2010

Electromagnetic Fields, Power Losses, and Resistance of High-Frequency Magnetic Devices

Daniel Joseph Whitman
Wright State University

Electromagnetic Fields, Power Losses, and Resistance of High-Frequency Magnetic Devices

A thesis submitted in partial fulfilment
of the requirements for the degree of
Master of Science in Engineering

By

DANIEL WHITMAN
B.S., Wright State University, 2007

2010
Wright State University

WRIGHT STATE UNIVERSITY
SCHOOL OF GRADUATE STUDIES

March 12, 2010

I HEREBY RECOMMEND THAT THE THESIS PREPARED UNDER MY SUPERVISION BY Daniel Joseph Whitman ENTITLED Electromagnetic Fields, Power Losses, and Resistance of High-Frequency Magnetic Devices BE ACCEPTED IN PARTIAL FULFILLMENT OF THE REQUIREMENTS FOR THE DEGREE OF Master of Science in Engineering.

Marian K. Kazimierczuk, Ph. D.
Thesis Director

Kefu Xue, Ph. D.
Department Chair

Committee on
Final Examination

Marian K. Kazimierczuk, Ph. D.

Ronald Riechers, Ph. D.

Raymond Siferd, Ph. D.

Jonh A. Bantle, Ph.D.
Vice President for Research and
Graduate Studies and Interim Dean
of Graduate Studies

ABSTRACT

Whitman, Daniel. M.S.Egr. Department of Electrical Engineering, Wright State University, 2010. Electromagnetic Fields, Power Losses, and Resistance of High-Frequency Magnetic Devices.

The operation of dc-dc PWM converters requires magnetic components that operate at high frequencies and carry large currents. At such frequencies the skin and proximity effects cause a substantial increase in power losses and ac resistance. This thesis reviews existing one dimensional analytical work on the prediction of these losses and, beginning with an inductor, derives expressions for the electromagnetic fields and power losses within the winding as well as the ac resistance of the device. The results of the inductor analysis are then extended to examine these quantities in transformers of various winding configurations. It is shown that proximity effects are theoretically eliminated and losses significantly reduced if the windings are interleaved in transformers with many layers. Following this, the more general case of a device with a core of arbitrary permeability is examined. It is found that 1-D analysis is insufficient to treat the analogous transformer case. It is shown that the losses in both devices can be significantly mitigated by optimizing the layer thicknesses and that the power savings is significant. A theoretical inconsistency in Dowell's approach is identified as well as its effects on the analysis done herein.

Contents

List of Figures

List of Tables

1

Introduction

1.1 Overview

Power losses in magnetic components can be completely divided into losses within the core, losses within the winding, and radiation losses. Core losses comprise ohmic losses due to a core with a nonzero conductivity and hysteresis losses in the magnetic material. Winding losses are entirely ohmic due to the winding material also having a finite conductivity (i.e. not an ideal conductor). At high frequencies these losses in the winding are exacerbated by the skin and proximity effects. The former is solely a property of the winding material [Robert 2002] while the latter is caused by the geometry of the device and includes effects from both the winding as well as the core [Spang and Albach 2008]. It will be shown herein that the radiation losses are negligible relative to the other causes of loss so long as the frequency is not too high, which is the case for most present applications. The purpose of this work is to determine analytically the electromagnetic fields in the winding space of a high-frequency magnetic component and the losses due to the windings, a topic that has received considerable attention in the literature.

1.2 Literature Review

1.2.1 Dowell and Venkatraman

The seminal work on the losses due to the windings of a high-frequency magnetic device is [Dowell 1966] by Dowell. He considered the windings as infinitely long, straight conductors and, after making certain assumptions, reduced the problem to one dimension. The primary assumption that allows this is the neglect of edge effects, which is justified in this work in Section 2.2. The system setup by Dowell also accounts for windings that are not a solid conductor (i.e. a foil), though still with a

rectangular cross section. His treatment of this is, however, an area of important theoretical debate [Robert 2002]. Dowell's approach is to use Maxwell's equations and boundary conditions to first determine an expression for the current density within an arbitrary layer. From the current density, the flux cutting each layer is found and, from this, the voltage across a given layer is found. Once the voltage is determined, Dowell's equation is simply the real part of the impedance determined from the voltage and current.

In [Venkatraman 1984], Venkatraman uses Dowell's results to extend analysis from purely sinusoidal current waveforms for rectangular and trapezoidal waves. This is accomplished by decomposing such waveforms into their Fourier components and then summing the losses or resistance using Dowell's equation for each harmonic. It was found in this work that the losses and resistance are substantially increased in the rectangular case as compared to the sinusoidal case. It was also shown that, for trapezoidal waveforms, the losses and resistance is reduced as compared to purely rectangular waveforms and the losses decrease with longer rise and/or fall times. All of the theoretical conclusions presented in this article are verified by experiment.

1.2.2 Bennet, Larson, and Perry

In [Bennet and Larson 1940], Bennet and Larson solves the problem in both Cartesian and cylindrical coordinates, the latter of which takes into account the curvature of the winding. Their work, published in 1940, appears to be one of the first on the topic. Perry takes a similar approach with the same results in [Perry 1979], which has ostensibly been done independently. When the current density is solved for infinitely long straight conductors (i.e. in Cartesian coordinates), the results are consistent with Dowell's. Unlike Bennet and Larson, Perry is primarily concerned with the power dissipation rather than the frequency-dependent resistance, though the normalized total power loss is equal to the normalized ac resistance. After determining the power dissipation and resistance within a layer, it is minimized and the authors arrive at expressions for the optimum thickness of each layer, though they mention the impracticality of this in production. Because of this, Perry continues on to derive an expression for the optimum thickness of the layers where all the layers are of the same thickness.

In cylindrical coordinates, the authors arrive at a solution for the current density that involves Bessel functions. While theoretically more accurate, the presence of Bessel functions make further analysis (e.g. determining expressions for power and/or impedance) difficult. To remedy this, the Bessel functions are approximated by exponentials, an approximation that is valid so long as radius of curvature is considerably greater than the skin depth and the width of the layers. Though his article was published later, Perry arrived at his results ostensibly independently of Dowell's as

[Dowell 1966] was not cited in his paper. Unlike Dowell's, these authors' treatments do not fully account for a non-foil winding. Though not in the same form, Bennet/Larson/Perry's final equation for total power loss and resistance is equivalent to Dowell's, which is shown here in Appendix C.

1.2.3 Vandelac and Ziogas

Vandelac and Ziogas, in [Vandelac and Ziogas 1988], expand on Perry's work by solving for a more general case in Cartesian coordinates. In particular they recognized that the fields and current density within the layers and therefore the total losses depend only on the tangential magnetic field at the surfaces of the conductors. Their resulting equations thus allow for an arbitrary MMF pattern in which the fields at the inner and outer surfaces of a layer may be of different magnitude and phase. The equations also account for immersion of the device in an external magnetic field, which has nontrivial effects on the resulting power dissipation. Also built into their treatment is the decomposition of an arbitrary periodic current into its Fourier components, though this could be readily found by summing the losses found using Dowell's or Perry's equations for each harmonic. Their equations for power losses degenerate to Perry's results when the appropriate assumptions are made and are thus also equivalent to Dowell's.

Their treatment is different from Dowell's however in that non-foil windings are handled differently. In their paper, Vandelac and Ziogas account for this by approximating a non-foil winding with a foil winding of equivalent cross-sectional area and an adjusted conductivity which contains a geometry-dependent porosity factor that is identical to that which appears in Dowell's work. The difference is that, in this work, this porosity factor is lumped in with the conductivity, and, in Dowell's, non-foil windings are treated directly. This is largely a matter of interpretation however and the results are equal so long as the same geometry used for Dowell's equation is not modified as might be done to keep the same cross-sectional area.

1.2.4 Hurley, Gath, and Breslin

The subject of [Hurley et al. 2000] is determining optimum layer thickness for arbitrary periodic currents using only the RMS values without having to determine the Fourier coefficients. Though interesting, the relevant part of this publication for this work is the appendix in which the authors derive Dowell's equation using a slightly different approach. In it, the magnetic field intensity is found in cylindrical coordinates and from this the electric field is determined. The authors then use the Poynting theorem to determine an expression for the complex power within a layer. It is at this point that, just as in [Perry 1979], the Bessel functions are approximated with complex exponentials. The powers within each layer are then summed to yield the total complex power in the winding.

The authors note that the normalized power loss is equivalent to the normalized resistance, though, with time averaging, the normalized resistance is actually equal to twice the normalized power loss. Thus, when the real part of the normalized power loss is taken, the result is identical to Dowell's with the exception that, like Perry's, this treatment does take into full account the effects of non-foil windings.

1.2.5 Ferreira and Robert

In [Ferreira 1994], Ferreira improves upon existing one-dimensional analysis by recognizing the orthogonality of the skin and proximity effects when certain assumptions are made. This fact means that the two effects can be determined independently and the simply summed together to get the solution. Applying this, he determines an exact solution for round conductors and shows the error introduced when, as in previous work, round conductors are approximated by square conductors of equal cross-sectional area. Ferreira also identifies a flaw with previous work in which the geometry-dependent porosity factor affects the skin depth, which is only a property of the material and not geometry. This theoretical inconsistency is presented in more detail in [Robert 2002] and is discussed later here in Section 5.1.

1.2.6 Bartoli, Noferi, Reatti, and Kazimierczuk

The authors derive in the appendix of [Bartoli et al. 1995] an expression for the ac resistance of an inductor winding with a round cross-section and, in the body of the article, propose an equivalent circuit model. Their equation is different from that given by Ferreira in [Ferreira 1994], though they only differ in the proximity effect term of the equation. These differences are compared in [Reatti and Kazimierczuk 2002] by Reatti and Kazimierczuk along with the expressions derived by Perry. Their conclusion, which was verified by experiment, is that the Perry/Ferreira equations are accurate only in certain frequency ranges. Their experiments show that their expression, however, is valid from dc to the first inductor resonant frequency and is valid independent of the winding composition.

1.2.7 Other Work

There has also been work by various authors towards increasing the accuracy of power loss prediction by deviating from the simple one dimensional analysis to include 2-D effects and other geometry-dependent effects. In [Kutkut 1998b], Kutkut derives a simplified 2-D model and arrives at a correction factor that is multiplied by the 1-D equations to take into account edge effects, which he

says are more significant as the frequency is increased. The same author, in [Kutkut 1998a], explores the effects of air gap fringing fields on winding losses using the method of images, which extends the analysis to the more general case of non-ideal cores. In [Albach et al. 2007; Spang and Albach 2008], Albach and Spang perform 2-D analysis using the magnetic vector potential in conjunction with the orthogonal expansion technique to compute the effects of a rod core by computer. Also utilizing the magnetic vector potential in two dimensions, Podoltsev uses repeat elementary cell concept, in [Podoltsev et al. 2003], to also determine the losses in the winding numerically.

1.3 Objectives

The primary objective of this work is to examine the behavior of the electromagnetic fields within the winding space of magnetic devices at high-frequencies, the power losses that occur due the behavior of the fields, and the ac resistance of the device. To this end Chapter 2 begins by developing from fundamental physical equations the 1D model of the system that is used in the previous literature. Expressions for the electromagnetic fields and current density are then derived beginning with the Maxwell's equations to which the fields must subscribe. The behavior of the fields is analyzed, which has not been done in the literature. From the fields the power density is determined followed by the total losses, which are determined in two different ways. From the total power losses the impedance is readily found, the real part of which is the ac resistance. The approach used here is a combination of the approaches used in the literature and is, at least in the author's opinion, more straightforward than Dowell's approach.

The results of the inductor analysis will then be extended to transformers in Chapter 3, which has not been treated explicitly in the literature. General deductions are made which apply to transformers in general regardless of winding configuration. Transformers with various winding configurations are discussed and expressions for power losses and ac resistance are derived first for general transformers in which the primary and secondary windings may not have the same material and geometric properties, and then for the special case in which the windings are the same. Transformers with non-interleaved windings are compared with those with interleaved windings and the effects of interleaving on the power losses are determined. In both the inductor and transformer cases non-sinusoidal current waveforms are not treated but can be readily treated using Fourier decomposition as has been done previously in the literature.

In Chapter 4 the analysis in the previous chapters is repeated for the more general case of devices with a non-ideal core ($\mu_r \ll \infty$), though it is found that the transformer case is beyond the scope of this work. We then shall show how the power losses can be significantly reduced by optimizing the

layer thicknesses of inductors and transformers. Two cases are treated, one in which each layer has a different optimum thickness and the other in which, for practical purposes, all the layers are the same thickness. In the final chapter, the conclusions of our analysis are enumerated, including the exposition of an incongruence in Dowell's analysis. The numerous appendices then serve to elucidate some of the concepts in the analysis as well as show some of the more tedious derivations needed in the body.

2

Electromagnetic Fields and Power Losses in a Multilayer Inductor

2.1 Maxwell's Equations

Consider the windings of a multilayer inductor carrying an alternating current $i(t) = I\cos\omega t$ and thus having a phasor representation of $\tilde{I} = I$. Neglecting the curvature of the cylindrical device, we shall consider the windings as straight, parallel conductors with rectangular cross sections as depicted in Fig. 2.1. The coordinate system is affixed as shown with the origin placed at the center of the core.

The conductors are regarded as having an equal amount of positive and negative charge, resulting in a net charge density of zero. Maxwell's equations therefore take the phasor form

$$\begin{aligned}
\nabla \cdot \tilde{\mathbf{E}} &= \frac{\rho}{\epsilon_0} = 0 \\
\nabla \times \tilde{\mathbf{E}} &= -\mu_0 j\omega \tilde{\mathbf{H}} \\
\nabla \cdot \tilde{\mathbf{H}} &= 0 \\
\nabla \times \tilde{\mathbf{H}} &= \tilde{\mathbf{J}} + \epsilon_0 j\omega \tilde{\mathbf{E}}\,,
\end{aligned}$$

where $\rho = 0$ is the charge density and the tilde above a symbol indicates that it is a complex phasor quantity or function. We are presently concerned with the fields and current density in the conductors. This being the case, Ohm's law ($\tilde{\mathbf{E}} = \rho_w \tilde{\mathbf{J}}$) can be applied. Doing so, we rewrite

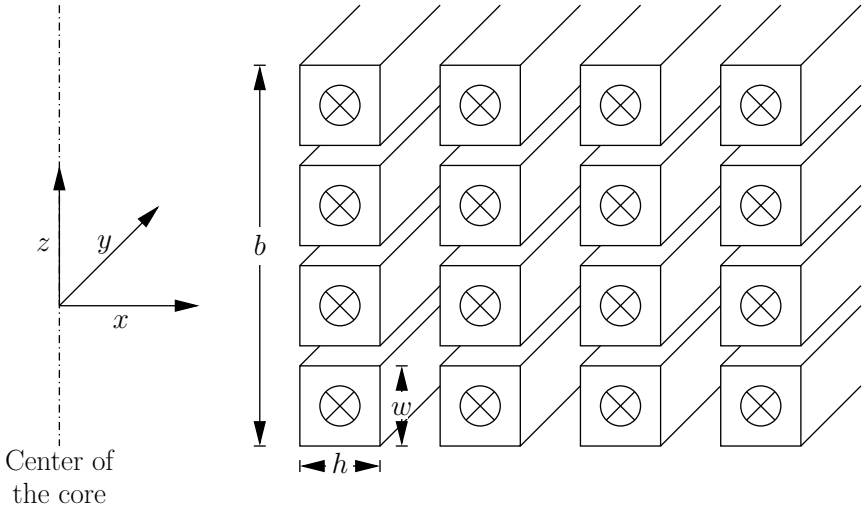

Figure 2.1: The windings of a magnetic device considered as straight, parallel conductors.

Maxwell's equations as

$$\nabla \cdot \tilde{\mathbf{J}} = \frac{\rho}{\epsilon_0 \rho_w} = 0 \tag{2.1}$$

$$\nabla \times \tilde{\mathbf{J}} = -\frac{j\omega\mu_0}{\rho_w}\tilde{\mathbf{H}} \tag{2.2}$$

$$\nabla \cdot \tilde{\mathbf{H}} = 0 \tag{2.3}$$

$$\nabla \times \tilde{\mathbf{H}} = (1 + j\omega\epsilon_0\rho_w)\tilde{\mathbf{J}}\,, \tag{2.4}$$

where ρ_w is the resistivity of the conductors.

Consider the complex coefficient of (2.4) in which the real and imaginary parts represent the magnetic field due to the current and the changing electric field, respectively. Let us propose that the imaginary part is negligible with respect to the real part. This is the case if and only if the imaginary part is no more than two orders of magnitude less than unity:

$$100\epsilon_0\rho_w\omega \leq 1\,.$$

Solving for the frequency, we get

$$\omega \leq \frac{1}{100\epsilon_0\rho_w}\,.$$

For copper windings, $\rho_w = 17.24$ nΩm at 20 °C, so the highest frequency at which the imaginary term can be considered negligible in that case is 65,542 THz. Since the frequencies encountered in common practice are nowhere near this, we are justified in neglecting this term. In doing so we have a magnetoquasistatic model of the system and (2.4) becomes simply

$$\nabla \times \tilde{\mathbf{H}} = \tilde{\mathbf{J}}\,. \tag{2.5}$$

2.2 General Field Solution

We assume that $h \ll b$ and so the end effects are taken to be negligible. This neglect of end effects is further justified if the windings are surrounded by a high-permeability material, which causes the magnetic field intensity to be nearly zero at the tops and bottoms of the winding. We also neglect the effects of the gaps in between the turns of a given layer. Because of these and symmetry,

$$\tilde{H}_x = \tilde{H}_y = 0\,,$$

where the subscripts denote the components of the vectors. It is also clear that

$$\tilde{J}_x = \tilde{J}_z = 0$$
$$\therefore\ \tilde{E}_x = \tilde{E}_z = 0\,.$$

Because the magnetic field and current density contain only z and y components, respectively, the subscripts can be dropped without ambiguity. Also, from (2.3) and (2.1), it follows that the fields and current density are independent of y and z and so are functions of x only. Thus

$$\tilde{J} = \tilde{J}_y = \tilde{J}(x) = \tilde{J}_y(x)$$
$$\tilde{E} = \tilde{E}_y = \tilde{E}(x) = \tilde{E}_y(x)$$
$$\tilde{H} = \tilde{H}_z = \tilde{H}(x) = \tilde{H}_z(x)\,.$$

Applying these deductions to (2.2), it becomes

$$\frac{d\tilde{J}}{dx} = -\frac{j\omega\mu_0}{\rho_w}\tilde{H}\,. \tag{2.6}$$

In order to take into account the fact that the turns in a given layer are separate conductors, we must use the integral form of (2.5). The core of the magnetic device is assumed to be ideal, which means that $\mu_r \to \infty$ and $\sigma_c \to 0$. As a result of this, the magnetic field intensity inside the core goes to zero. Consider then the Amperian loop shown L in Fig. 2.2, which extends from the core to partially through the nth layer from the center. Integrating clockwise along this loop, we obtain the relation

$$-b\tilde{H}(x) = N_t I(n-1) + N_t \int_{x_{n_i}}^{x} w\tilde{J}(x)dx\,. \tag{2.7}$$

where N_t is the number of turns per layer and w and b are the lengths shown in Fig. 2.1. x_{n_i} is the distance from the center of the core (the origin) to the inner surface of the nth layer. Solving (2.7) for $\tilde{H}(x)$ and differentiating both sides with respect to x, we get

$$\frac{d\tilde{H}}{dx} = -\eta\tilde{J}\,, \tag{2.8}$$

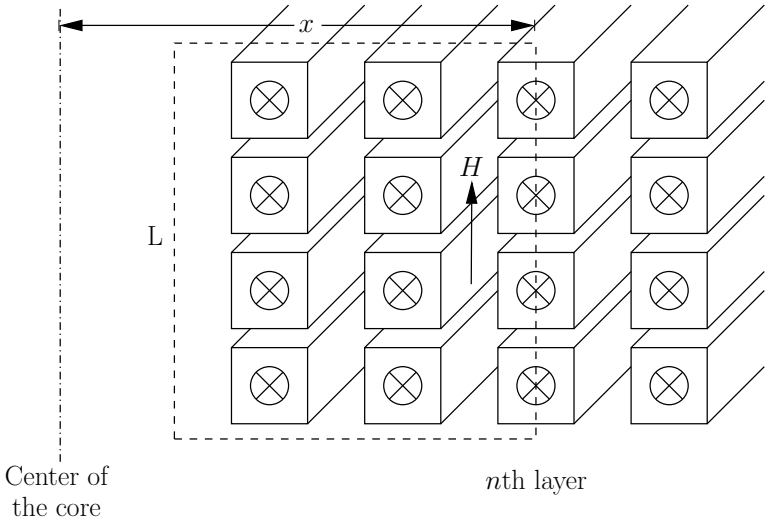

Figure 2.2: Amperian loop extending partially through the nth layer.

where

$$\eta \equiv \frac{N_t w}{b}$$

is the porosity factor. Differentiating (2.8) with respect to x and then substituting (2.6) into it yields

$$\frac{d^2\tilde{H}}{dx^2} = \frac{j\omega\mu_0\eta}{\rho_w}\tilde{H}\,.$$

This is an ordinary, second-order differential equation and, more specifically, it is the one-dimensional Helmholtz equation. The general solution is

$$\tilde{H}(x) = H_a e^{\gamma x} + H_b e^{-\gamma x}\,, \tag{2.9}$$

where H_a and H_b are complex constants,

$$\gamma \equiv \sqrt{\frac{j\omega\mu_0\eta}{\rho_w}} = \frac{1+j}{\delta_w}\sqrt{\eta}\,,$$

and the skin depth is

$$\delta_w \equiv \sqrt{\frac{2\rho_w}{\omega\mu_0}}\,.$$

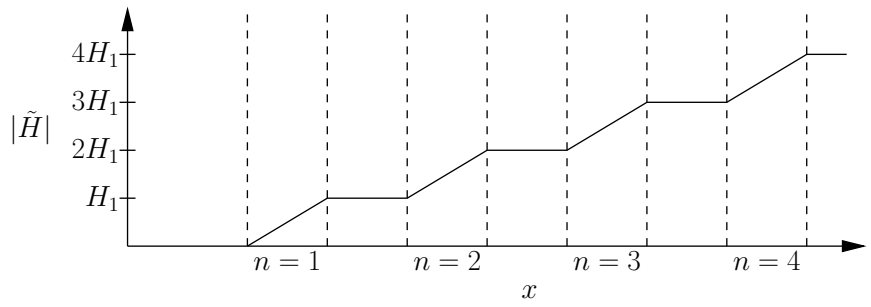

Figure 2.3: The magnitude of the magnetic field across the layers at low frequencies ($\delta_w \gg h$).

2.3 Boundary Conditions

In order to obtain specific solutions to the fields, the boundary conditions of the differential equation must be established. From the neglect of end effects it follows that the magnetic field intensities in between the layers are of constant amplitude and phase with respect to x, and so the magnetic field intensities across the layers will, in general, be something like what is shown in Fig. 2.3. In this figure, the magnetic field intensities inside the winding space is shown as it would be at low frequencies ($\delta_w \gg h$). At high frequencies the skin and proximity effects are prevalent as will be shown.

In the literature there are conflicting reports regarding the boundary conditions. In [Dowell 1966] and [Hurley et al. 2000] the core is assumed to be ideal, as we have done here, and the magnetic field intensity at the inner surface of the innermost layer is thus zero. However, in [Perry 1979] and [Vandelac and Ziogas 1988] the magnetic field is assumed to be zero at the outer surface of the outermost layer, which can be deduced from the fact that it must be zero infinitely far from the device and the neglect of edge effects. In the former case the magnetic field intensity throughout the winding space is as shown in Fig. 2.3 while in the latter case the magnetic field intensity takes on the opposite configuration with zero intensity on the outside and maximum intensity at the core. Both of these are reasonable and it can be shown that this difference is inconsequential when determining the total power losses. However, as we are here also concerned with the nature of the fields themselves, this discrepancy must be resolved.

To resolve this, 2-D finite element analysis was performed using Maxwell, which is an electromagnetic finite element analysis program developed by the Ansoft Corporation. The simulated model had the following geometric parameters: $\eta = 1$, $h/\delta_w = 3$, and $b/h = 100$ with four layers. A plot of the resulting magnetic field intensity is shown in Fig. 2.4 and, in this plot, the plateaus are in between the layers and the dips are within the layers. It is clear that, when a high-permeability core

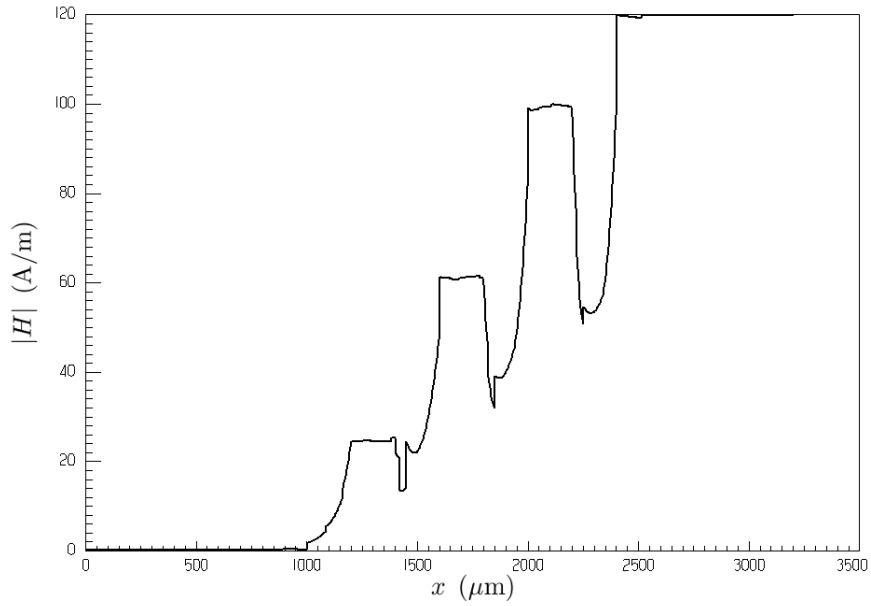

Figure 2.4: Simulated magnetic field intensity across multiple winding layers.

is used, it can be assumed to be ideal and the magnetic field intensity configuration is as we have deduced here.

Consider now the Amperian loops L1 and L2 shown in Fig. 2.5, where we are concerned with the nth layer from the inside. Summing around L1 and L2, we have

$$-b\tilde{H}(x_{n_i}) = (n-1)IN_t$$
$$-b\tilde{H}(x_{n_o}) = nIN_t\,,$$

respectively, where x_{n_o} is the distance from the center of the core to the outer surface of the conductor as shown in Fig. 2.6. Solving for the magnetic field intensities at the surfaces, we obtain

$$\tilde{H}(x_{n_i}) = -(n-1)H_1 \tag{2.10}$$
$$\tilde{H}(x_{n_o}) = -nH_1\,, \tag{2.11}$$

where the magnetic field intensity phasor between the first and second layers is

$$H_1 \equiv \frac{N_t I}{b}\,.$$

Evidently the magnetic field intensity phasor in between the conductors is real and so the physical field here oscillates with zero phase shift relative to the current. Note that (2.10) and (2.11) are negative and so the field really points downward in the negative z direction in between the layers. However, we shall consider it to be the positive z direction (and keep the negative signs) so as to be

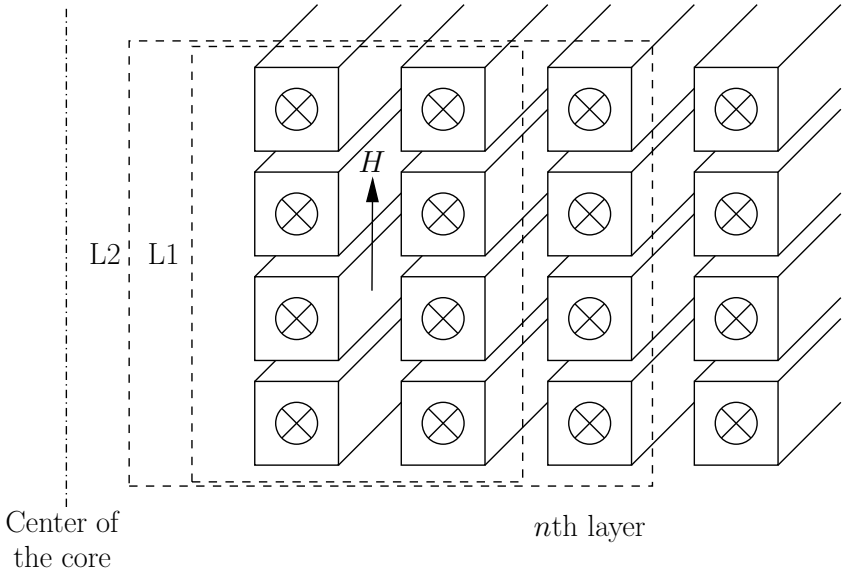

Figure 2.5: Amperian loops used to determine the boundary conditions of the nth layer.

consistent with our coordinate system. An alternate interpretation, and perhaps a more appropriate one given our time harmonic analysis, is that the magnetic field intensities in between the layers point in the positive z direction and are simply 180° out of phase with the current.

2.4 Specific Field Solutions

Now that we are in possession of the governing differential equation and the boundary conditions, we are in a position to determine the magnetic field inside of the nth layer. Though we have in the previous section found the boundary conditions for the nth layer, let us first consider some general boundary conditions

$$H_{ni} \equiv \tilde{H}(x_{n_i})$$
$$H_{no} \equiv \tilde{H}(x_{n_o})\,,$$

where H_{ni} and H_{no} may be complex. Substituting the latter of these into 2.9, we have

$$\tilde{H}(x_{n_o}) = H_a e^{\gamma x_{n_o}} + H_b e^{-\gamma x_{n_o}} = H_{no}\,,$$

and then solving for H_b in terms of H_a:

$$H_b = \frac{H_{no} - H_a e^{\gamma x_{n_o}}}{e^{-\gamma x_{n_o}}}\,. \tag{2.12}$$

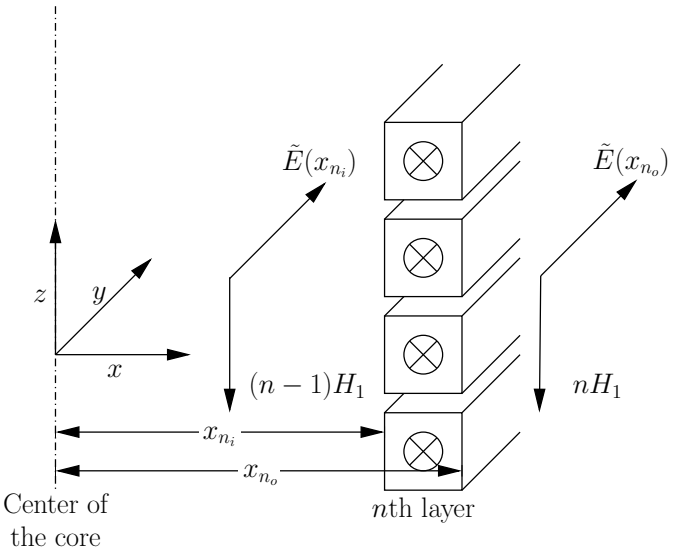

Figure 2.6: Boundary conditions of the nth layer.

Next we apply the other boundary condition to (2.9) and substitute (2.12) for H_b:

$$\begin{aligned}
\tilde{H}(x_{n_i}) = H_a e^{\gamma x_{n_i}} + \frac{H_{no} e^{-\gamma x_{n_i}} - H_a e^{\gamma(x_{n_o} - x_{n_i})}}{e^{-\gamma x_{n_o}}} &= H_{ni} \\
H_a e^{\gamma(x_{n_i} - x_{n_o})} + H_{no} e^{-\gamma x_{n_i}} - H_a e^{\gamma(x_{n_o} - x_{n_i})} &= H_{ni} e^{-\gamma x_{n_o}} \\
H_a &= \frac{H_{ni} e^{-\gamma x_{n_o}} - H_{no} e^{-\gamma x_{n_i}}}{e^{-\gamma h} - e^{\gamma h}} \\
H_a &= \frac{H_{no} e^{-\gamma x_{n_i}} - H_{ni} e^{-\gamma x_{n_o}}}{2 \sinh \gamma h} ,
\end{aligned} \tag{2.13}$$

where $h = x_{n_o} - x_{n_i}$ is the height of the layers and it is assumed that all layers are of the same height. H_b is found by substituting (2.13) back into (2.12):

$$\begin{aligned}
H_b = \frac{H_{no} - H_a e^{\gamma x_{n_o}}}{e^{-\gamma x_{n_o}}} &= H_{no} e^{\gamma x_{n_o}} - H_a e^{2\gamma x_{n_o}} \\
H_b = H_{no} e^{\gamma x_{n_o}} + \frac{H_{ni} e^{\gamma x_{n_o}} - H_{no} e^{\gamma(2x_{n_o} - x_{n_i})}}{2 \sinh \gamma h} & \\
H_b = \frac{H_{no} e^{\gamma x_{n_o}} [e^{\gamma(x_{n_o} - x_{n_i})} - e^{\gamma(x_{n_i} - x_{n_o})}] + H_{ni} e^{\gamma x_{n_o}} - H_{no} e^{\gamma(2x_{n_o} - x_{n_i})}}{2 \sinh \gamma h} & \\
H_b = \frac{H_{ni} e^{\gamma x_{n_o}} - H_{no} e^{\gamma x_{n_i}}}{2 \sinh \gamma h} . &
\end{aligned} \tag{2.14}$$

After plugging (2.13) and (2.14) into (2.9), we obtain the solution in terms of general boundary

conditions:

$$\begin{aligned}\tilde{H}(x) &= H_a e^{\gamma x} + H_b e^{-\gamma x} \\ \tilde{H}(x) &= \frac{H_{no} e^{\gamma(x-x_{n_i})} - H_{ni} e^{\gamma(x-x_{n_o})} + H_{ni} e^{\gamma(x_{n_o}-x)} - H_{no} e^{\gamma(x_{n_i}-x)}}{2\sinh\gamma h} \\ \tilde{H}(x) &= \frac{H_{ni}\sinh\left[\gamma(x_{n_o}-x)\right] + H_{no}\sinh\left[\gamma(x-x_{n_i})\right]}{\sinh\gamma h}\,. \end{aligned} \tag{2.15}$$

Plugging in the boundary conditions for our problem found in the previous section, i.e. (2.10) and (2.11), gives the specific solution for the magnetic field intensity inside the nth layer:

$$\tilde{H}(x) = -H_1 \frac{n\sinh\left[\gamma(x-x_{n_i})\right] + (n-1)\sinh\left[\gamma(x_{n_o}-x)\right]}{\sinh\gamma h}\,. \tag{2.16}$$

Substituting (2.16) into (2.8) and solving for $\tilde{J}$ yields the current density in the nth layer,

$$\tilde{J}(x) = -\frac{1}{\eta}\frac{d\tilde{H}}{dx} = \frac{H_1\gamma}{\eta}\left\{\frac{n\cosh\left[\gamma(x-x_{n_i})\right] - (n-1)\cosh\left[\gamma(x_{n_o}-x)\right]}{\sinh\gamma h}\right\}, \tag{2.17}$$

and the electric field in the nth layer

$$\tilde{E}(x) = \rho_w\tilde{J} = \frac{H_1\rho_w\gamma}{\eta}\left\{\frac{n\cosh\left[\gamma(x-x_{n_i})\right] - (n-1)\cosh\left[\gamma(x_{n_o}-x)\right]}{\sinh\gamma h}\right\}. \tag{2.18}$$

To gain some insight into what is going in the conductors, it will be useful to plot the derived equations. In order to avoid having to choose arbitrary values for the various parameters, we can normalize the equations in such a way that the parameters and the fields become unitless. We shall do this by normalizing the parameters to the height h of the nth conductor and the magnetic field intensity and current density to its boundary value and its low frequency value, respectively:

$$\boxed{\frac{\tilde{H}(\frac{x}{h})}{H_1} = \frac{(1-n)\sinh\kappa\beta - n\sinh\kappa\alpha}{\sinh\kappa\epsilon}} \tag{2.19}$$

and

$$\boxed{\frac{\tilde{J}(\frac{x}{h})}{J_{LF}} = \frac{\tilde{E}(\frac{x}{h})}{E_{LF}} = \kappa\epsilon\frac{n\cosh\kappa\alpha - (n-1)\cosh\kappa\beta}{\sinh\kappa\epsilon}\,,} \tag{2.20}$$

where, for compactness, we introduce the constants

$$\begin{aligned}\epsilon &\equiv \sqrt{\eta}\frac{h}{\delta_w} \\ \kappa &\equiv 1 + j\end{aligned}$$

and the normalized variables

$$\begin{aligned}\alpha &\equiv \epsilon\frac{x - x_{n_i}}{h} \\ \beta &\equiv \epsilon\frac{x_{n_o} - x}{h}\,.\end{aligned}$$

The uniform current density and uniform electric field that occur in the low-frequency case ($\delta_w \gg h$) and appear in (2.20) are

$$J_{LF} \equiv \frac{H_1}{\eta h} = \frac{I}{wh}$$
$$E_{LF} \equiv \rho_w J_{LF} = \frac{\rho_w I}{wh}\,.$$

Plots of the normalized functions are shown in Fig. 2.7 through Fig. 2.22 for several layers and for various h/δ_w. These plots are for a single, solid conductor, i.e. a foil ($\eta = 1$). Because the electric field is proportional to the current density and therefore the normalized electric field is equal to the normalized current density, only plots of the latter are shown. The normalized edges of each layer were chosen arbitrarily but with $x_{n_i} > 0$, for, though the equations will allow it, the inner surface of the innermost layer must allow room for a core. Also satisfied is the necessary condition that

$$\frac{x_{n_o}}{h} - \frac{x_{n_i}}{h} = 1$$
$$\therefore\ x_{n_o} - x_{n_i} = h\,.$$

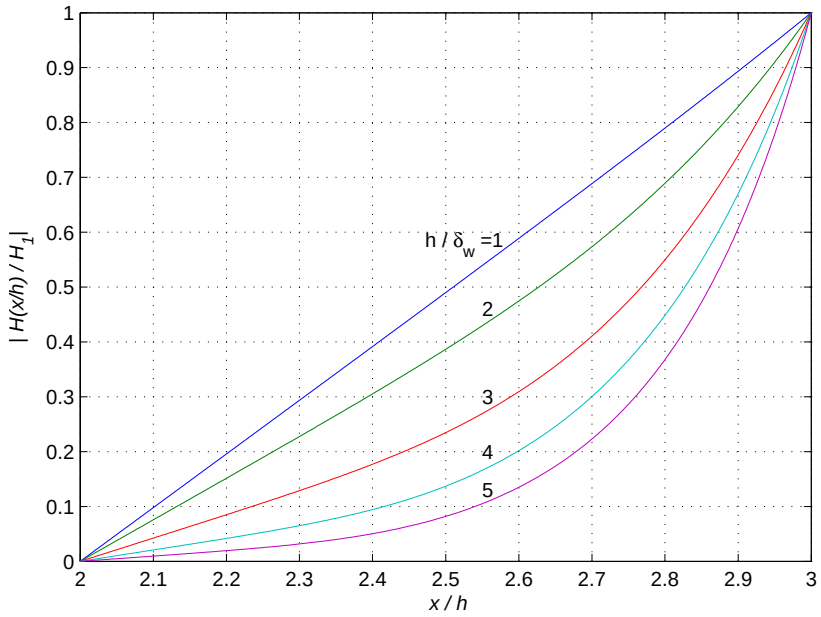

Figure 2.7: The magnitude of the normalized magnetic field intensity for $n = 1$.

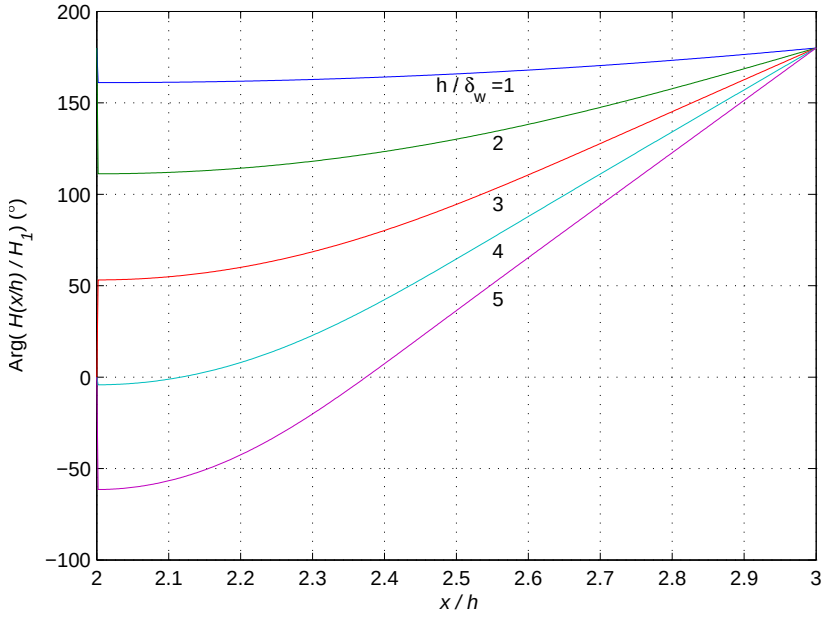

Figure 2.8: The phase of the normalized magnetic field intensity for $n = 1$.

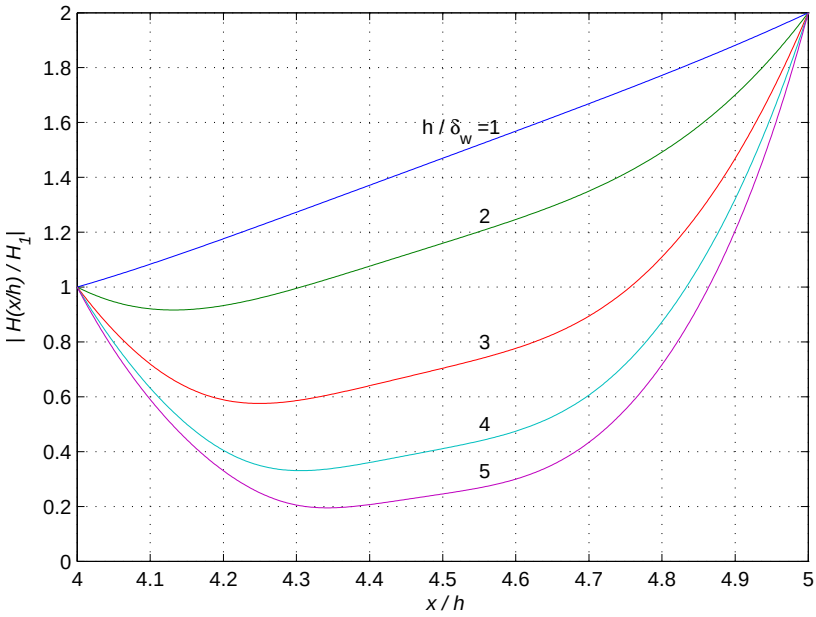

Figure 2.9: The magnitude of the normalized magnetic field intensity for $n = 2$.

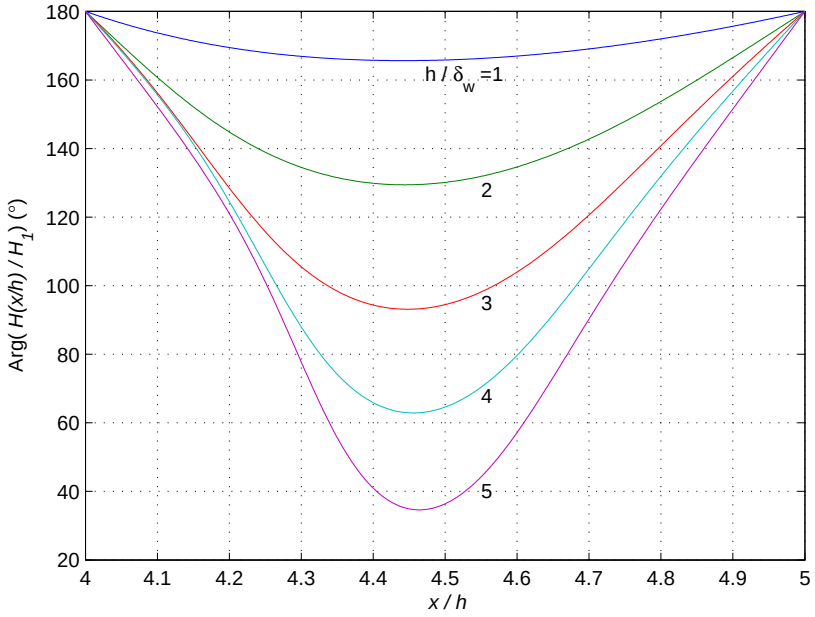

Figure 2.10: The phase of the normalized magnetic field intensity for $n = 2$.

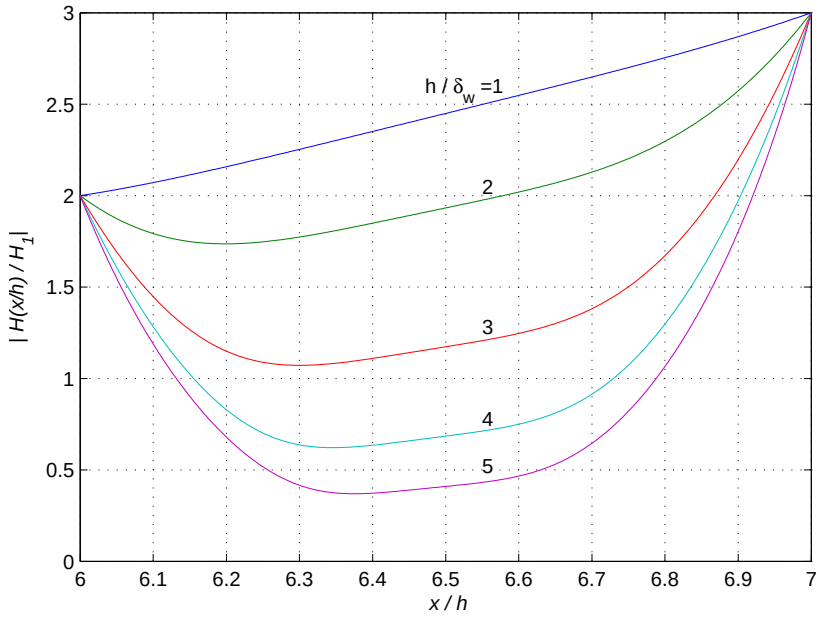

Figure 2.11: The magnitude of the normalized magnetic field intensity for $n = 3$.

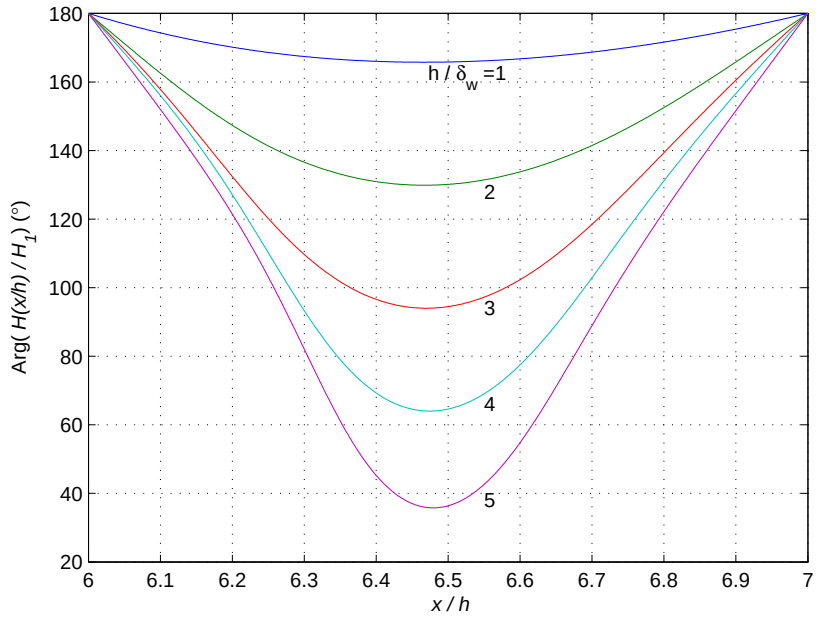

Figure 2.12: The phase of the normalized magnetic field intensity for $n = 3$.

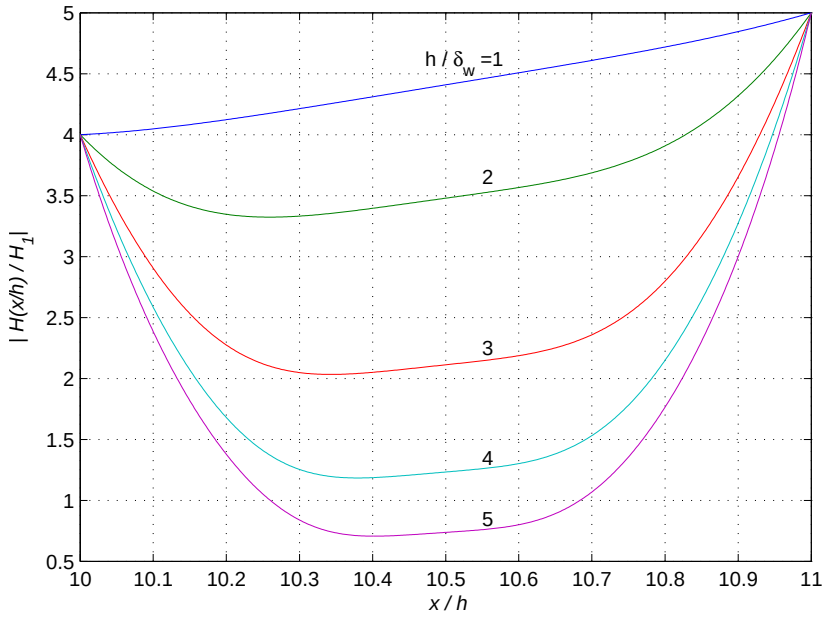

Figure 2.13: The magnitude of the normalized magnetic field intensity for $n = 5$.

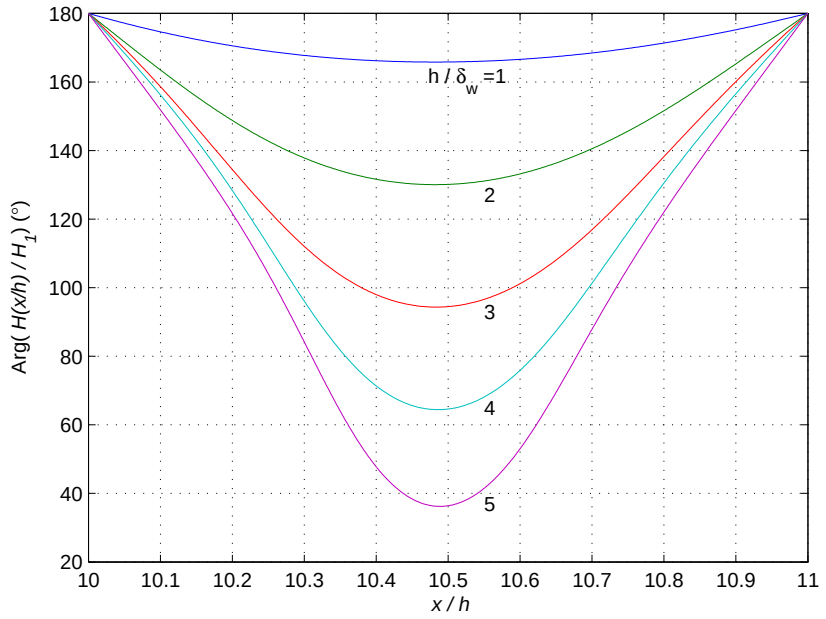

Figure 2.14: The phase of the normalized magnetic field intensity for $n = 5$.

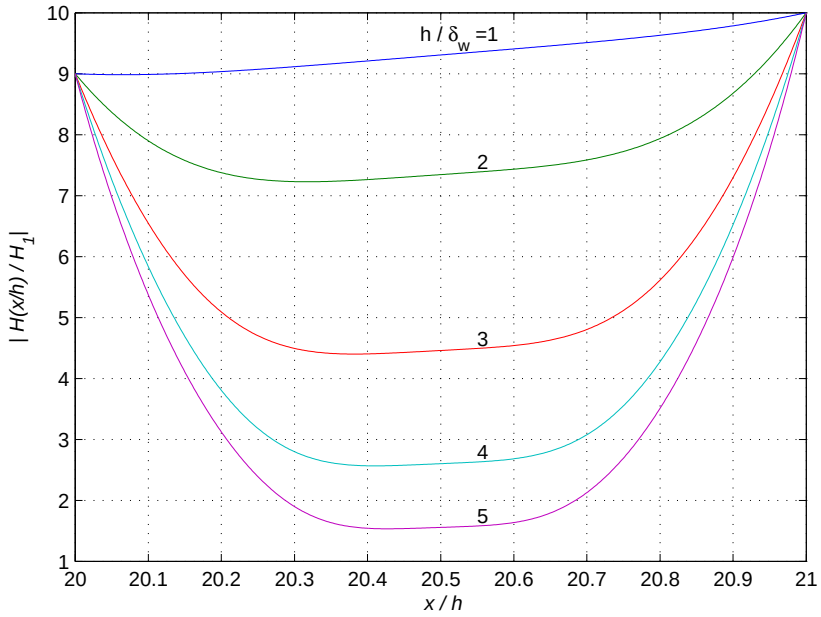

Figure 2.15: The magnitude of the normalized magnetic field intensity for $n = 10$.

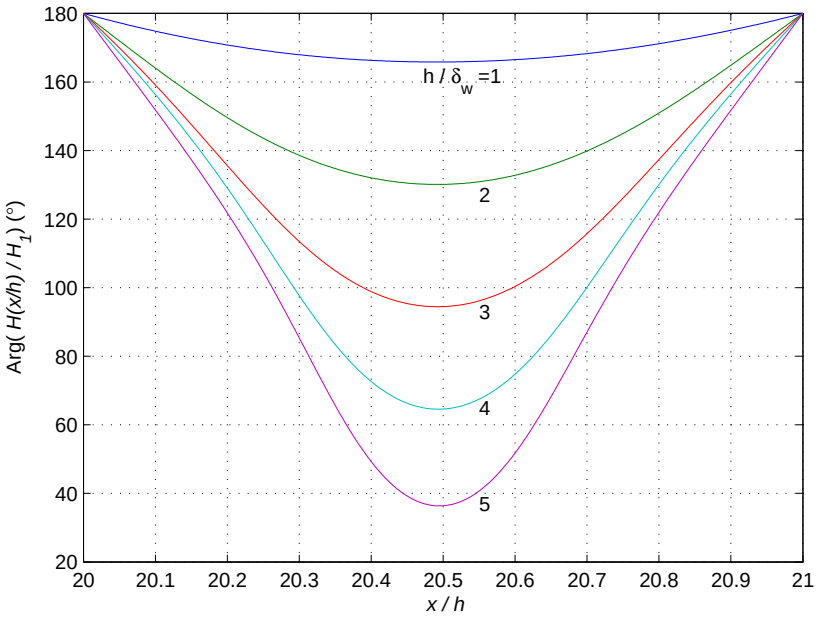

Figure 2.16: The phase of the normalized magnetic field intensity for $n = 10$.

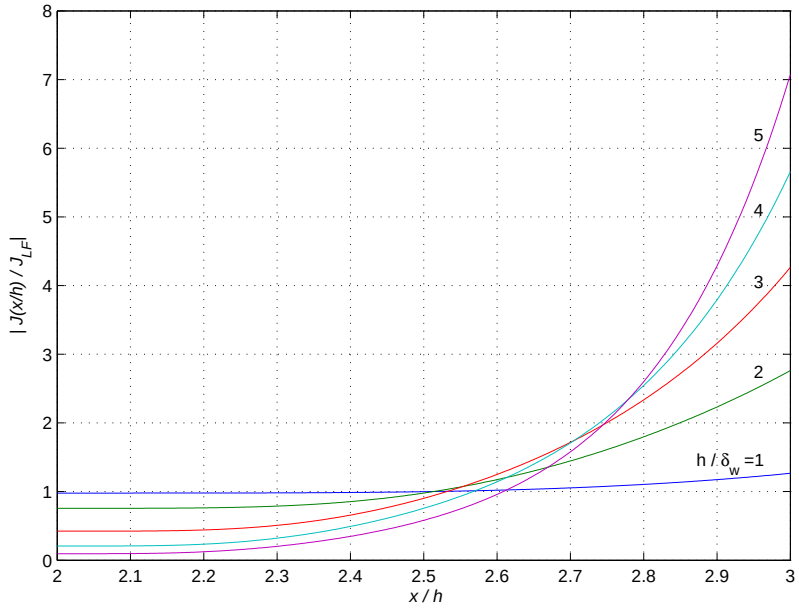

Figure 2.17: The magnitude of the normalized current density for $n = 1$.

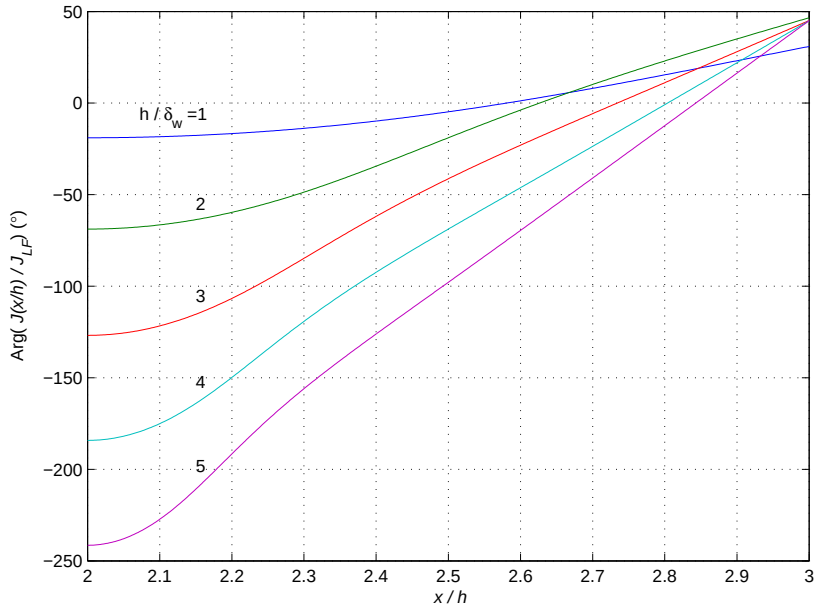

Figure 2.18: The phase of the normalized current density for $n = 1$.

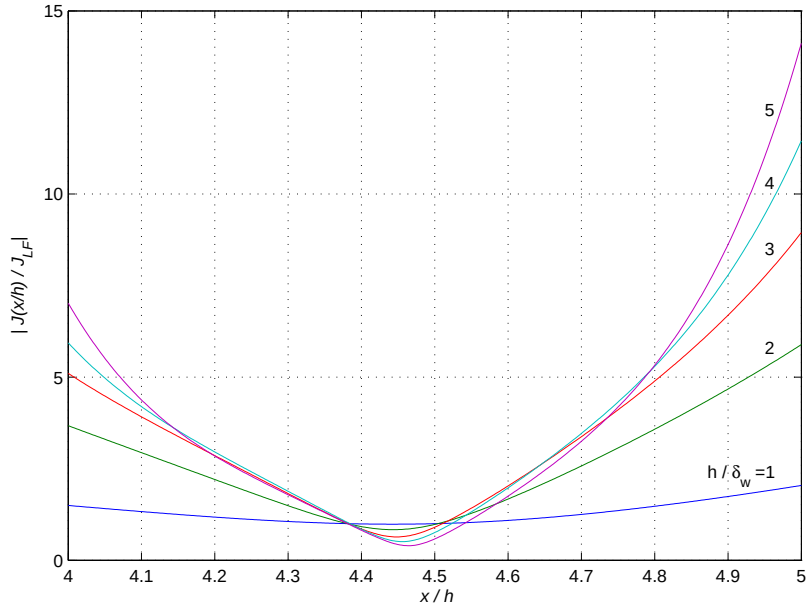

Figure 2.19: The magnitude of the normalized current density for $n = 2$.

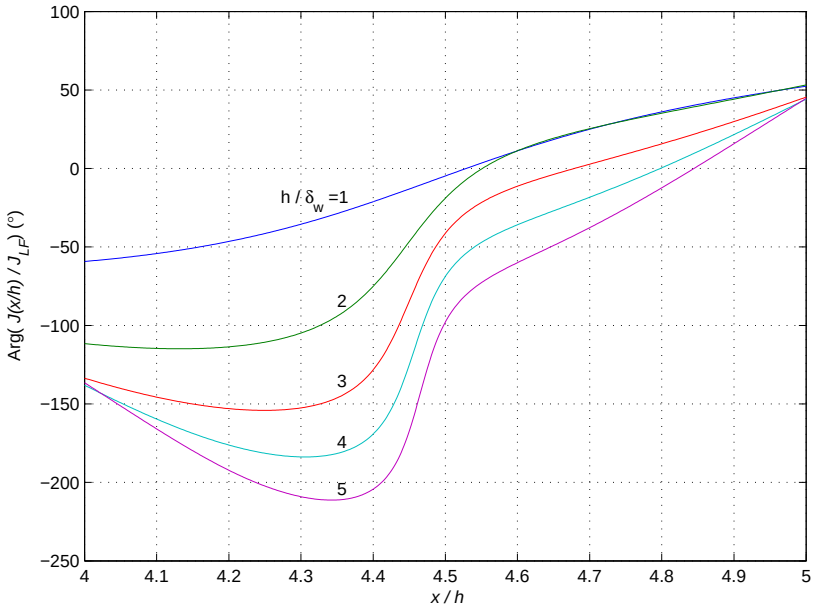

Figure 2.20: The phase of the normalized current density for $n = 2$.

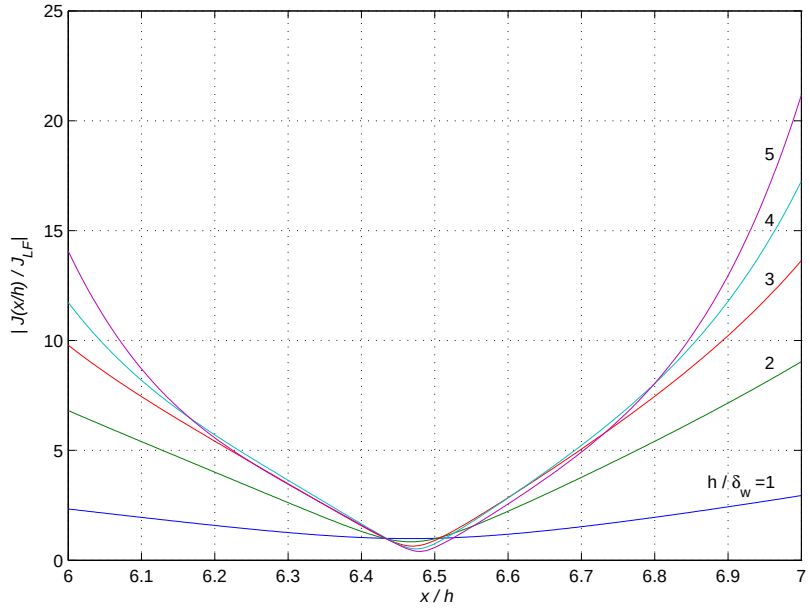

Figure 2.21: The magnitude of the normalized current density for $n = 3$.

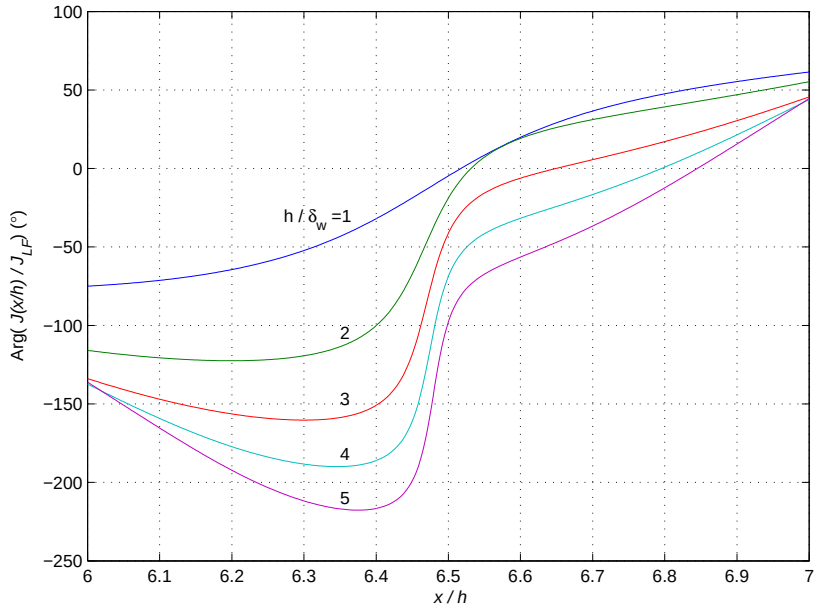

Figure 2.22: The phase of the normalized current density for $n = 3$.

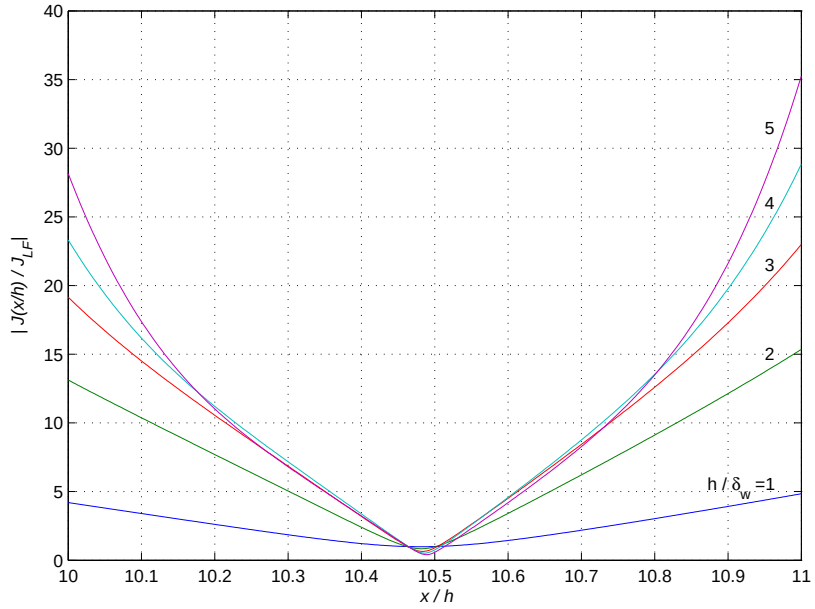

Figure 2.23: The magnitude of the normalized current density for $n = 5$.

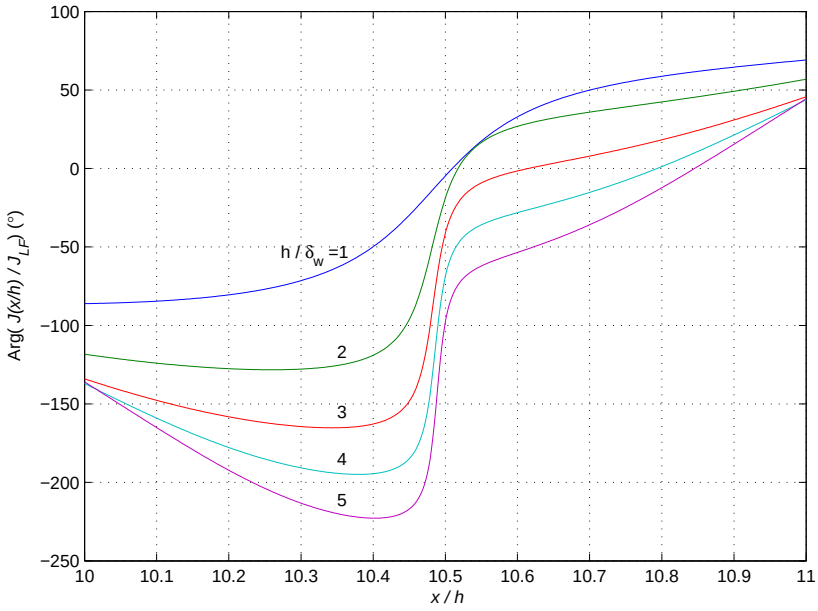

Figure 2.24: The phase of the normalized current density for $n = 5$.

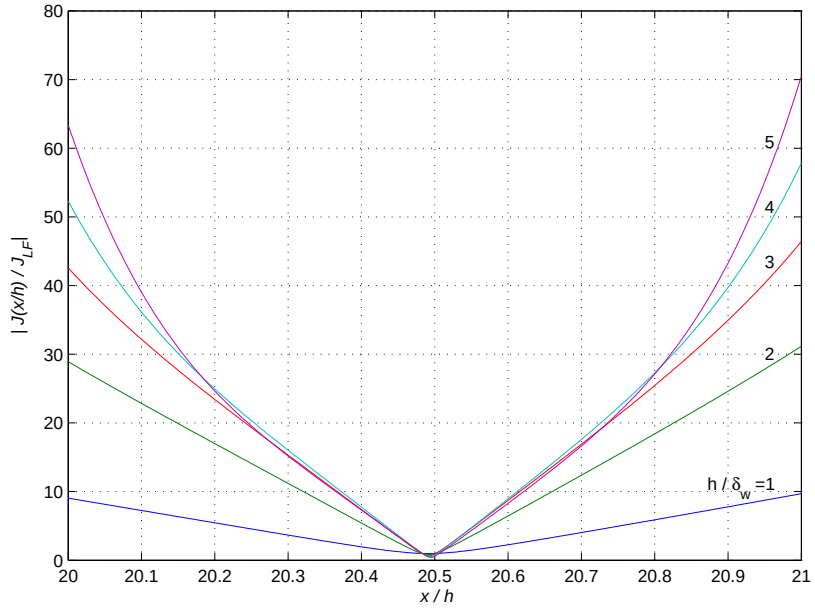

Figure 2.25: The magnitude of the normalized current density for $n = 10$.

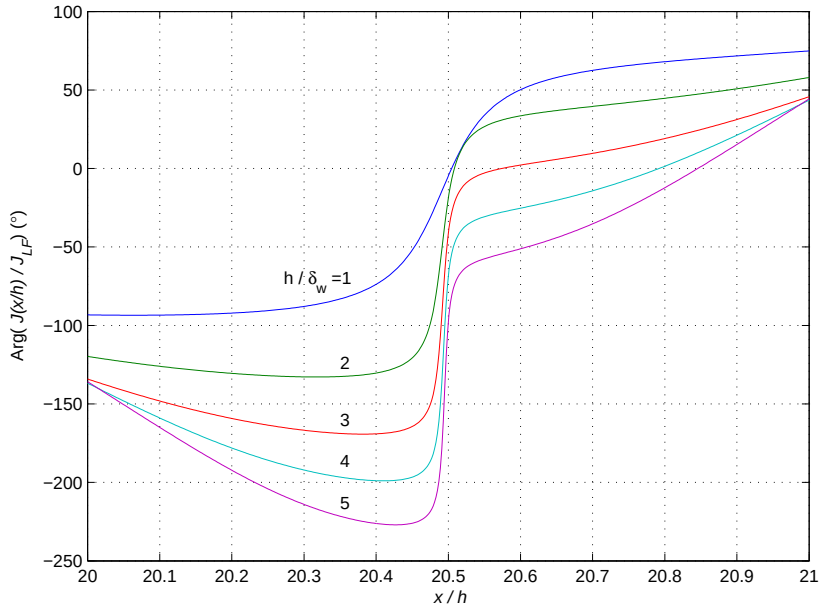

Figure 2.26: The phase of the normalized current density for $n = 10$.

2.5 Field Analysis

In the plots it can be observed that the degree to which the fields penetrate the conducting layers decreases as the frequency increases (and the skin depth decreases). Whereas the magnetic field intensity at the inner and outer surfaces of a given layer does not change with frequency, the electric field at the surfaces increases with increasing frequency. Because it is proportional to the electric field, the current density also increases at the surfaces with increasing frequency and thus more current flows near the surfaces and less near the center of the conductor. This is of course the skin effect.

The magnitudes of the magnetic field intensity, current density, and electric field are greater at the outer surface than the inner surface and this is the proximity effect. The ratio of the magnetic field intensity at the outer surface to that at the inner surface is, from (2.10) and (2.11),

$$\frac{\tilde{H}(x_{n_o})}{\tilde{H}(x_{n_i})} = \frac{n}{n-1}\,, \tag{2.21}$$

and the same ratio for the current density and electric field is found by plugging x_{n_o} and x_{n_i} into (2.18):

$$\frac{\tilde{J}(x_{n_o})}{\tilde{J}(x_{n_i})} = \frac{\tilde{E}(x_{n_o})}{\tilde{E}(x_{n_i})} = \frac{n\cosh\gamma h - n + 1}{n - (n-1)\cosh\gamma h}\,. \tag{2.22}$$

Note that this latter ratio is a complex value, the magnitude of which is the ratio of the amplitudes and the phase of which is the difference in phases.

Also of interest is what happens to the fields and current density in the outer layers as more and more layers are added. By taking the limit of (2.21) and (2.22) as the layer number goes to infinity we see that

$$\lim_{n\to\infty} \frac{\tilde{H}(x_{n_o})}{\tilde{H}(x_{n_i})} = 1$$

and

$$\lim_{n\to\infty} \frac{\tilde{J}(x_{n_o})}{\tilde{J}(x_{n_i})} = \lim_{n\to\infty} \frac{\tilde{E}(x_{n_o})}{\tilde{E}(x_{n_i})} = -1\,.$$

Thus the magnetic field intensity at the surfaces are nearly equal for an outer layer of a device with many layers and the current density and electric field at the surfaces are of equal magnitude but are 180° out of phase.

In looking at the plots one might notice that, as the layer number increases, they seem to converge to a definite form, noting however that the magnitude of both fields appears to increase as the layer number increases. A quick glance at (2.16) and (2.18) will show that the magnitudes of both fields do indeed increase without bound as the layer number increases. This difficulty is surmounted by

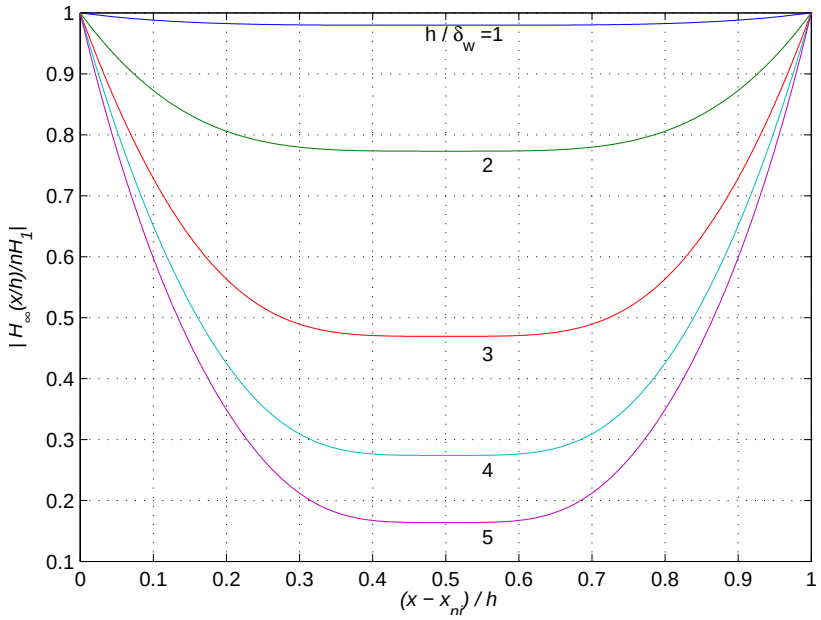

Figure 2.27: The magnitude of the form of the normalized magnetic field intensity in an infinite layer.

further normalizing the normalized fields expressed in (2.19) and (2.20) by the layer number and taking the limit as the layer number goes to infinity. The resulting equations,

$$H_\infty(x/h) \equiv \lim_{n\to\infty} \frac{\tilde{H}(\frac{x}{h})}{nH_1} = -\frac{\sinh\kappa\alpha + \sinh\kappa\beta}{\sinh\kappa\epsilon}$$

and

$$J_\infty(x/h) \equiv \lim_{n\to\infty} \frac{\tilde{J}(\frac{x}{h})}{nJ_{LF}} = \lim_{n\to\infty} \frac{\tilde{E}(\frac{x}{h})}{nE_{LF}} = \kappa\epsilon\frac{\cosh\kappa\alpha - \cosh\kappa\beta}{\sinh\kappa\epsilon}$$
$$E_\infty(x/h) \equiv \lim_{n\to\infty} \frac{\tilde{E}(\frac{x}{h})}{nE_{LF}} = J_\infty(x/h)\,,$$

express the forms to which the fields and current density converge with increasing layer number.

Magnitude and phase plots of these field forms in an infinite layer are shown in Fig 2.27 through Fig. 2.30, again for various frequencies and $\eta = 1$. As can be seen in the plots, the magnetic field intensity exhibits an even symmetry with respect to the center of the layer while the electric field and current density exhibit an odd symmetry if the magnitude and phase are taken together. Note the phase discontinuity in the phase of the current density and electric field. The physical field and current density, however, are continuous because, at the point of phase discontinuity, their magnitudes are zero, thus there is a smooth transition from what could be thought of as a positive value to a negative one. It is also evident here why the currents within the layers are considered

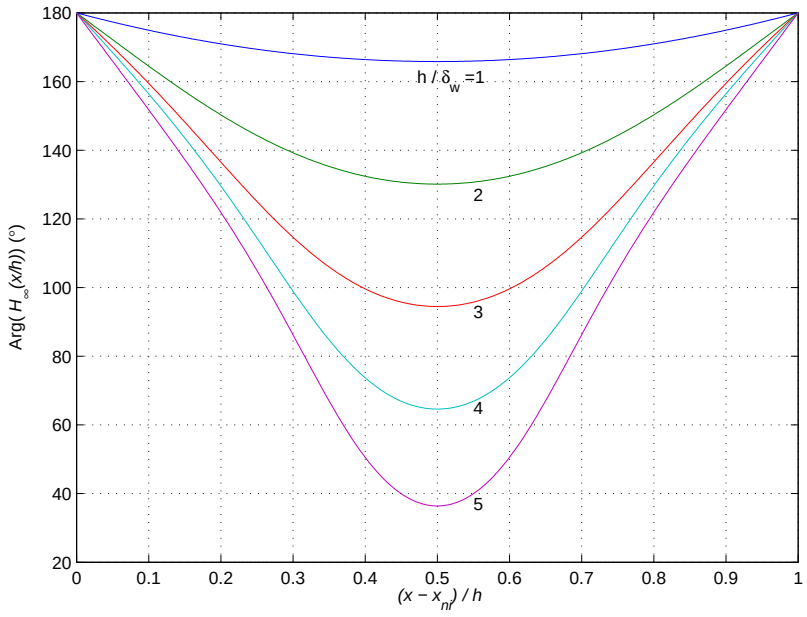

Figure 2.28: The phase of the form of the normalized magnetic field intensity in an infinite layer.

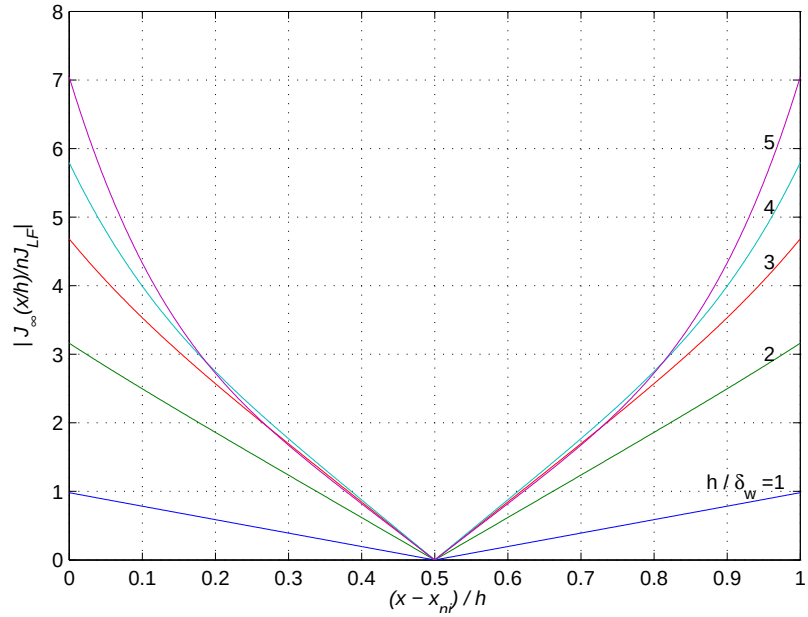

Figure 2.29: The magnitude of the form of the normalized current density in an infinite layer.

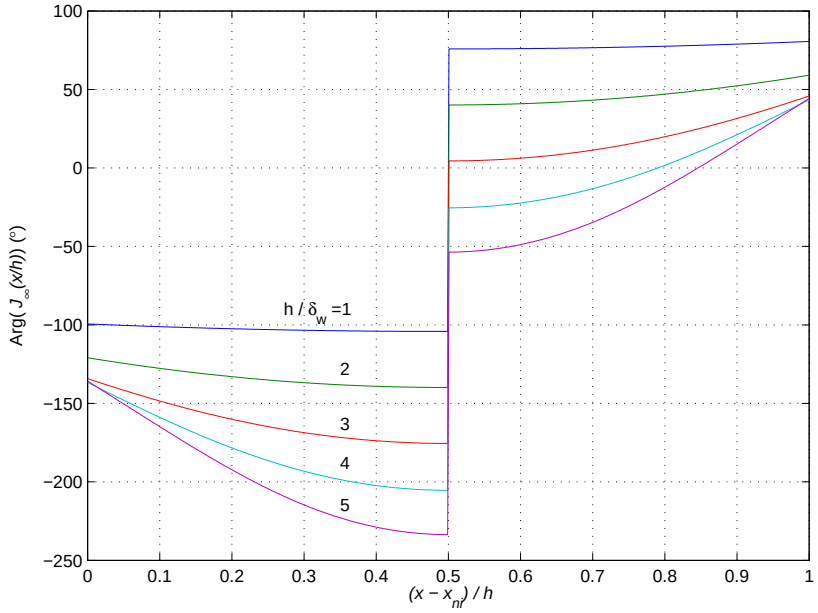

Figure 2.30: The phase of the form of the normalized current density in an infinite layer.

eddy currents: because on one side of the layer you have current flowing and, on the opposite side, it flows in the opposite direction (i.e. they are 180° out of phase) thereby returning.

One thing that the astute observer might notice here is that, because it has odd symmetry, if one were find the total current in an infinite layer by integrating the current density, the result would be zero current. This seems to be in conflict with our initial requirement that the total current in each layer is I (where I is generally not zero). The reason for this is that, in any given layer, the nonzero total current I comes from the fact that the current density is greater at the outer surface than at the inner surface, with most of the current density in the inner half of the layer cancelling that in outer half. This difference at the surfaces becomes less and less of the general magnitude of the current density until, in an infinite layer, it disappears and we are left only with eddy currents. This is how the losses can increases (since they are concerned only with the square of the current, and thus do not cancel but rather add together) while the total current flowing in the layer remains the same. Though this analysis is valid in this model, it should be noted that it has been shown in [Robert and Mathys 1998] that Dowell's model (i.e. this model) is less accurate as the number of layers increases, at least regarding the total power losses.

As the frequency of the current is increased the fields and current density do not converge to a definite form as they do when the layer number is increased. Rather the magnitudes of the fields and current are pushed further and further towards the surfaces of the conductor, creating greater losses

until, at a hypothetical infinite frequency, all the current flows within infinitesimally thin slivers at the inner and outer surfaces and the fields only penetrate the conductor as deep as these slivers.

We can, however gain some insight into what happens inside the conductor as the frequency increases (and the skin depth decreases). Let us begin by looking again at equation (2.19), i.e. the normalized magnetic field intensity:

$$\begin{aligned}\frac{\tilde{H}(\frac{x}{h})}{H_1} &= \frac{(1-n)\sinh\kappa\beta - n\sinh\kappa\alpha}{\sinh\kappa\epsilon} \\ &= \frac{(1-n)\sinh(\beta+j\beta) - n\sinh(\alpha+j\alpha)}{\sinh\kappa\epsilon}\,.\end{aligned}$$

Recalling that, for arbitrary real or complex a and b,

$$\sinh(a+b) = \sinh a\cosh b + \cosh a\sinh b\,,$$

we have

$$\begin{aligned}\frac{\tilde{H}(\frac{x}{h})}{H_1} = \frac{1}{\sinh\kappa\epsilon}\Big[&(1-n)(\sinh\beta\cosh j\beta + \cosh\beta\sinh j\beta) \\ &- n(\sinh\alpha\cosh j\alpha + \cosh\alpha\sinh j\alpha)\Big] \\ \frac{\tilde{H}(\frac{x}{h})}{H_1} = \frac{1}{\sinh\kappa\epsilon}\Big[&(1-n)(\sinh\beta\cos\beta + j\cosh\beta\sin\beta) \\ &- n(\sinh\alpha\cos\alpha + j\cosh\alpha\sin\alpha)\Big]\,.\end{aligned}$$

Here we have a combination of trigonometric functions of α and β multiplied by hyperbolic functions of the same variables. Since α and β are linear functions of the spatial variable x, this can be interpreted as spatial waves that are enveloped by the hyperbolic functions.

Fig. 2.31 shows a plot of the physical magnetic field intensity and the spatial waves can clearly be seen. This plot is for layer $n = 5$ with $h/\delta_w = 60$ and $\eta = 1$ and, because the envelope of these waves decays so rapidly from the surfaces, it has been scaled exponentially so that the waves are more clearly shown. To determine the wavelength of these waves we need only determine the period of the trigonometric functions, i.e. the difference in x when their argument differs by 2π.

To this end let us first find the wavelength when the argument is α:

$$\begin{aligned}\alpha &= \epsilon\frac{x_0 - x_{n_i}}{h} = 0 \\ \therefore\ x_0 &= x_{n_i}\end{aligned}$$

and

$$\begin{aligned}\alpha &= \epsilon\frac{x_{2\pi} - x_{n_i}}{h} = 2\pi \\ \therefore\ x_{2\pi} &= \frac{2\pi h}{\epsilon} + x_{n_i}\,.\end{aligned}$$

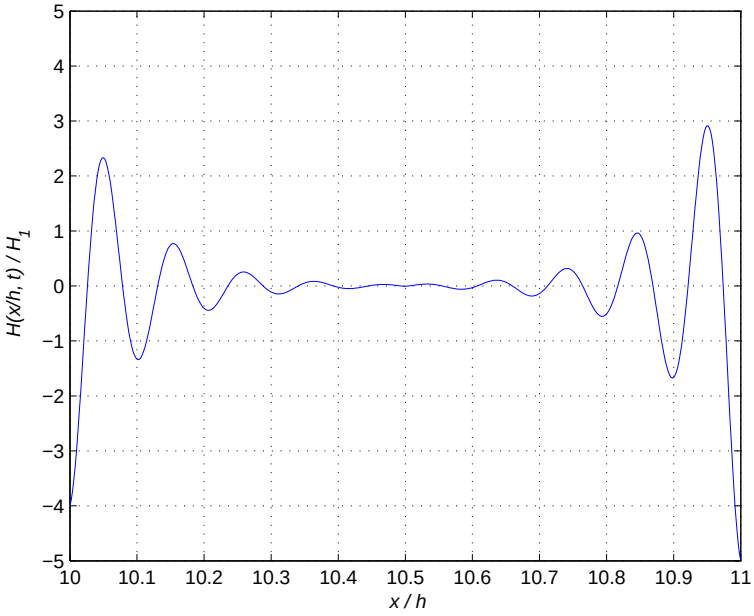

Figure 2.31: The magnetic field intensity throughout a layer, which shows the spatial waves that develop at high frequencies.

Thus the wavelength is

$$\lambda_\alpha = x_{2\pi} - x_0 = \frac{2\pi h}{\epsilon}\,.$$

When the argument is β,

$$\beta = \epsilon\frac{x_{n_o} - x_0}{h} = 0$$

$$\therefore\ x_0 = x_{n_o}$$

and

$$\beta = \epsilon\frac{x_{n_o} - x_{2\pi}}{h} = 2\pi$$

$$\therefore\ x_{2\pi} = x_{n_o} - \frac{2\pi h}{\epsilon}\,.$$

Thus the wavelength is in this case

$$\lambda_\beta = x_{2\pi} - x_0 = -\frac{2\pi h}{\epsilon}\,.$$

So we can say then that the wavelength of these waves, regardless of their trigonometric argument, is

$$\lambda = \frac{2\pi h}{\epsilon} = \frac{2\pi\delta_w}{\sqrt{\eta}}\,,$$

or $2\pi/\epsilon$ in space normalized to the height of the layer. While it would be difficult to show analytically, it turns out that these waves propagate in space towards the center of the conductor, i.e. the wave in the inner half of the layer propagates outward while that in the outer half propagates inward. It can be shown that similar waves develop in the electric field and current density as well and propagate in the same manner.

2.6 Power Density

By Joule's law, the time-averaged power density within a layer is

$$P_d(x) = \frac{1}{2}\rho_w \tilde{J}\tilde{J}^* = \frac{1}{2}\rho_w |\tilde{J}|^2 \,.$$

Substituting (2.17) into this and simplifying we get

$$\boxed{\begin{aligned} P_d(x) = P_{d(LF)} \frac{2\epsilon^2}{\cosh 2\epsilon - \cos 2\epsilon} \big[& n^2(\cosh 2\alpha + \cos 2\alpha) \\ & + (n-1)^2(\cosh 2\beta + \cos 2\beta) \\ & - 2n(n-1)(\cosh\epsilon\cos\zeta + \cosh\zeta\cos\epsilon)\big] \,, \end{aligned}} \tag{2.23}$$

where the power density at low frequencies is

$$P_{d(LF)} \equiv \frac{1}{2}\rho_w J_{LF}^2 = \frac{\rho_w I^2}{2w^2h^2}$$

and the variable ζ is defined to be

$$\zeta \equiv \alpha - \beta \;= \frac{\epsilon}{h}\left(2x - x_{n_i} - x_{n_o}\right) \,,$$

noting also that

$$\epsilon = \alpha + \beta \,.$$

The algebra involved in this simplification is tedious and is shown in full in Appendix B. Plots of normalized power density are shown in Fig. 2.32 through Fig. 2.36 for the same layers for which the normalized fields were shown and, again, for various normalized frequencies h/δ_w and a solid conductor ($\eta = 1$). One can observe here the rapidity with which the power density increases as more layers are added, especially near the surfaces.

As the layer number approaches infinity, the power density approaches a definite form though, like the current density, its magnitude increases indefinitely. This form can be found in similar fashion by normalizing the power density again with respect to the layer number squared and taking the limit:

$$\begin{aligned} \lim_{n\to\infty} \frac{P_d(\frac{h}{\delta_w})}{n^2 P_{d(LF)}} = \frac{2\epsilon^2}{\cosh 2\epsilon - \cos 2\epsilon} \big[& \cosh 2\alpha + \cos 2\alpha + \cosh 2\beta \\ & + \cos 2\beta - 2\cosh\epsilon\cos\zeta - 2\cosh\zeta\cos\epsilon\big] \,. \end{aligned} \tag{2.24}$$

A plot of this form is shown in Fig. 2.37. From (2.24) it is clear that this form exhibits even symmetry with respect to the center of the layer, a fact which can also be deduced by noting that the power density is proportional to the square of the oddly symmetric current density.

As the frequency is increased, the power density, like the fields and current density, does not approach a definite form but the power density at the surfaces increases indefinitely and more and more power is dissipated near the surfaces. The spatial waves that develop in the fields and current density cause half-waves in the instantaneous power density since the current density is squared. However, the expressions deduced and plotted here are the time-averaged power density and thus these half-waves do not appear.

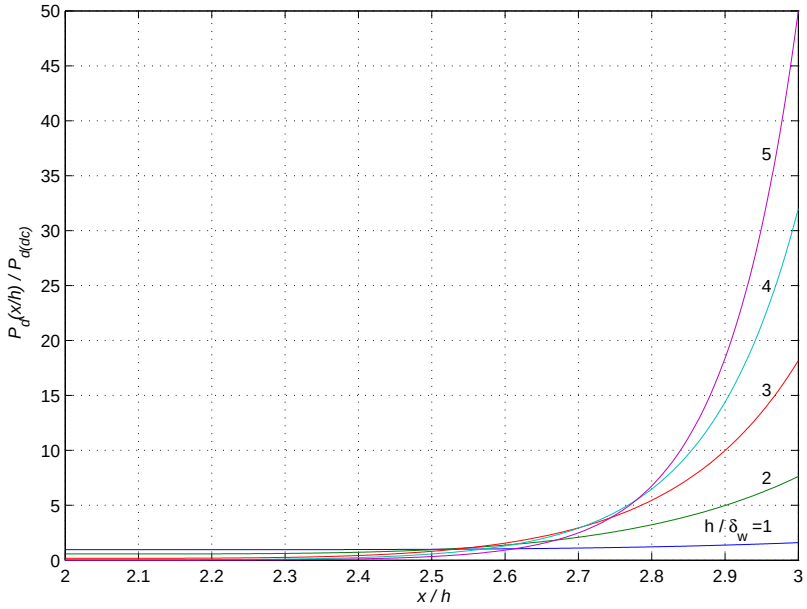

Figure 2.32: Normalized power density within layer $n = 1$.

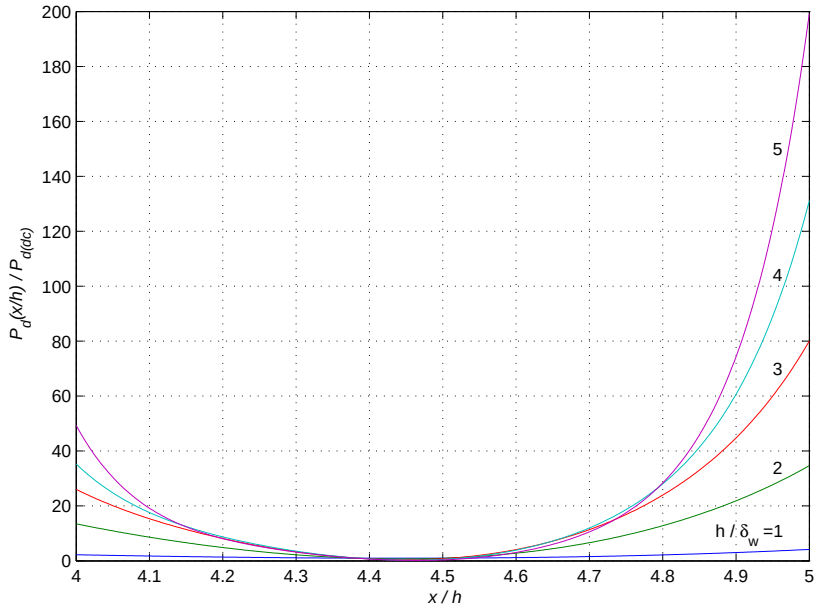

Figure 2.33: Normalized power density within layer $n = 2$.

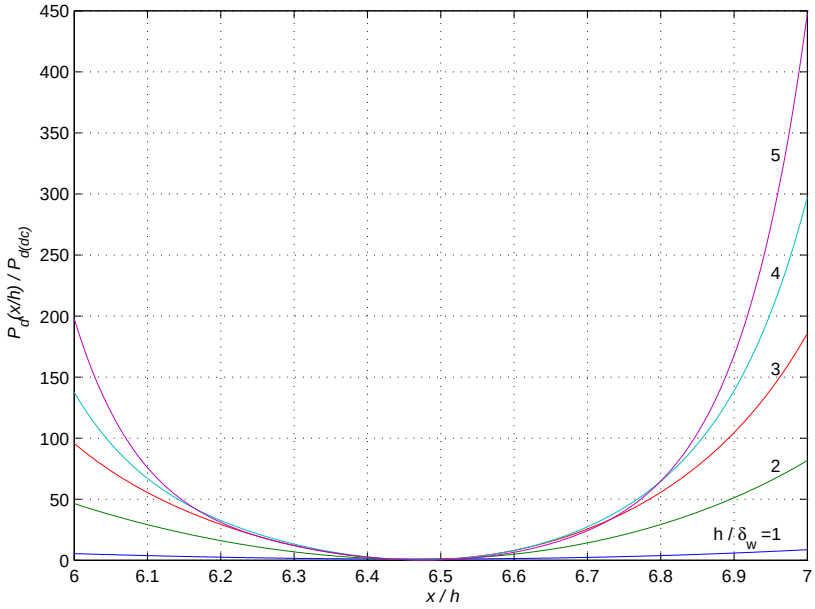

Figure 2.34: Normalized power density within layer $n = 3$.

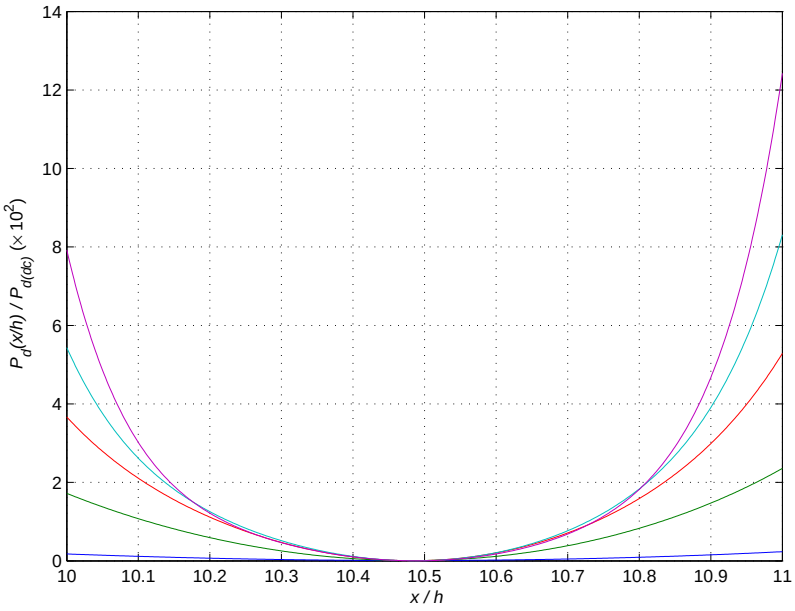

Figure 2.35: Normalized power density within layer $n = 5$.

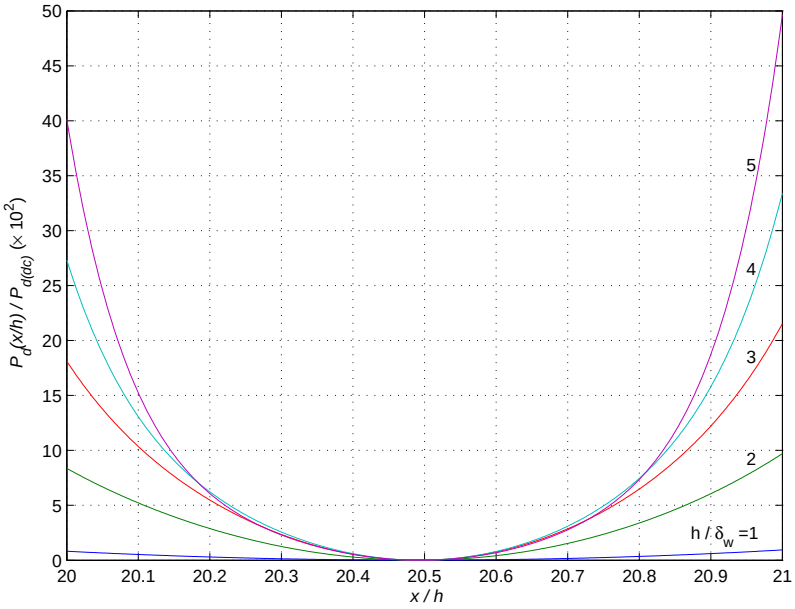

Figure 2.36: Normalized power density within layer $n = 10$.

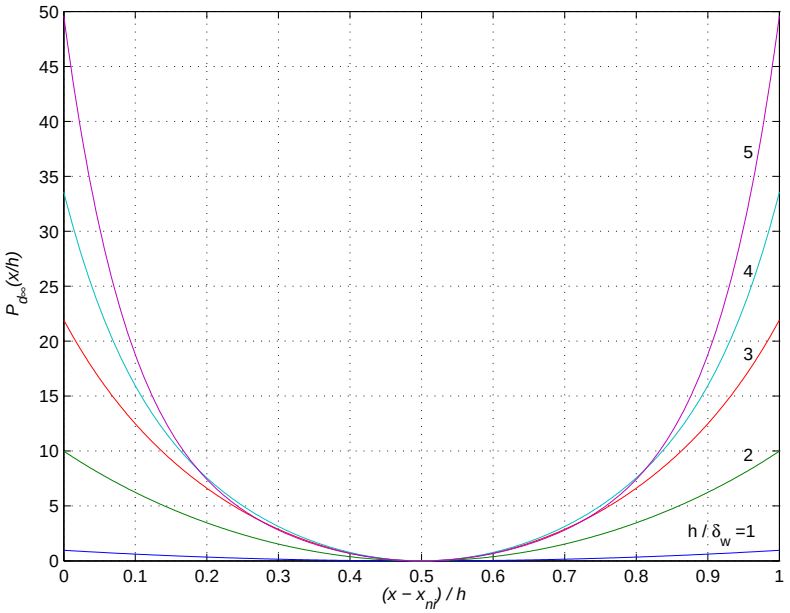

Figure 2.37: The form of the normalized power density within an infinite layer.

2.7 Total Power Loss

To find the total power losses we could integrate the power densities of each layer and then sum them together. However, it turns out to be simpler to use the Poynting theorem and it does not require the tedious algebra involved with finding the power density if one is only concerned with the total losses. This equivalence is verified in Appendix C. In integral form, the Poynting theorem states that

$$\oint_S (\mathbf{E} \times \mathbf{H}) \cdot d\mathbf{S} = -\int_V \left(\mathbf{E} \cdot \mathbf{J} + \frac{\partial}{\partial t} \frac{1}{2} \epsilon_0 E^2 + \frac{\partial}{\partial t} \frac{1}{2} \mu_0 H^2 \right) dv \,. \tag{2.25}$$

The first term on the right side represents the power dissipated in the volume and the second and third terms represent the change in the energy stored in the electric and magnetic fields, respectively. If the vectors are phasors, as they are in our case, then (2.25) takes the form

$$\oint_S (\tilde{\mathbf{E}} \times \tilde{\mathbf{H}}^*) \cdot d\mathbf{S} = -\int_V \left(\sigma_w |\tilde{E}|^2 + j\omega\epsilon_0 |\tilde{E}|^2 + j\omega\mu_0 |\tilde{H}|^2 \right) dv \tag{2.26}$$

where the * superscript denotes the complex conjugate. Notice that the first term on the right side (power density determined in Section 2.6) is pure real and the second and third terms (the change in the energy stored in the fields) are pure imaginary. This integral is the complex power of the conductor. While technically not a phasor, this quantity is useful as we shall soon see. See Appendix D for a discussion of complex power and its meaning and relationship to the Poynting theorem.

In our case, the Poynting vector $\mathbf{S} = \tilde{\mathbf{E}} \times \tilde{\mathbf{H}}^*$ points in the positive x direction and has a magnitude and phase of $\tilde{E}(x)\tilde{H}^*(x)$. If we evaluate the integral on the left hand side of (2.26) for a single turn in the nth layer and equate it to the negative complex power (the right hand side), we obtain

$$-P_{wn} = w l_T \tilde{E}(x_{n_o}) \tilde{H}^*(x_{n_o}) - w l_T \tilde{E}(x_{n_i}) \tilde{H}^*(x_{n_i}) \,, \tag{2.27}$$

where l_T is the mean turn length of the conductors, which is assumed to be the same for all layers. Note that only the inner and outer surfaces of the conductor contribute to the integral because, over the other four surfaces, the Poynting vector has no component normal to the surfaces. It turns out that $\tilde{H}^*(x_{n_i}) = \tilde{H}(x_{n_i})$ and $\tilde{H}^*(x_{n_o}) = \tilde{H}(x_{n_o})$, a result which is verified in Appendix E. So substituting (2.16) and (2.18) into (2.27) yields an expression for the complex power of a single turn

of the nth layer:

$$\begin{aligned}
P_{wn} &= wl_T\left[E(x_{n_i})H(x_{n_i}) - E(x_{n_o})H(x_{n_o})\right] \\
&= \frac{\rho_w wl_T H_1^2\gamma}{\eta}\left[-(n-1)\frac{n-(n-1)\cosh\gamma h}{\sinh\gamma h} + n\frac{n\cosh\gamma h-(n-1)}{\sinh\gamma h}\right] \\
&= \frac{\rho_w wl_T H_1^2\gamma}{\eta}\left[\frac{(2n^2-2n+1)\cosh\gamma h-(2n^2-2n)}{\sinh\gamma h} - \frac{\cosh\gamma h}{\sinh\gamma h} + \frac{\cosh\gamma h}{\sinh\gamma h}\right] \\
&= \frac{\rho_w wl_T H_1^2\gamma}{\eta}\left[(2n^2-2n)\frac{\cosh\gamma h-1}{\sinh\gamma h} + \coth\gamma h\right] \\
P_{wn} &= \frac{\rho_w l_T N_t I^2\gamma}{b}\left[\coth\gamma h + 2n(n-1)\tanh\frac{\gamma h}{2}\right].
\end{aligned}$$

Note that this complex power could have been determined by evaluating the integral on the right side of (2.26), but this would have been considerably more tedious.

Because the fields are identical in all the turns of the nth layer, the complex power associated with that layer is simply

$$P_n = N_t P_{wn} = \frac{\rho_w l_T N_t^2 I^2\gamma}{b}\left[\coth\gamma h + 2n(n-1)\tanh\frac{\gamma h}{2}\right]. \tag{2.28}$$

To find the complex power of the entirety of the winding, we sum the powers of each layer:

$$\begin{aligned}
P &= \sum_{n=1}^{m} P_n \\
&= \frac{\rho_w l_T N_t^2 I^2\gamma}{b}\sum_{n=1}^{m}\left[\coth\gamma h + 2n(n-1)\tanh\frac{\gamma h}{2}\right]
\end{aligned} \tag{2.29}$$

where m is the total number of layers. Recalling that

$$\sum_{n=1}^{m} n = \frac{m(m+1)}{2}$$

and

$$\sum_{n=1}^{m} n^2 = \frac{m(m+1)(2m+1)}{6},$$

(2.29) evaluates to

$$\begin{aligned}
P &= \frac{\rho_w l_T N_t^2 I^2\gamma}{b}\left[m\coth\gamma h + 2\left(\frac{m(m+1)(2m+1)}{6} - \frac{m(m+1)}{2}\right)\tanh\frac{\gamma h}{2}\right] \\
P &= \frac{\rho_w l_T N_t^2 I^2\gamma m}{b}\left[\coth\gamma h + \frac{2(m^2-1)}{3}\tanh\frac{\gamma h}{2}\right].
\end{aligned} \tag{2.30}$$

At low frequencies ($\delta_w \gg h$) or dc, resistance of the inductor is reasoned to be

$$R_{LF} \equiv \frac{\rho_w l_T N_t m}{wh} = \frac{\rho_w l_T N_t^2 m}{\eta h b},$$

and the power dissipation is

$$P_{LF} \equiv R_{LF} I^2 = \frac{\rho_w l_T N_t^2 I^2 m}{\eta h b} \,. \tag{2.31}$$

The complex high frequency power (2.30) can then be expressed in terms of the low frequency power:

$$P = P_{LF} F \,, \tag{2.32}$$

where the complex HF-to-LF (high frequency-to-low frequency) ratio factor is

$$F \equiv \eta\gamma h \left[\coth \gamma h + \frac{2(m^2-1)}{3} \tanh \frac{\gamma h}{2} \right] .$$

For ac, the average power dissipated in the windings is equal to half the real part of (2.32):

$$P_{av} = \frac{1}{2} \Re\{P\} = \frac{1}{2} P_{LF} \Re\{F\}$$

$$\boxed{P_{av} = \frac{1}{2} P_{LF} \eta\epsilon \left[\frac{\sinh 2\epsilon + \sin 2\epsilon}{\cosh 2\epsilon - \cos 2\epsilon} + \frac{2(m^2-1)}{3} \frac{\sinh \epsilon - \sin \epsilon}{\cosh \epsilon + \cos \epsilon} \right] .} \tag{2.33}$$

See Appendix F for elaboration on the splitting of F into its real and imaginary parts.

2.8 Impedance

We can use the complex power to find the impedance of the winding and therefore of the device. In general, the complex power of a conductor is equal to

$$P = \tilde{V} \tilde{I}^* = Z \tilde{I} \tilde{I}^* = Z |\tilde{I}|^2 \,.$$

Therefore, the impedance, in our case, is

$$Z = \frac{P}{I^2} = \frac{\rho_w l_T N_t^2 \gamma m}{b} \left[\coth \gamma h + \frac{2(m^2-1)}{3} \tanh \frac{\gamma h}{2} \right] .$$

It should be noted that this is the impedance due only to the winding space itself. The resistive (real) part is therefore complete, however the reactive (imaginary) part represents the inductance only due to the fields inside the windings. The complete inductance would also include inductance due to the fields in the interlayer gaps, the gaps between turns in each layer, and the core.

Like the power, the impedance can be expressed in terms of resistance at low frequencies and the complex HF-to-LF ratio:

$$Z = R_{LF} F = R_{LF} \eta\gamma h \left[\coth \gamma h + \frac{2(m^2-1)}{3} \tanh \frac{\gamma h}{2} \right] . \tag{2.34}$$

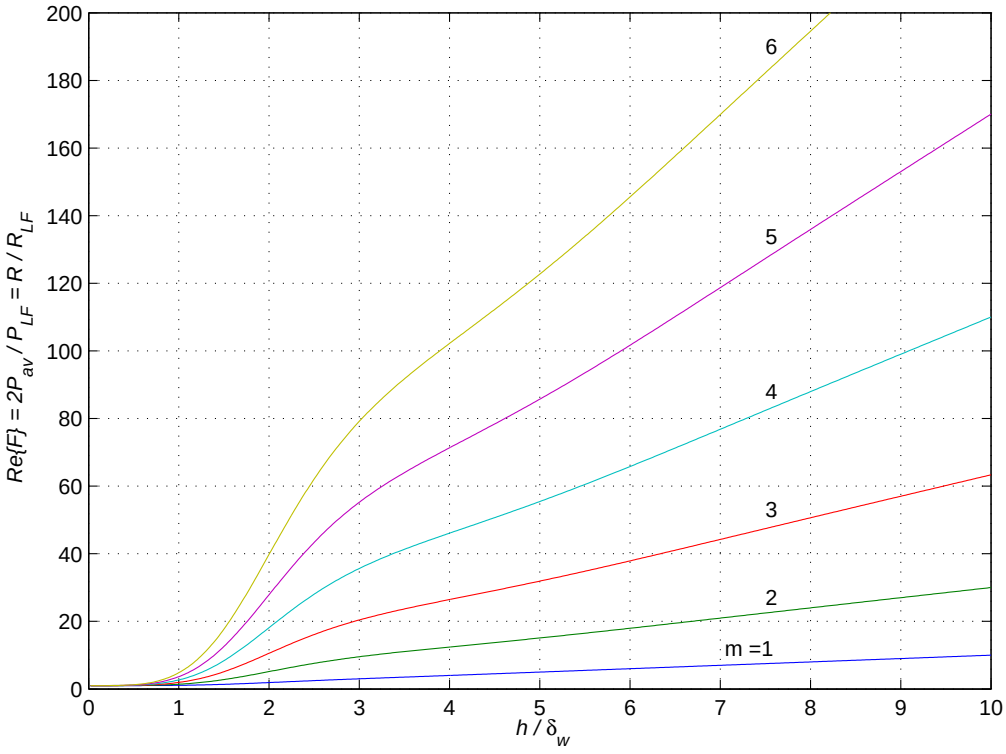

Figure 2.38: Normalized high-frequency resistance as a function of w/δ_w for various number of layers. This is also twice the ratio of the average high frequency power loss to the low frequency power loss.

The high frequency resistance is the real part of the impedance (2.34):

$$R = \Re\{Z\} = R_{LF}\Re\{F\}$$

$$\boxed{R = R_{LF}\eta\epsilon\left[\frac{\sinh 2\epsilon + \sin 2\epsilon}{\cosh 2\epsilon - \cos 2\epsilon} + \frac{2(m^2-1)}{3}\frac{\sinh\epsilon - \sin\epsilon}{\cosh\epsilon + \cos\epsilon}\right].} \tag{2.35}$$

This is Dowell's equation with a slight slight but important difference, which is discussed later in Section 5.1. Notice that

$$\frac{2P_{av}}{P_{LF}} = \frac{R}{R_{LF}} = \Re\{F\}\,. \tag{2.36}$$

A plot of this normalized power and resistance is shown in Fig. 2.38 for various number of layers. Again, this is for solid layers ($\eta = 1$).

3

Power Losses and Winding Resistance in Transformers

3.1 General Deductions

Next we shall discuss multilayer transformers where, in addition to the primary winding, there is a secondary winding that may or may not be interleaved in some way with the primary winding. Consider the winding configuration shown in Fig. 3.1, which has been chosen arbitrarily and in which the single, rectangular conductors have been replaced with a foil only for compactness and simplicity in the figure as the analysis will be still for separate conductors. The coordinate system and the geometric parameters are the same as in Chapter 2 and the same assumptions and neglect of edge effects apply here as well.

For this deduction we will introduce a second boundary condition that was not used in the inductor case. We shall again assume that the magnetic field intensity is zero within the core (an ideal core) and therefore also at the inner surface of the innermost layer. We shall also assume that the core material surrounds the device and the magnetic field intensity at the outer surface of the outermost layer is also zero. Equivalently we could assume the magnetic field intensity to be zero at infinity (as is physically required in a non-radiating system) and the following Amperian loop to extends out to infinity.

Now the current in all the primary layers must be the same and similarly the current in the secondary layers must be as well, though the primary current is not necessarily equal to the secondary current. By considering an Amperian loop which extends from the core to outside the outermost

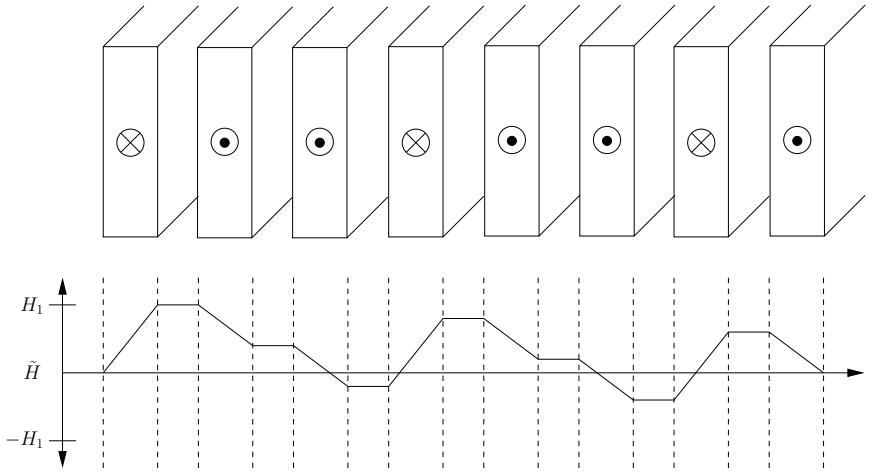

Figure 3.1: Arbitrarily chosen transformer winding configuration and associated magnetic field intensity at low frequencies.

layer and completely encloses all the layers, we obtain a relationship between the two currents:

$$0 = m_1 N_{t1} I_1 + m_2 N_{t2} I_2$$
$$\therefore \boxed{I_2 = -\frac{m_1 N_{t1}}{m_2 N_{t2}} I_1 \,,} \tag{3.1}$$

where the numeric subscripts indicate the primary or secondary quantities and the nomenclature is otherwise the same as before.

Evidently the current that must flow through the secondary winding is independent of the exact winding configuration and depends only on the relative number of layers and the number of turns of the primary and secondary windings. It is also independent of layer thicknesses. Fig. 3.1, in which $m_1 = 3$, $m_2 = 5$, and we let $N_{t1} = N_{t2}$, also shows the magnetic field for that configuration at low frequencies. Again H_1 is the magnetic field intensity between the first and second layers. To illustrate the independence of I_2 on the specific configuration, a different configuration and magnetic field diagram are shown in Fig. 3.2 with the same parameters (and thus the same I_2). Though the secondary current is independent of the winding configuration, clearly the magnetic field intensity (and therefore current density and power losses) is not.

Naturally Maxwell's equations and their general solution, i.e. the solution to the one dimensional Helmholtz equation given by (2.9), are valid within transformer layers. Thus, once the secondary current is found found via (3.1), the boundary conditions at the inner and outer surfaces of any layer can be found by using the appropriate Amperian loops. Once these boundary conditions are known, the fields and power losses within that layer can be determined for any configuration via (2.15) just as was done in the preceding chapter for inductors. Because of this, we shall forgo discussion of them

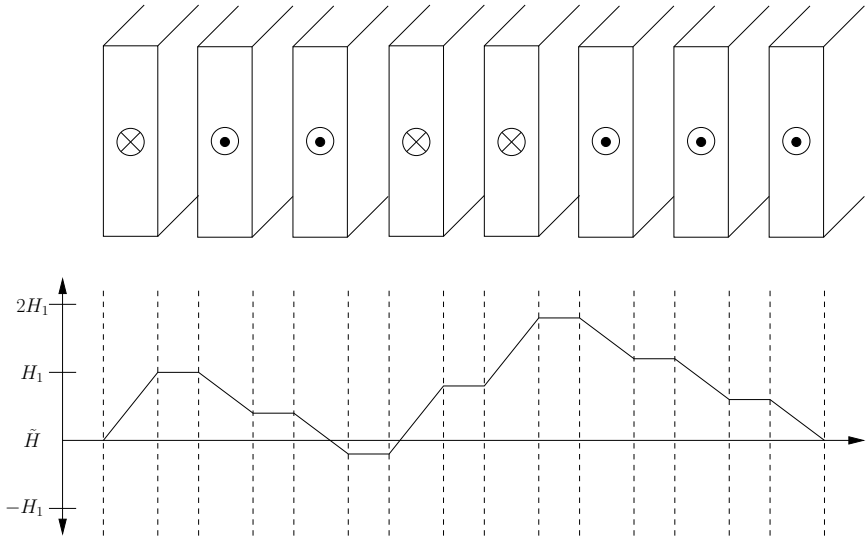

Figure 3.2: A second arbitrarily chosen transformer winding configuration and associated magnetic field intensity with the same parameters as Fig. 3.1.

and concern ourselves with the power losses and ac resistances. Let us now look at some frequently used special cases.

3.2 Non-interleaved Windings

Consider the non-interleaved transformer winding configuration shown in Fig. 3.3 in which all the primary layers are together on the inside and all the secondary layers are together outside of the primary layers. Note that the number of layers for each winding (i.e. m_1 and m_2) are not necessarily equal. Notice here that each set of windings (primary or secondary) when considered separately constitute exactly the same situation as described in Chapter 2, though the secondary winding is the opposite situation with respect to x. This observation means that we can simply use (2.33) to determine the time-averaged power losses in each section and then simply sum them together to get the total power losses in the windings of the transformer. This general sum can be used for the case in which the primary and secondary windings have completely different material and geometric parameters. Note also that the ac resistance seen at the primary terminals is just (2.35) for the primary winding and similarly for the secondary winding. However, as discussed in Appendix C, the Poynting theorem does not quite hold in our analysis and so we should use the power equation derived in that appendix. Equivalently we can divide (2.33) and the resistance equation (2.35) by the porosity factor η, as per the relation (5.1) to obtain the equations that would be derived by

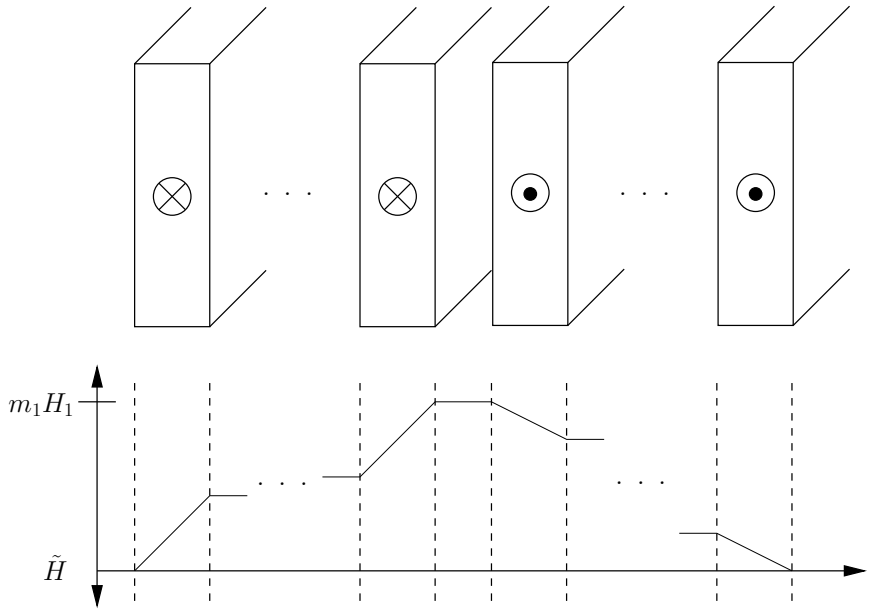

Figure 3.3: Transformer with non-interleaved windings and associated magnetic field intensity at low frequencies.

integrating the power density. This is what we shall do in the following discussion.

Let us look at the case in which the two windings are the same, i.e.

$$\begin{aligned} N_{t1} &= N_{t2} = N_t \\ \rho_{w1} &= \rho_{w2} = \rho_w \\ \therefore \delta_{w1} &= \delta_{w2} = \delta_w \\ \eta_1 &= \eta_2 = \eta \\ h_1 &= h_2 = h \\ \therefore \epsilon_1 &= \epsilon_2 = \epsilon \end{aligned} \tag{3.2}$$

and we can drop the subscripts, though again m_1 and m_2 are not necessarily equal. Summing the two power equations we have

$$P_{av} = \frac{1}{2}P_{LF1}\epsilon\left[F_1(\epsilon) + \frac{2(m_1^2-1)}{3}F_3(\epsilon)\right] + \frac{1}{2}P_{LF2}\epsilon\left[F_1(\epsilon) + \frac{2(m_2^2-1)}{3}F_3(\epsilon)\right], \tag{3.3}$$

where F_1 and F_3 are as defined in Appendix C. We note that, from (2.31), the low-frequency powers dissipated in each winding are

$$\begin{aligned} P_{LF1} &= \frac{\rho_w l_T N_t^2 I_1^2 m_1}{\eta h b} \\ P_{LF2} &= \frac{\rho_w l_T N_t^2 I_2^2 m_2}{\eta h b}\,. \end{aligned}$$

Substituting (3.1) into the secondary low-frequency power we get

$$P_{LF2} = \frac{\rho_w l_T N_t^2 I_1^2 m_1^2}{\eta h b m_2} = \frac{m_1}{m_2} P_{LF1}\,.$$

Applying this to (3.3) yields

$$\begin{aligned} P_{av} &= \frac{1}{2}P_{LF1}\epsilon\left[F_1(\epsilon) + \frac{2(m_1^2-1)}{3}F_3(\epsilon)\right] + \frac{1}{2}\frac{m_1}{m_2}P_{LF1}\epsilon\left[F_1(\epsilon) + \frac{2(m_2^2-1)}{3}F_3(\epsilon)\right] \\ &= \frac{1}{2}P_{LF1}\epsilon\left[F_1(\epsilon) + \frac{2(m_1^2-1)}{3}F_3(\epsilon) + \frac{m_1}{m_2}F_1(\epsilon) + \frac{2m_1(m_2^2-1)}{3m_2}F_3(\epsilon)\right] \\ \boxed{P_{av} &= \frac{1}{2}P_{LF1}\epsilon\left[\left(1+\frac{m_1}{m_2}\right)F_1(\epsilon) + \frac{2}{3m_2}(m_1^2m_2 + m_1m_2^2 - m_1 - m_2)F_3(\epsilon)\right]\,,} \end{aligned}$$

which is the total time-average power loss of the transformer referred to the low-frequency power loss in the primary winding. If we take the even more special case of $m_1 = m_2 = m$, then $P_{LF1} = P_{LF2} = P_{LF}$ and this equation collapses to

$$\begin{aligned} P_{av} &= \frac{1}{2}P_{LF}\epsilon\left[(1+\frac{m}{m})F_1(\epsilon) + \frac{2}{3m}(m^2m + mm^2 - m - m)F_3(\epsilon)\right] \\ &= P_{LF}\epsilon\left[F_1(\epsilon) + \frac{2(m^2-1)}{3}F_3(\epsilon)\right] \\ &= 2P_{av(inductor)}\,, \end{aligned} \tag{3.4}$$

which makes sense intuitively. The ac resistance of each winding is the same as that of an inductor having only the primary or secondary winding, which is given by (2.35).

3.3 Interleaved Windings

Consider now a transformer with purely interleaved windings as shown in Fig. 3.4. By necessity $m_1 = m_2 = m$, though we do not initially require that the windings have the same material and geometric properties. The current flowing through each winding are related by the following equation:

$$I_2 = -\frac{N_{t1}}{N_{t2}}I_1\,, \tag{3.5}$$

which is simply (3.1) with $m_1 = m_2$. Though the currents may not necessarily be equal, the magnitude of the total current flowing through a given layer is equal for all the layers with the current in secondary layers flowing in the opposite direction of that in the primary layers. This fact follows directly from (3.5) if one multiplies both sides by N_{t2}.

It is clear that, because the currents are equal and opposite in a given primary/secondary layer pair, the magnetic field intensity returns to zero on the inside and outside of a given pair. Equation

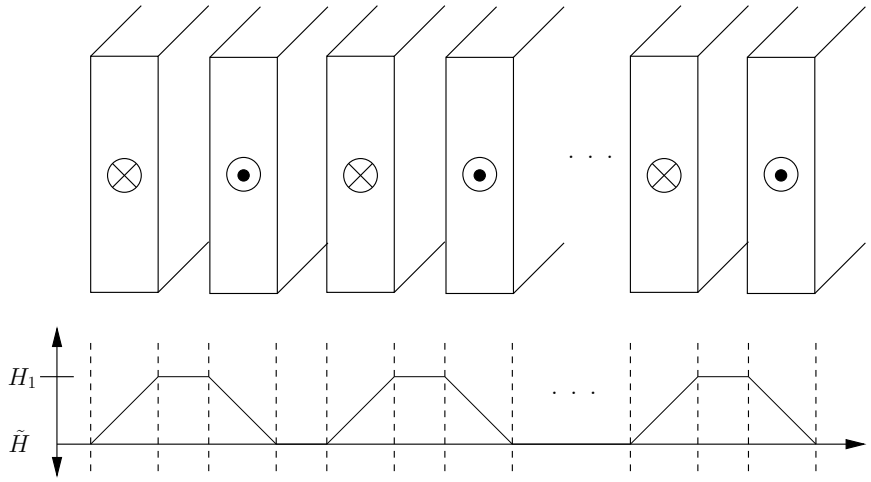

Figure 3.4: Transformer with purely interleaved windings and associated magnetic field intensity at low frequencies.

(2.28) gives the complex power in a given layer and it is apparent from the above deductions that both of the layers in a primary/secondary pair can be considered as the first ($n = 1$) layer where the magnetic field intensity is zero on one side and H_1 on the other. Applying this to (2.28) and putting it in terms of the total power loss at low-frequencies gives the complex power in each of the layers in a pair:

$$P_{11} = P_{LF1}\frac{h_1}{m}\gamma_1 \coth \gamma_1 h_1$$
$$P_{12} = P_{LF2}\frac{h_2}{m}\gamma_2 \coth \gamma_2 h_2 \,,$$

noting that the low-frequency powers and other constants are not necessarily equal since the windings do not have the same properties in general.

The total complex power of a primary/secondary pair is simply the sum $P_{11} + P_{12}$. Since there are m pairs, the total complex power of the device is given by

$$\begin{aligned} P &= m(P_{11} + P_{12}) \\ &= P_{LF1}h_1\gamma_1 \coth \gamma_1 h_1 + P_{LF2}h_2\gamma_2 \coth \gamma_2 h_2 \,. \end{aligned} \tag{3.6}$$

The time-averaged power dissipation in the device is of course $P_{av} = \Re\{P\}/2$ and, applying this to (3.6) and using the deductions in Appendix F, gives

$$\boxed{P_{av} = \frac{1}{2}\left[P_{LF1}\epsilon_1 F_1(\epsilon_1) + P_{LF2}\epsilon_2 F_1(\epsilon_2)\right] \,.}$$

If we again let the windings be the same, as explicitly stated in (3.2), then again $P_{LF1} = P_{LF2} = P_{LF}$

and the above equation collapses to

$$P_{av} = P_{LF}\epsilon F_1(\epsilon)\,. \tag{3.7}$$

As just discussed, the time-averaged power dissipated in either the primary or secondary winding is

$$P_{(av)w} = \frac{1}{2}P_{LFw}\epsilon_w F_1(\epsilon_w) \tag{3.8}$$

for different windings, where the w subscript is 1 or 2 for either the primary or secondary winding. From (2.36) we know that

$$R = R_{LF}\frac{2P_{av}}{P_{LF}}\,.$$

By (3.8), the resistance of the primary or secondary winding is thus

$$\boxed{R_w = R_{LFw}\epsilon_w F_1(\epsilon_w)\,.} \tag{3.9}$$

In the special case of identical windings these two powers and resistances are equal.

3.4 Comparison

Consider now two transformers with identical windings except that one is non-interleaved (with $m_1 = m_2 = m$) and the other is purely interleaved and in which the primary and secondary windings are the same. The powers dissipated in each device, given by (3.4) and (3.7), are

$$P_{av(non-int)} = P_{LF}\epsilon\left[F_1(\epsilon) + \frac{2(m^2-1)}{3}F_3(\epsilon)\right]$$
$$P_{av(int)} = P_{LF}\epsilon F_1(\epsilon)\,.$$

Note that the interleaved power dissipation does not depend at all on the total number of layers. In fact, it is clear that these equations are the same except that the non-interleaved power has an extra term which depends on the total number of layers. That extra term is due to the proximity effect and so interleaving the windings has completely mitigated it, resulting in lower power losses and resistances as compared to the analogous non-interleaved configuration.

If we wish to know just how much more the losses would be if we chose not to interleave the windings, we simply take the ratio of the two:

$$\frac{P_{av(non-int)}}{P_{av(int)}} = 1 + \frac{2(m^2-1)}{3}\frac{F_3(\epsilon)}{F_1(\epsilon)}$$
$$\boxed{\frac{P_{av(non-int)}}{P_{av(int)}} = 1 + \frac{2(m^2-1)}{3}\frac{(\cosh 2\epsilon - \cos 2\epsilon)(\sinh\epsilon - \sin\epsilon)}{(\sinh 2\epsilon + \sin 2\epsilon)(\cosh\epsilon + \cos\epsilon)}\,.} \tag{3.10}$$

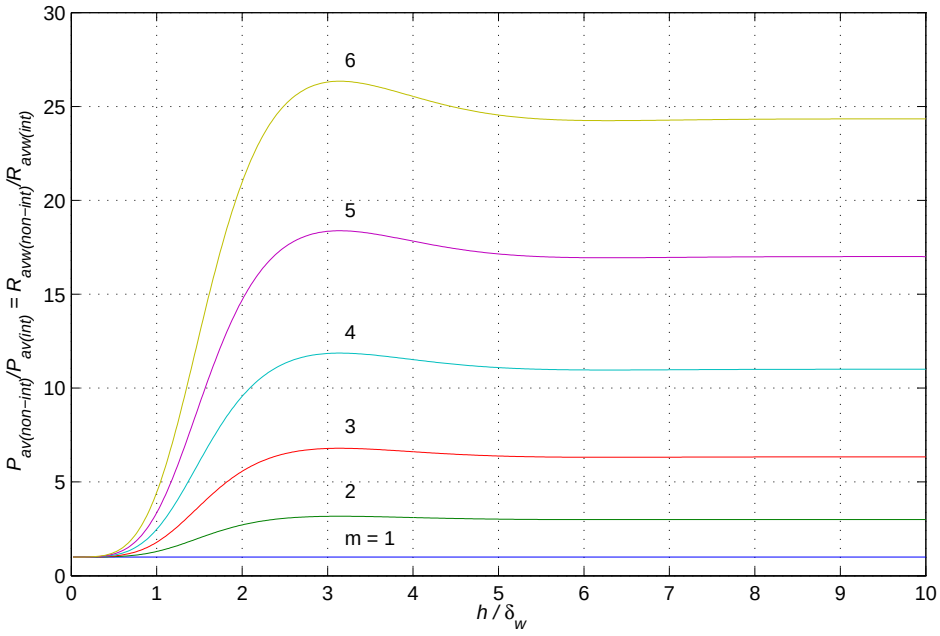

Figure 3.5: The ratio of power losses of a transformer with non-interleaved windings to that with interleaved windings for identical windings and $\eta = 1$.

As we have shown, the ac resistances of the primary or secondary windings are given by (2.35) for non-interleaved windings and (3.9) for interleaved windings. If we take the ratio of these we get the same result as the ratio of the power:

$$\frac{R_{(av)w(non-int)}}{R_{(av)w(int)}} = \frac{P_{av(non-int)}}{P_{av(int)}},$$

where m becomes m_w and ϵ becomes ϵ_w for the primary or secondary winding.

Clearly this ratio is a quadratic function of the number layers for a given ϵ. It might be interesting though to see how this ratio depends on ϵ, or rather h/δ_w. A plot of (3.10) in shown in Fig. 3.5 as a function of h/δ_w for various numbers of layers m. It is clear from the plot and equation that

$$\lim_{\frac{h}{\delta_w}\to\infty} \frac{P_{av(non-int)}}{P_{av(int)}} = \lim_{\frac{h}{\delta_w}\to\infty} \frac{R_{(av)w(non-int)}}{R_{(av)w(int)}} = 1 + \frac{2(m^2-1)}{3}.$$

Thus as the frequency increases (or equivalently the thickness of the layers increases) the normalized height of the layer is less important and the number of layers dominates the difference between non-interleaved and interleaved transformers. Note also that for $m = 1$ non-interleaved and interleaved windings are the same thus the ratio is unity.

4

Non-Ideal Core and Reduction of Power Losses by Layer Thickness Optimization

4.1 Non-Ideal Core

4.1.1 Inductors

In the previous discussions we assumed an ideal core for simplicity. Often times though the permeability of the core is low enough that the ideal approximation is not sufficient. Consider first an inductor the same as that shown in Fig. 2.1 except that the core has some finite permeability $\mu_r\mu_0$. The non-ideal core results in a nonzero magnetic field intensity at the innermost surface of the innermost layer and its effects on the analysis are nontrivial.

The effect of the core on the winding fields can be determined using the method of images, as is done in [Kutkut 1998a]. The method of images is applicable when there is a boundary between two regions with different constitutive parameters, i.e. different permittivities and/or permeabilities as is discussed in greater detail in Appendix G. In such a situation the different regions are replaced by a single region and sources on one side of the boundary are mirrored on the other side by image sources positioned at the reflection of the original sources across the boundary. In the case of a current current source, the current flowing through the image source is related to the current flowing at the original source by

$$I' = \frac{\mu_2 - \mu_1}{\mu_2 + \mu_1} I \,, \tag{4.1}$$

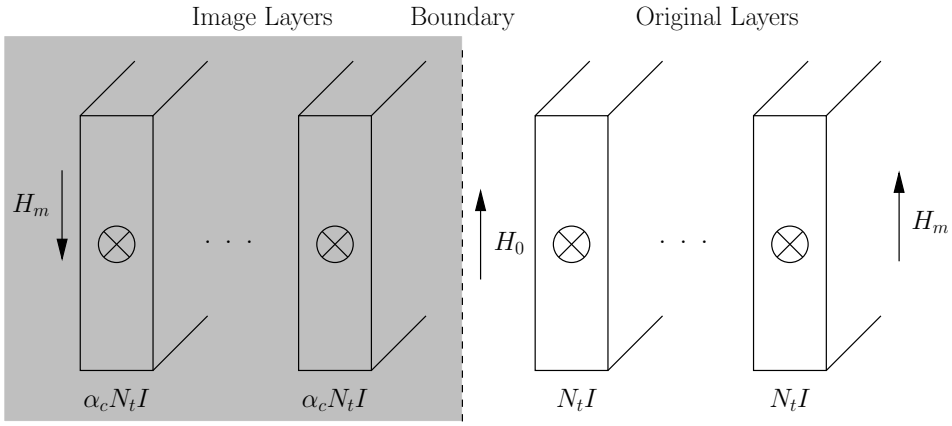

Figure 4.1: Inductor windings after applying the method of images. The gray region indicates where the solution is not valid.

where μ_1 is the permeability of the region in which the original sources reside and μ_2 is the permeability of the region containing the images. The solution of the resulting system is valid in the μ_1 region and is equivalent to the original problem.

In our case the resulting system is shown in Fig. 4.1 in which the display of individual windings has been suppressed for simplicity and each layer is shown as a single conductor. Each turn in the original layers carries a current I and so, according to (4.1) where $\mu_1 = \mu_0$ and $\mu_2 = \mu_r\mu_0$, the current through each image turn is

$$I' = \frac{\mu_r\mu_0 - \mu_0}{\mu_r\mu_0 + \mu_0} I$$
$$I' = \alpha_c I \,,$$

where we shall let

$$\alpha_c \equiv \frac{\mu_r - 1}{\mu_r + 1} \,.$$

The total current carried by each image layer is therefore $N_t I' = \alpha_c N_t I$ as shown in the figure.

The first step in determining the electromagnetic fields within the layers is to determine the boundary conditions of an arbitrary layer. To this end let us begin by determining the magnetic field intensity within the core H_0. The first thing we note here is that, as shown in Fig. 4.1, the magnetic field intensity outside the outermost layer H_m is the same as the magnetic field intensity at the outside of the image layers but in the opposite direction. The reason for this becomes apparent if one considers all the layers (both original and image) as a single conductor carrying a current of $mN_tI(\alpha_c + 1)$, which is valid when speaking only of the magnetic fields outside of all the layers. Then, by symmetry, the two magnetic fields at the outside must be equal and opposite.

These magnetic field intensities can then be simply determined by considering an Amperian loop around the entirety of the layers. Doing so results in

$$bH_m + bH_m = -mN_tI(\alpha_c + 1)$$
$$H_m = -\frac{m(\alpha_c + 1)}{2b} N_tI\,.$$

From this the magnetic field intensity in the core can be determined by integrating around another Amperian loop extending from the outside of the image layers to the innermost surface of the inner layer:

$$bH_m + bH_0 = -m\alpha_c N_tI$$
$$H_0 = -\frac{m\alpha_c N_tI}{b} + \frac{mN_tI(\alpha_c + 1)}{2b}$$
$$H_0 = -\frac{m(\alpha_c - 1)}{2b} N_tI\,.$$

We can now find the magnetic field intensities at the inner and outer surfaces of the nth layer using the Amperian loops shown in Fig. 2.6. For the outer surface

$$bH_0 - bH_{no} = nN_tI$$
$$H_{no} = -\frac{mN_tI(\alpha_c - 1)}{2b} - \frac{nN_tI}{b}$$
$$H_{no} = -\frac{m(\alpha_c - 1) + 2n}{2b} N_tI\,. \tag{4.2}$$

For the magnetic field intensity at the inner surface it suffices to substitute $n - 1$ for n in (4.2), resulting in

$$H_{ni} = -\frac{m(\alpha_c - 1) + 2n - 2}{2b} N_tI\,. \tag{4.3}$$

We are now equipped to find the magnetic field intensity within the nth by substituting (4.3) and (4.2) into (2.15):

$$\boxed{\tilde{H}(x) = -H_0' \frac{(\beta_c + 1)\sinh\kappa\alpha + (\beta_c - 1)\sinh\kappa\beta}{\sinh\kappa\epsilon}\,,}$$

where

$$H_0' \equiv \frac{N_tI}{2b}$$

and we let

$$\beta_c \equiv m(\alpha_c - 1) + 2n - 1\,.$$

Magnitude and phase plots of the magnetic field intensity are shown in Fig. 4.2 and Fig. 4.3,

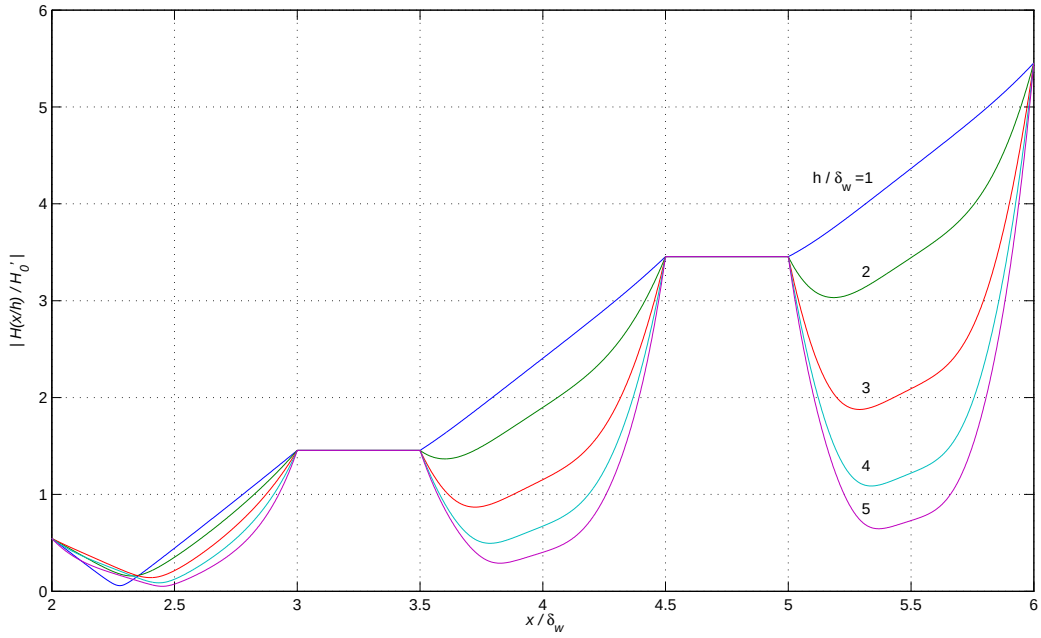

Figure 4.2: The magnitude of the normalized magnetic field intensity in the layers of an inductor with $m = 3$ layers, $\eta = 1$, and $\mu_r = 10$.

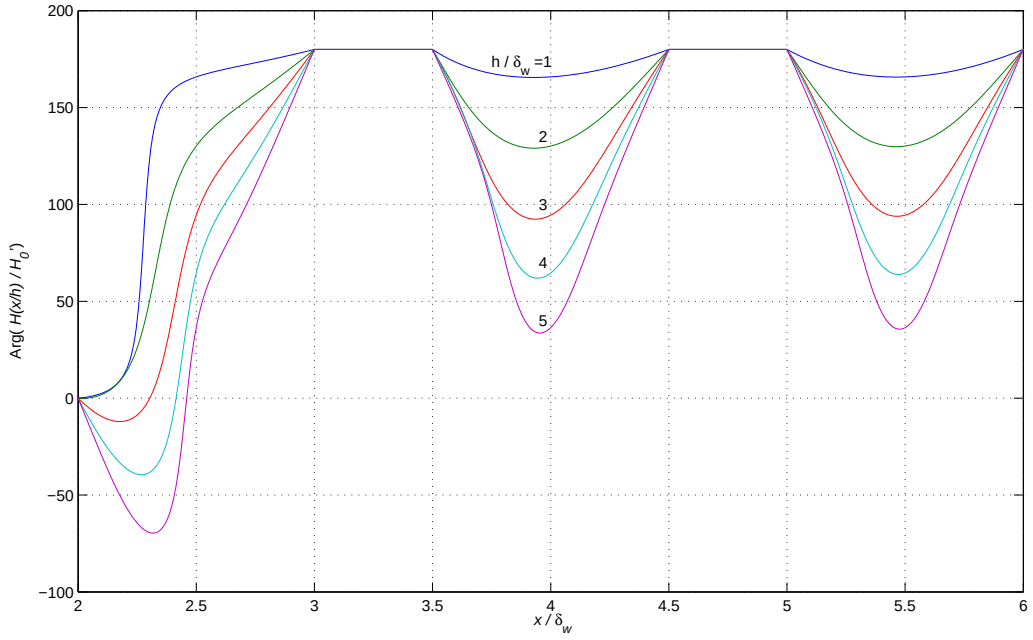

Figure 4.3: The phase of the normalized magnetic field intensity in the layers of an inductor with $m = 3$ layers, $\eta = 1$, and $\mu_r = 10$.

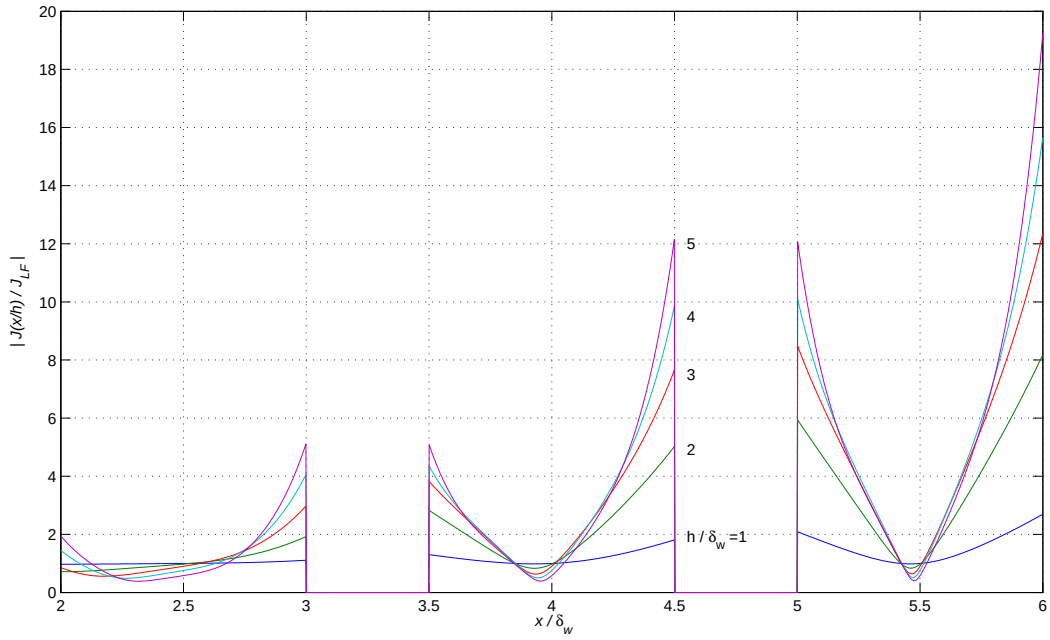

Figure 4.4: The magnitude of the normalized current density in the layers of an inductor with $m = 3$ layers, $\eta = 1$, and $\mu_r = 10$.

respectively for an inductor with $m = 3$ layers and $\eta = 1$ with $\mu_r = 10$ to emphasize the effect and for various h/δ_w. All three layers are shown and the dips in the magnitude plot are the locations of the layers with the flat parts being the space in between the layers. Compare this magnitude plot with the magnetic field intensity plots for an ideal core (Fig. 2.7 through Fig. 2.11) and note that the innermost layer is most affected by the non-ideal core, which makes sense since it is in closest proximity to the core.

The current density can again be found using (2.8), which results in

$$\boxed{\tilde{J}(x) = -\frac{1}{\eta}\frac{d\tilde{H}}{dx} = \frac{1}{2}J_{LF}\kappa\epsilon\frac{(\beta_c+1)\cosh\kappa\alpha - (\beta_c-1)\cosh\kappa\beta}{\sinh\kappa\epsilon}},$$

where $J_{LF} = 2H_0'/\eta h = I/wh$ is again the uniform current density at low frequencies. As before the electric field is

$$\tilde{E}(x) = E_{LF}\frac{\tilde{J}(x)}{J_{LF}}$$

for the same low-frequency electric field as before ($E_{LF} = \rho_w I/wh$). Magnitude and phase plots of the normalized current density and electric field are shown in Fig. 4.2 and Fig. 4.5, respectively for the same parameters that were used for the magnetic field intensity plots.

From the fields, the power losses can be determined using the Poynting theorem as was done in Section 2.7, though as discussed in Section 5.1 and Appendix C, we shall divide by the porosity

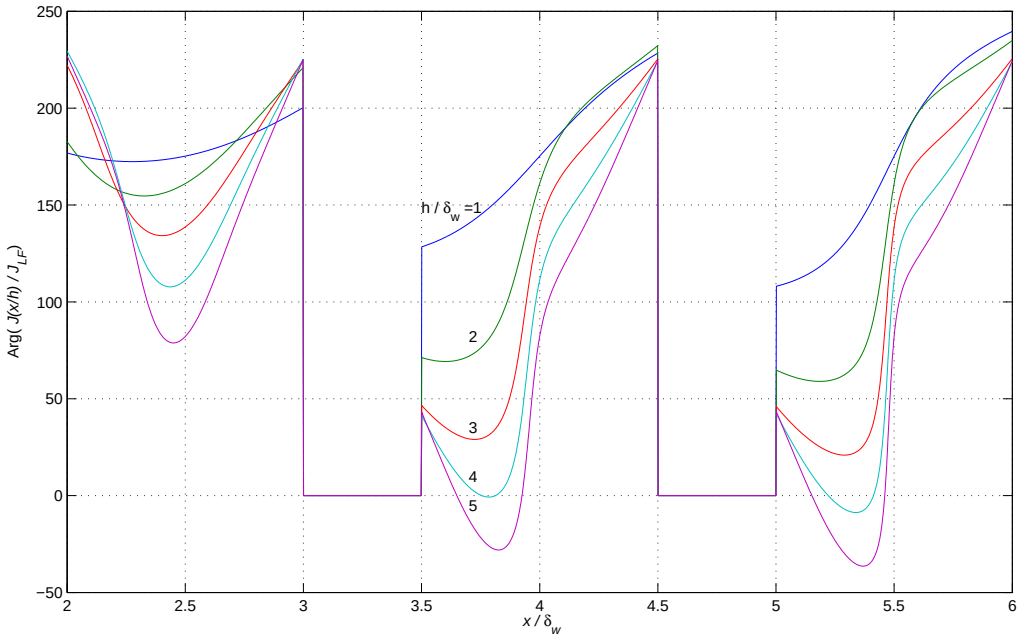

Figure 4.5: The phase of the normalized current density in the layers of an inductor with $m = 3$ layers, $\eta = 1$, and $\mu_r = 10$.

factor to correct for the breakdown of Poynting's theorem and thereby obtain the same result as would be obtained by first determining the power density and then integrating. Integrating over the inner and outer surfaces of a turn of the nth and dividing by η gives the power losses per turn:

$$P_{wn} = \frac{1}{\eta}\left[wl_T\tilde{E}(x_{n_i})\tilde{H}^*(x_{n_i}) - wl_T\tilde{E}(x_{n_o})\tilde{H}^*(x_{n_o})\right] ,$$

which is the same as (2.27) with both sides multiplied by -1 and divided by η. Again, following the deduction in Appendix E, $\tilde{H}^*(x_{n_i}) = \tilde{H}(x_{n_i})$ and $\tilde{H}^*(x_{n_o}) = \tilde{H}(x_{n_o})$. So, substituting for the fields

at the surfaces yields

$$\begin{aligned} P_{wn} &= \frac{wl_T E_{LF}\kappa\epsilon}{2\eta}\left[-H_0'(\beta_c-1)\frac{\beta_c+1-(\beta_c-1)\cosh\kappa\epsilon}{\sinh\kappa\epsilon}\right. \\ &\qquad \left.+(\beta_c+1)\frac{(\beta_c+1)\cosh\kappa\epsilon-\beta_c+1}{\sinh\kappa\epsilon}\right] \qquad (4.4) \\ &= \frac{wl_T E_{LF}\kappa\epsilon}{2\eta}\left[\frac{(\beta_c+1)^2\cosh\kappa\epsilon+(\beta_c-1)^2\cosh\kappa\epsilon-2\beta_c^2+2}{\sinh\kappa\epsilon}\right] \\ &= \frac{\rho_w l_T N_t I^2\gamma}{2\eta b}\left[\frac{(\beta_c^2+1)\cosh\kappa\epsilon-(\beta_c^2-1)}{\sinh\kappa\epsilon}\right] \\ &= \frac{\rho_w l_T N_t I^2\gamma}{2\eta b}\left[\frac{(\beta_c^2+1)\cosh\kappa\epsilon-(\beta_c^2-1)+2\cosh\kappa\epsilon-2\cosh\kappa\epsilon}{\sinh\kappa\epsilon}\right] \\ &= \frac{\rho_w l_T N_t I^2\gamma}{2\eta b}\left[\frac{(\beta_c^2-1)\cosh\kappa\epsilon-(\beta_c^2-1)}{\sinh\kappa\epsilon}+2\frac{\cosh\kappa\epsilon}{\sinh\kappa\epsilon}\right] \\ P_{wn} &= \frac{\rho_w l_T N_t I^2\gamma}{\eta b}\left[\coth\kappa\epsilon+\frac{\beta_c^2-1}{2}\tanh\frac{\kappa\epsilon}{2}\right]. \qquad (4.5) \end{aligned}$$

The total complex power can then be found by summing the complex power of all the layers:

$$P=\sum_{n=1}^{m} N_t P_{wn}\,.$$

To this end, let us consider the sum

$$\begin{aligned} \sum_{n=1}^{m}(\beta_c^2-1) &= \sum_{n=1}^{m}[m(\alpha_c-1)+2n-1]^2 \\ &= \sum_{n=1}^{m}[m^2(\alpha_c-1)^2+2mn(\alpha_c-1)-m(\alpha_c-1)+2mn(\alpha_c-1) \\ &\qquad +4n^2-2n-m(\alpha_c-1)-2n+1-1] \\ &= \sum_{n=1}^{m}\left([m^2(\alpha_c-1)+4mn-2m](\alpha_c-1)+4n^2-4n\right) \\ &= m^2[m(\alpha_c-1)-2](\alpha_c-1)+\sum_{n=1}^{m}4mn(\alpha_c-1)+4\sum_{n=1}^{m}(n^2-n) \\ &= m^2[m(\alpha_c-1)-2](\alpha_c-1)+2m^2(m+1)(\alpha_c-1)+\frac{4m(m^2-1)}{3} \\ &= m^3(\alpha_c^2-1)+\frac{4m(m^2-1)}{3}\,. \end{aligned}$$

Therefore the total complex power is

$$P=P_{LF}\kappa\epsilon\left\{\coth\kappa\epsilon+\left[\frac{m^2(\alpha_c^2-1)}{2}+\frac{2(m^2-1)}{3}\right]\tanh\frac{\kappa\epsilon}{2}\right\}, \qquad (4.6)$$

Where we have again used the dissipated power at low frequencies $P_{LF}=\rho_w l_t N_t^2 I^2 m/\eta hb$. Following

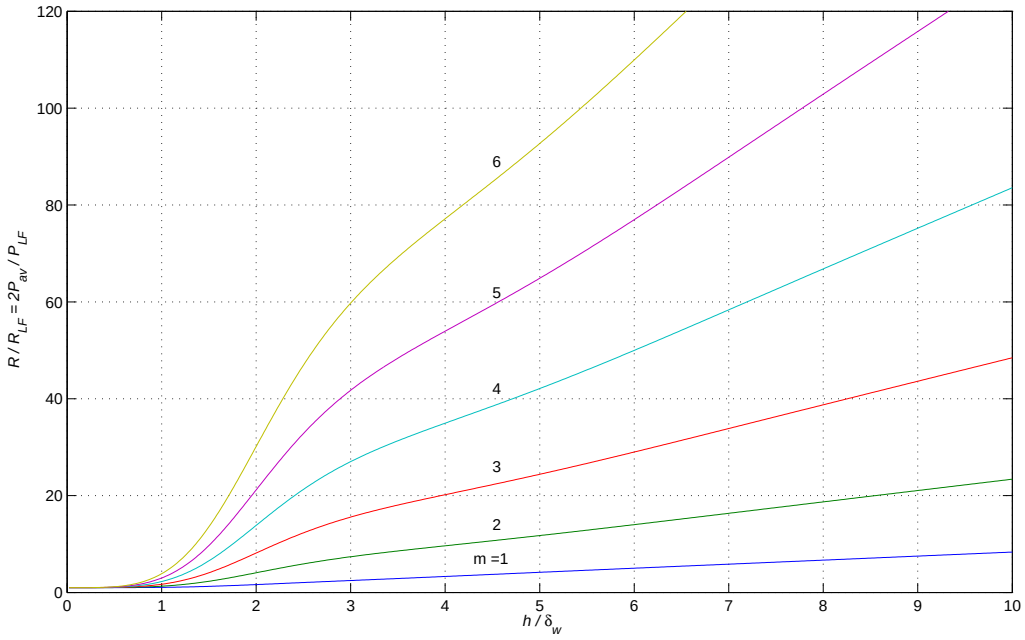

Figure 4.6: The normalized high-frequency resistance and power losses for various numbers of layers m for a device with $\eta = 1$ and $\mu_r = 10$.

the deduction in Appendix F we obtain the time-averaged power dissipated in the layers:

$$\boxed{P_{av} = \frac{1}{2}\Re\{P\} = \frac{1}{2}P_{LF}\epsilon\left\{F_1(\epsilon) + \left[\frac{m^2(\alpha_c^2 - 1)}{2} + \frac{2(m^2 - 1)}{3}\right]F_3(\epsilon)\right\}.} \tag{4.7}$$

We know from our previous analysis that the normalized frequency-dependent resistance is

$$\frac{R}{R_{LF}} = \frac{2P_{av}}{P_{LF}}. \tag{4.8}$$

A plot of the normalized resistance (and twice the normalized time-averaged power losses) is shown in Fig. 4.6 as a function of h/δ_w for various numbers of layers. Note that this plot is very similar to the power/resistance plot for an ideal core shown in Fig. 2.38, the main difference being the scale of the power losses. Notice also that all of the equations derived in this section collapse to their ideal core counterparts if we let $\mu_r \to \infty$, in which case $\alpha_c = 1$.

We may also be interested in seeing how the permeability of the core affects the power losses. Comparing (4.6) with the ideal core result (2.30), the effect of the non-ideal core is an additional term in the $\tanh(\kappa\epsilon/2)$ coefficient. One might expect this additional term to cause an increase in the power losses when the core is non-ideal but, because in this case $\alpha_c < 1$, the term takes a negative value, resulting in generally less losses for the non-ideal case. This makes sense when one considers that, the higher the permeability of the core, the more magnetic flux density will be present to

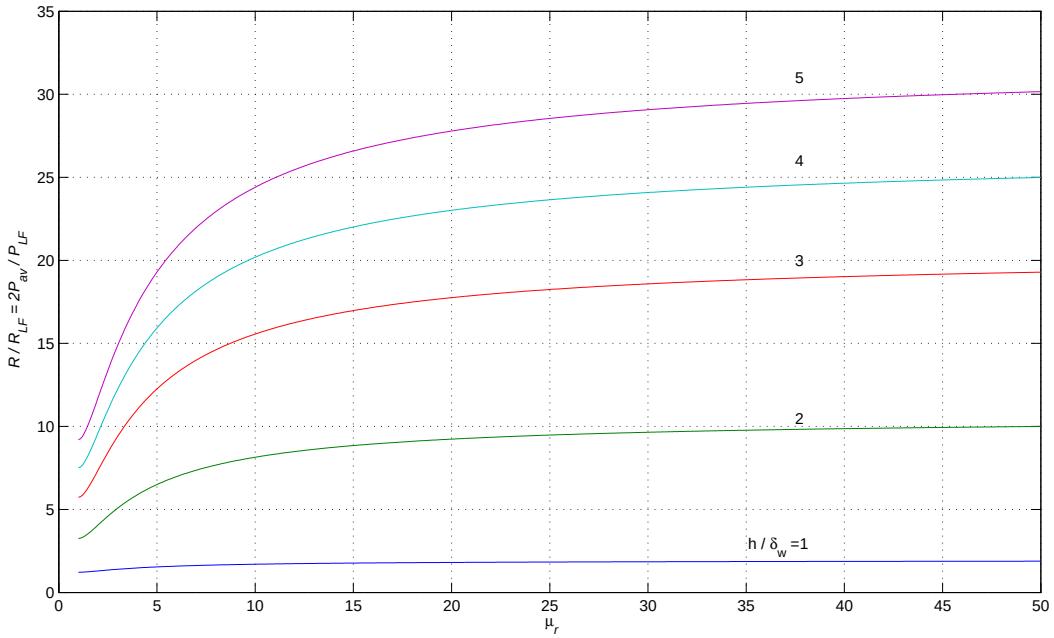

Figure 4.7: The normalized high-frequency resistance and power losses as a function of core permeability for various h/δ_w for a device with $m = 3$ and $\eta = 1$.

induce losses. This is shown in Fig. 4.7, which is a plot of the normalized ac resistance and (twice the) normalized time-averaged power dissipation for various h/δ_w and a device with $m = 3$ and $\eta = 1$. It can be observed that the losses converge to the ideal case as μ_r is increased.

4.1.2 Transformers

In the transformer case in which the core material surrounds the device, we have a situation in which the windings are in between what can be considered as two semi-infinite regions of different permeability. The application of the method of images to this problem requires an infinite number of images [Bladel 1985]. This in itself is not a problem but analysis of the 1D problem in which the windings are treated as infinitely long in y and z leads to a fundamental contradiction which cannot be resolved without a more physical 2D analysis. Such an analysis, however is outside the scope of this work and shall therefore not be treated here.

4.2 Optimum Layer Thicknesses

In the design of high-frequency magnetic devices we might like to know if there are any other ways to mitigate the losses due to the skin and proximity effects. It turns out that we can choose normalized

layer thicknesses such that the power losses are minimized, which is treated in [Perry 1979]. However, because it is more general, we shall derive the optimum layer thicknesses for a device with a non-ideal core, which to the author's knowledge has not been previously treated in the literature.

4.2.1 Inductors

We seek to thus minimize the equation for power losses in a layer. In doing this we cannot use the previously normalized form of the equations for the losses at high frequencies are always greater than the low-frequency or dc losses, thus the normalized equations have no minima, as can be observed from Fig. 2.38 and Fig. 4.7. Mathematically it is the ϵ that appears in these equations among the coefficients of the hyperbolic/trigonometric functions that renders no zeros in the derivative (thus no extrema).

So we shall begin by considering the time-averaged power losses in a layer, which is found by taking $N_t/2$ times the real part of (4.5). Applying to this the deduction in Appendix F we arrive at

$$P_{n(av)} = \frac{\rho_w l_T N_t^2 I^2}{2\sqrt{\eta}\delta_w b}\left[F_1(\epsilon) + \frac{\beta_c^2 - 1}{2}F_3(\epsilon)\right].$$

We shall find it simpler to work with this equation in a form similar to (C.5) and to that end we use the identity (C.6), which states that

$$F_3(x) = F_1(x) - 2F_2(x).$$

We thus obtain

$$P_{n(av)} = \frac{\rho_w l_T N_t^2 I^2}{2\sqrt{\eta}\delta_w b}\left[F_1(\epsilon) + \frac{\beta_c^2 - 1}{2}[F_1(\epsilon) - 2F_2(\epsilon)]\right]$$

$$P_{n(av)} = \frac{1}{2}P_{\delta_w}\sqrt{\eta}\left[\frac{\beta_c^2 + 1}{2}F_1(\epsilon) - (\beta_c^2 - 1)F_2(\epsilon)\right], \tag{4.9}$$

where

$$P_{\delta_w} \equiv \frac{\rho_w l_T N_t I^2}{\delta_w w} = \frac{\rho_w l_T N_t^2 I^2}{\eta\delta_w b}$$

is the power loss in a layer if there were a dc current flowing through only one skin depth.

A plot of renormalized (4.9) is shown in Fig. 4.8 for various layers for an inductor with $m = 5$ layers, $\mu_r = 10$ and $\eta = 1$. As can be seen, these curves have both minima and maxima and that they approach a limiting value as $\epsilon \to \infty$, i.e. as the frequency or layer thickness is increased. To determine the extrema we of course set the derivative with respect to the normalized thickness ϵ equal to zero. Taking the derivative gives

$$\frac{\partial P_{n(av)}}{\partial \epsilon} = \frac{1}{2}P_{\delta_w}\sqrt{\eta}\left[\frac{\beta_c^2 + 1}{2}\frac{dF_1}{d\epsilon} - (\beta_c^2 - 1)\frac{dF_2}{d\epsilon}\right]. \tag{4.10}$$

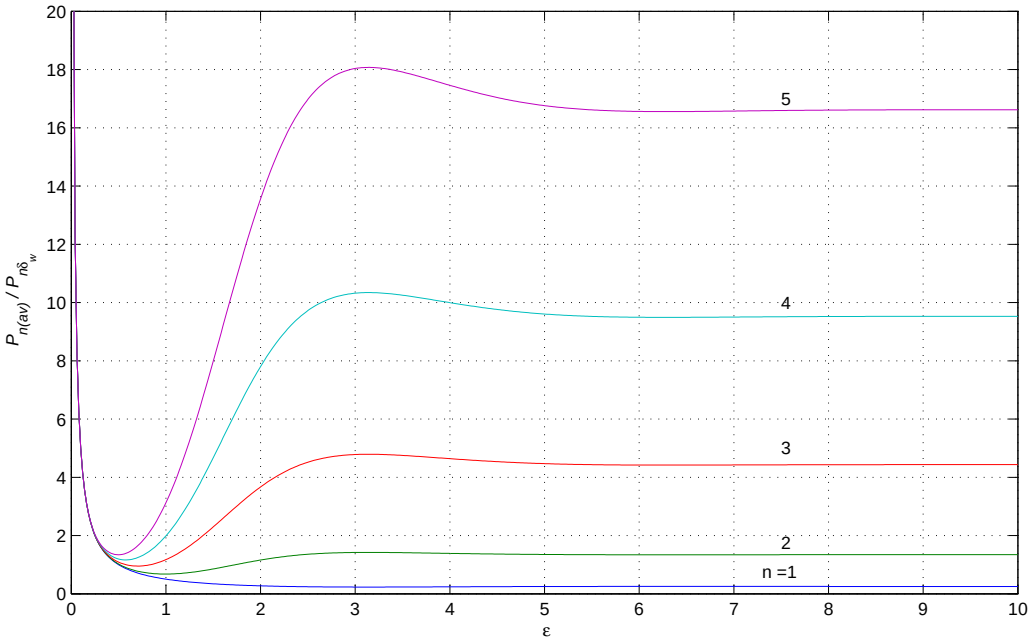

Figure 4.8: The renormalized power losses in the layers of an inductor with $m = 5$ layers, $\mu_r = 10$ and $\eta = 1$.

The derivatives of $F_1(\epsilon)$ and $F_2(\epsilon)$ are determined in Appendix H as this involves some tedious algebra. They are, from (H.6) and (H.7),

$$\frac{dF_1}{d\epsilon} = -16\frac{\cosh\epsilon\sinh\epsilon\cos\epsilon\sin\epsilon}{(\cosh 2\epsilon - \cos 2\epsilon)^2}$$

and

$$\frac{dF_2}{d\epsilon} = -4\frac{\sinh\epsilon\sin\epsilon(\cosh^2\epsilon + \cos^2\epsilon)}{(\cosh 2\epsilon - \cos 2\epsilon)^2}\,.$$

Substituting these into (4.10) yields

$$\begin{aligned}\frac{\partial P_{n(av)}}{\partial\epsilon} &= \frac{1}{2}P_{\delta_w}\sqrt{\eta}\left[-8(\beta_c^2+1)\frac{\cosh\epsilon\sinh\epsilon\cos\epsilon\sin\epsilon}{(\cosh 2\epsilon - \cos 2\epsilon)^2}\right.\\ &\qquad\left.+4(\beta_c^2-1)\frac{\sinh\epsilon\sin\epsilon(\cosh^2\epsilon+\cos^2\epsilon)}{(\cosh 2\epsilon - \cos 2\epsilon)^2}\right]\\ &= 2P_{\delta_w}\sqrt{\eta}\frac{\sinh\epsilon\sin\epsilon}{(\cosh 2\epsilon - \cos 2\epsilon)^2}\left[(\beta_c^2-1)(\cosh^2\epsilon+\cos^2\epsilon) - 2(\beta_c^2+1)\cosh\epsilon\cos\epsilon\right]\,.\end{aligned}$$

Setting this derivative to zero means that either

$$\boxed{\frac{\sinh\epsilon\sin\epsilon}{(\cosh 2\epsilon - \cos 2\epsilon)^2} = 0} \tag{4.11}$$

or

$$Z(\epsilon) \equiv (\beta_c^2 - 1)(\cosh^2\epsilon + \cos^2\epsilon) - 2(\beta_c^2 + 1)\cosh\epsilon\cos\epsilon = 0\,. \tag{4.12}$$

In looking at (4.11), one might immediately think it true at $\epsilon = 0$. However, the denominator is also zero here and, if one takes the limit, it is found that $\epsilon = 0$ is a pole, not a zero. However, this equation has analytical solutions at $\epsilon = n\pi$, where n is an integer other than zero, at which points the sine function goes to zero (and the denominator remains finite). We find, however, that such solutions correspond to maxima in the power as can be be seen from Fig. 4.8. That is except in the case of $n = 1$, in which case the single solution $\epsilon = \pi$ is the absolute minimum.

We now turn our attention to 4.12 and, in attempting to solve for ϵ, reduce it to

$$\begin{aligned}
(\beta_c^2 - 1)(\cosh^2\epsilon + \cos^2\epsilon) &= 2(\beta_c^2 + 1)\cosh\epsilon\cos\epsilon \\
\frac{\cosh^2\epsilon + \cos^2\epsilon}{\cosh\epsilon\cos\epsilon} &= 2\frac{\beta_c^2 + 1}{\beta_c^2 - 1} \\
\boxed{\frac{\cosh\epsilon}{\cos\epsilon} + \frac{\cos\epsilon}{\cosh\epsilon} = 2\frac{\beta_c^2 + 1}{\beta_c^2 - 1}\,.}
\end{aligned} \tag{4.13}$$

In the limiting case of an ideal core ($\mu_r \to \infty$), this reduces to

$$\frac{\cosh\epsilon}{\cos\epsilon} + \frac{\cos\epsilon}{\cosh\epsilon} = \frac{2n^2 - 2n + 1}{n(n-1)}\,,$$

which is the same as Perry's result (equation (19b) in [Perry 1979]).

Equation (4.12) is plotted in Fig. 4.9, in which the zero crossings are the solutions to (4.13). This is for a device with the same properties as before. The solutions of ϵ in (4.13) can only be found numerically but in the case of $n = 1$ there is no real solution except in the ideal core case, which has the analytical solution $\epsilon = \pi/2$. In the non-ideal core case the solution for $n = 1$ comes from (4.11) as discussed above. The determination of the optimized power losses in a given layer, i.e. $P_{n(av)}(\epsilon_{no})$ where ϵ_{no} denotes the solution to (4.13) for a given layer, is most simply found numerically by plugging ϵ_{no} back into (4.9).

It will be useful to be able to compare the optimized power losses with a meaningful quantity. Following Perry, we shall compare the optimized power losses with the losses when the layer thickness is much greater than the skin depth, i.e. $\epsilon \to \infty$, which approaches a definite limit as can be observed from Fig. 4.8. So, for a given layer, the time-averaged power loss in this limit is

$$P_{n(av)\infty} \equiv \lim_{\epsilon\to\infty} P_{n(av)} = \lim_{\epsilon\to\infty} \frac{1}{2} P_{\delta_w}\sqrt{\eta}\left[\frac{\beta_c^2 + 1}{2}F_1(\epsilon) - (\beta_c^2 - 1)F_2(\epsilon)\right]\,. \tag{4.14}$$

Evaluating the limit comes down to evaluating the limits for $F_1(\epsilon)$ and $F_2(\epsilon)$. These limits are found in Appendix I to be 1 and 0 for $F_1(\epsilon)$ and $F_2(\epsilon)$, respectively, thus (4.14) becomes

$$P_{n(av)\infty} = \frac{1}{2} P_{\delta_w}\sqrt{\eta}\frac{\beta_c^2 + 1}{2}\,.$$

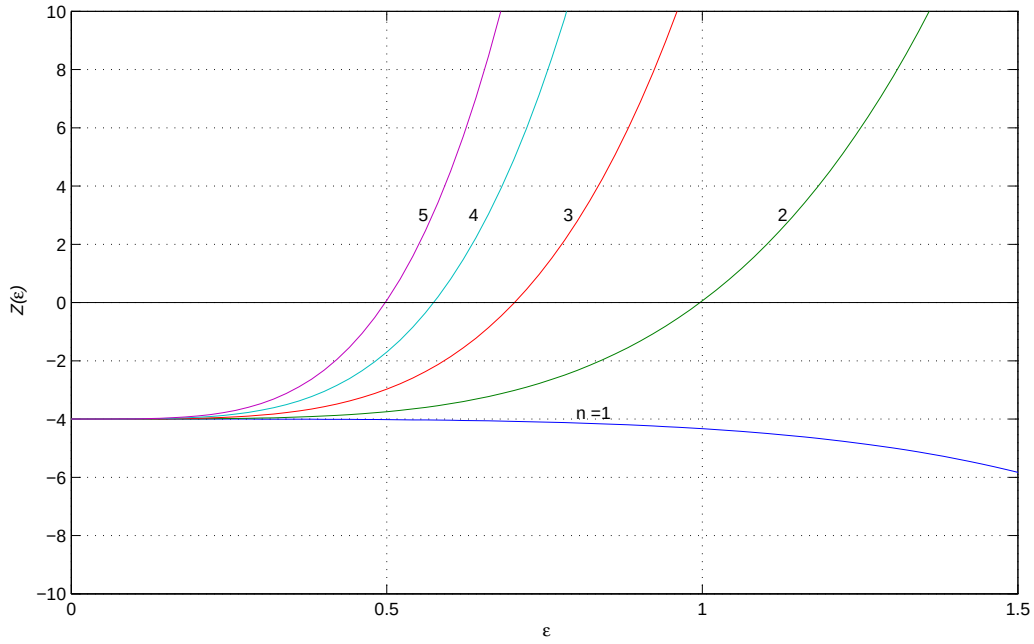

Figure 4.9: The zeros of the derivative of normalized power in a layer for an inductor with $m = 5$ layers, $\mu_r = 10$ and $\eta = 1$.

The comparative ratio is therefore

$$\boxed{\frac{P_{n(av)o}}{P_{n(av)\infty}} = F_1(\epsilon_{no}) - 2\frac{\beta_c^2 - 1}{\beta_c^2 + 1}F_2(\epsilon_{no})\,.}$$

For the device thus far considered, Table 4.2.1 shows the optimum layer thickness, normalized power losses, and the percent inverse of the ratio just developed. The percent inverse ratio quantifies the power that was saved by optimization. It is clear from this table that the power losses are significantly decreased by optimizing the layer thicknesses and that these savings increase in layers further from the core. The total power savings in the device as compared to the the case in which all the layers are much thicker than the skin depth is found by

$$1 - \frac{\sum_{n=1}^{m} P_{n(av)o}}{\sum_{n=1}^{m} P_{n(av)\infty}}\,,$$

which, for the device thus far considered, is calculated to be 86.43%.

In practical design situations it may not be possible for each layer to have a different thickness. It will therefore also be of interest how the layer thickness can be optimized such that all layers have the same thickness. To this end we begin with the equation for total time-averaged power loss in an inductor, given by (4.7):

$$P_{av} = \frac{1}{2}P_{LF}\epsilon\left\{F_1(\epsilon) + \left[\frac{m^2(\alpha_c^2 - 1)}{2} + \frac{2(m^2 - 1)}{3}\right]F_3(\epsilon)\right\}\,.$$

Table 4.1: Optimum layer thicknesses and associated power losses for an inductor with $m = 5$ layers, $\mu_r = 10$ and $\eta = 1$.

n	ϵ_{no}	$\frac{P_{n(av)o}}{P_{\delta_w}}$	$1 - \frac{P_{n(av)o}}{P_{n(av)\infty}}$
1	π	0.2315	8.14%
2	0.9966	0.6778	49.53%
3	0.7025	0.9521	78.53%
4	0.5742	1.1627	87.79%
5	0.4978	1.3404	91.93%

After renormalizing and rearranging using (C.6) as before, this becomes

$$P_{av} = \frac{m}{2} P_{\delta_w} \sqrt{\eta} \left[(\gamma_c + 1) F_1(\epsilon) - 2\gamma_c F_2(\epsilon) \right] , \tag{4.15}$$

where, for compactness in the equations we have let

$$\gamma_c \equiv \frac{m^2(\alpha_c^2 - 1)}{2} + \frac{2(m^2 - 1)}{3} = \frac{m^2(3\alpha_c^2 + 1) - 4}{6} .$$

A plot of this renormalized total power loss is shown in Fig. 4.10 for the device that we have been considering.

Taking the derivative of (4.15) with respect to ϵ gives

$$\begin{aligned} \frac{\partial P_{av}}{\partial \epsilon} &= \frac{m}{2} P_{\delta_w} \sqrt{\eta} \left[-16(\gamma_c + 1) \frac{\cosh\epsilon \sinh\epsilon \cos\epsilon \sin\epsilon}{(\cosh 2\epsilon - \cos 2\epsilon)^2} \right. \\ &\qquad \left. + 8\gamma_c \frac{\sinh\epsilon \sin\epsilon (\cosh^2\epsilon + \cos^2\epsilon)}{(\cosh 2\epsilon - \cos 2\epsilon)^2} \right] \\ &= 4m P_{\delta_w} \sqrt{\eta} \frac{\sinh\epsilon \sin\epsilon}{(\cosh 2\epsilon - \cos 2\epsilon)^2} \left[\gamma_c (\cosh^2\epsilon + \cos^2\epsilon) \right. \\ &\qquad \left. - 2(\gamma_c + 1) \cosh\epsilon \cos\epsilon \right] . \end{aligned}$$

Setting this to zero we arrive at a similar situation as before when optimizing each individual layer. From that discussion we know that the hyperbolic/trigonometric term in the front gives analytical solutions at $\epsilon = n\pi$, were n is a non-zero integer, and again these correspond to maxima in the

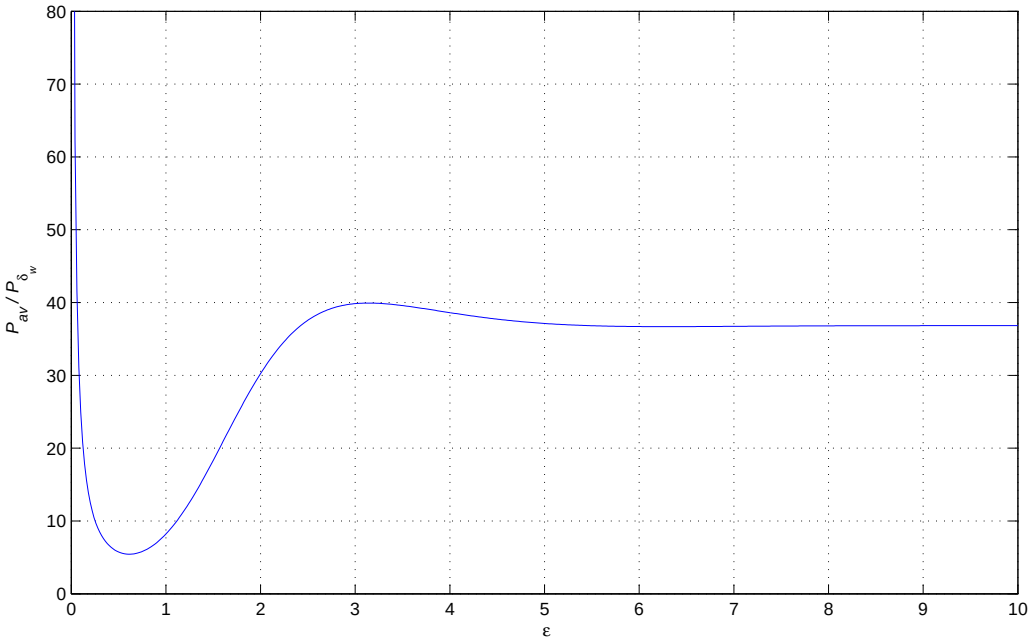

Figure 4.10: The renormalized total power losses in the layers of an inductor with $m = 5$ layers, $\mu_r = 10$ and $\eta = 1$, in which all layers are of the same thickness.

power as can be seen in Fig. 4.10. Setting the terms in brackets equal to zero reduces to

$$\gamma_c(\cosh^2\epsilon + \cos^2\epsilon) - 2(\gamma_c + 1)\cosh\epsilon\cos\epsilon = 0$$

$$\gamma_c(\cosh^2\epsilon + \cos^2\epsilon) = 2(\gamma_c + 1)\cosh\epsilon\cos\epsilon$$

$$\frac{\cosh^2\epsilon + \cos^2\epsilon}{\cosh\epsilon\cos\epsilon} = 2\frac{\gamma_c + 1}{\gamma_c}$$

$$\boxed{\frac{\cosh\epsilon}{\cos\epsilon} + \frac{\cos\epsilon}{\cosh\epsilon} = 2\frac{\gamma_c + 1}{\gamma_c}\,,}$$

which is similar to what we had before and again requires a numerical solution. It can be readily verified that in the ideal core case, this reduces to (25) in [Perry 1979]. For the device we have been considering, the absolute minimum is the numerical solution found at $\epsilon_o = 0.6140$.

If we again wish to compare this with the losses when the layer thickness is much greater than the skin depth, it should be clear from our previous discussions that

$$P_{(av)\infty} = \lim_{\epsilon\to\infty} P_{av}(\epsilon) = \frac{m}{2}P_{\delta_w}\sqrt{\eta}(\gamma_c + 1)\,.$$

Letting $P_{(av)o} = P_{av}(\epsilon_o)$, we then have our comparative ratio

$$\boxed{\frac{P_{(av)o}}{P_{(av)\infty}} = F_1(\epsilon_o) - 2\frac{\gamma_c}{\gamma_c + 1}F_2(\epsilon_o)\,.}$$

The percent inverse of this ratio, .i.e. $1 - P_{(av)o}/P_{(av)\infty}$, represents the power savings, which, in the case of our device, is computed to be 85.23%, which is only a bit less than the savings when optimizing the individual layer thicknesses.

4.2.2 Transformers

Optimum layer thicknesses can also be determined in the transformer case though, because we did not treat the more general non-ideal core in transformers, we require that $\mu_r \to \infty$. Now in the case of non-interleaved windings we can optimize each layer thickness, or the thickness in which all layers have the same thickness, in both the primary and secondary windings by considering each as the winding of an inductor. The equations deduced in the previous section therefore apply, though again such analysis is valid only for an ideal core.

In the purely interleaved case, as determined in Section 3.3, all the layers in either the primary or secondary windings are identical regarding the fields at their boundaries. It follows from this that the optimum thicknesses are the same for all of the primary or secondary layers. The total time-averaged power losses in the primary or secondary winding was found in Section 3.3, (3.8) to be

$$P_{(av)w} = \frac{1}{2} P_{LFw} \epsilon_w F_1(\epsilon_w)\,, \tag{4.16}$$

where the w subscript is 1 or 2 for either the primary or secondary winding. Furthermore, in the purely interleaved case, we observe that, because the fields on either side of a secondary layer are exactly opposite (with respect to x) of those at the boundaries of a primary layer, their optimum thicknesses will be the same, even if the primary and secondary windings have a different number of turns N_t. However the power losses will be different as factors with which we normalize the equations depend on geometry. We shall thus drop the subscript on ϵ while retaining it on these factors.

To find the losses in a single primary/secondary layer we simply divide by (4.16) by m and, after doing so and renormalizing for the reason mentioned above, we get

$$P_{1(av)w} = \frac{1}{2} P_{\delta_w w} \sqrt{\eta_w} F_1(\epsilon)\,.$$

Taking the derivative and setting it equation to zero results in

$$\frac{\partial P_{1(av)w}}{\partial \epsilon} = -2 P_{\delta_w w} \sqrt{\eta_w} \frac{\sinh 2\epsilon \sin 2\epsilon}{(\cosh 2\epsilon - \cos 2\epsilon)^2} = 0\,,$$

where we have again used the derivative of $F_1(\epsilon)$ found in Appendix H, this time using the form (H.3).

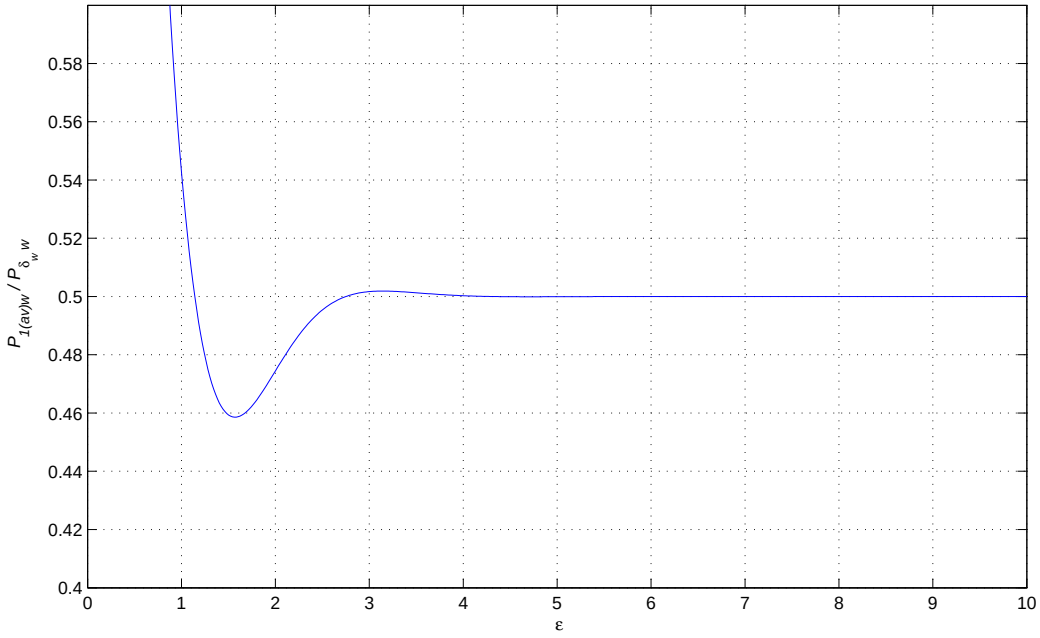

Figure 4.11: Power losses within any layer of a purely interleaved transformer normalized to the losses with current flowing through one skin depth.

Equation (4.2.2) has clear analytical solutions at $\epsilon_o = n\pi/2$, where n is any integer except zero. Zero is excluded from the solutions for the same reasons as before (the denominator also goes to zero here and it is a pole). A plot of the renormalized power losses is shown in Fig. 4.11 and, from this, it is clear that the solution $\epsilon_o = \pi/2$ is the absolute minimum. The losses at this optimum normalized thickness is found analytically as

$$\begin{aligned} P_{1(av)ow} &= \frac{1}{2} P_{\delta_w w} \sqrt{\eta_w} F_1(\epsilon_o) \\ &= \frac{1}{2} P_{\delta_w w} \sqrt{\eta_w} \frac{\sinh \pi + \sin \pi}{\cosh \pi - \cos \pi} \\ &= \frac{1}{2} P_{\delta_w w} \sqrt{\eta_w} \frac{\sinh \pi}{\cosh \pi + 1} \\ \boxed{P_{1(av)ow} &= \frac{1}{2} P_{\delta_w w} \sqrt{\eta_w} \tanh \frac{\pi}{2}\,,} \end{aligned}$$

where in the last step we have used the hyperbolic identity

$$\tanh x = \frac{\sinh 2x}{\cosh 2x + 1}\,.$$

Taking the limit as $\epsilon \to \infty$ gives us the power losses when the layer thickness is much greater than

the skin depth, which we'll use to compare as before:

$$P_{1(av)\infty w} = \lim_{\epsilon\to\infty} P_{1(av)w} = \frac{1}{2} P_{\delta_w w}\sqrt{\eta_w}\,.$$

Optimizing therefore reduces the power losses by

$$1 - \frac{P_{1(av)ow}}{P_{1(av)\infty w}} = 1 - \tanh\frac{\pi}{2} \approx 8.28\%$$

as compared to the losses at $\epsilon \to \infty$, which is not as dramatic as the inductor or non-interleaved cases, though the overall losses are greatly reduced by interleaving itself as was shown in Section 3.4. Note that this relative power saved is not dependent on the number of layers or on the geometry of the windings.

The optimized power loss for the total device is simply

$$P_{(av)o} = mP_{1(av)o1} + mP_{1(av)o2} = \frac{m}{2}\tanh\frac{\pi}{2}(\sqrt{\eta_1}P_{\delta_w 1} + \sqrt{\eta_2}P_{\delta_w 2})$$

while the total loss at $\epsilon \to \infty$ is

$$P_{(av)\infty} = mP_{1(av)\infty 1} + mP_{1(av)\infty 2} = \frac{m}{2}(\sqrt{\eta_1}P_{\delta_w 1} + \sqrt{\eta_2}P_{\delta_w 2})\,.$$

From these it is clear that the power savings for the device as a whole is the same as the savings for a single layer.

5

Conclusions

5.1 The Porosity Factor η

In Ferreira's article [Ferreira 1994] he points out that, in Dowell's work and many subsequent treatments, the porosity factor η appears in the equations as though the skin depth depends upon it. Skin depth, however can only be a function of the material properties (conductivity and permeability) and frequency and cannot depend on the geometry, of which η is a function. This theoretical inconsistency and its effects on the analysis are explored in detail by Robert in [Robert 2002]. In it he says that the fundamental problem is that Dowell performed a 1D analysis but attempted to mix in 2D effects and that its appearance in the equations cannot be justified mathematically or physically. The fact that the system is 1D means that the other dimensions simply do not exist and thus the porosity of the layers simply cannot be described in a 1D model and so trying to incorporate this into the model is unnecessary and merely empirical.

One of the effects of introducing η into the equations is that Maxwell's equations are violated, in particular Ampere's law. To illustrate how this occurs consider Fig. 5.1, which shows an Amperian loop through a single turn in a porous layer and in which the current flows into the page. Integrating around the loop results in

$$LH(x_0) - LH(x) = w \int_{x_0}^{x} J(x)dx$$
$$H(x_0) = H(x) + \frac{w}{L} \int_{x_0}^{x} J(x)dx\,.$$

This equation is valid so long as $w \leq L \leq w/\eta$. We may vary L but, in the 1D model, $H(x)$, $H(x_0)$, and the integral of $J(x)$ are constant and so the equation breaks down, thus violating Ampere's law. The only way this equation holds is if $\eta = 1$, which forces $L = w$ thereby removing 2D constants and restoring the equation to purely 1D.

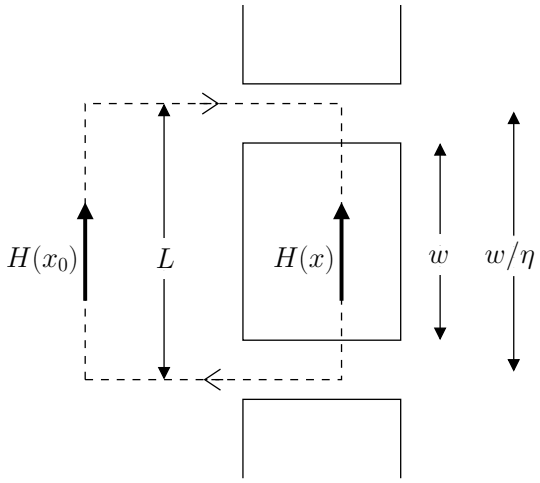

Figure 5.1: Amperian loop through a single turn of a layer.

In the previous chapter and Appendix C we derived the power losses in a layer, as well as the total power losses, in two different ways. In the chapter we used Poynting's theorem and in the appendix we integrated the power density. The results did not agree but are related by

$$\boxed{P_{Poynting} = \eta P_{density}\,.} \tag{5.1}$$

Notice that these two results are equal if and only if $\eta = 1$. Having checked and rechecked the derivations, this author can only conclude that the results are different because of the introduction of the 2D porosity factor into the 1D system. Poynting's theorem is of course derived from Maxwell's equations and, because Ampere's law is violated, Poynting's theorem does not hold. This is also the difference between our result and Dowell's. Because it does not depend on the Poynting theorem, we have used the result for power derived in Appendix C in the discussion on transformers, though in the subsequent analysis for non-ideal cores we use the Poynting theorem and divide by the porosity factor to get to the more "pure" result.

5.2 Conclusions Review

In the preceding chapters we developed the framework for describing the electromagnetic fields and losses within the windings of various types of magnetic devices. In doing so we have arrived at some conclusions regarding their operation which may also serve as principles when designing such devices. Some conclusions have already been known in the literature, while others are, to the author's knowledge, unique to this work. Such conclusions shall be reviewed and enumerated in this section.

We spent most Chapter 2 determining the electromagnetic fields, power losses, and ac resistance

of inductors while also providing the foundation for the subsequent chapters. We also analyzed the behavior of the determined fields with respect to various factors in Section 2.5. Throughout the course of this chapter we reached the following conclusions:

1. A magnetoquasistatic analysis is sufficient for typical operating frequencies and the lowest frequency at which full electrodynamic effects become appreciable was found to be 65,542 THz for copper windings.

2. As the frequency is increased, the fields penetrate into the conducting layer less and less and the current density goes to the surface, increasing there without limit. This is the familiar skin effect.

3. The magnitudes of the electromagnetic fields, current density, and power density are greater at the outer surface than the inner surface in all the layers. This is due to the proximity effect.

4. In the limit as the layer number increases, i.e. as we move from layers near the core outward

   (a) the magnetic field intensity approaches a definite form that is evenly symmetric about the center of the layer.

   (b) the electric field and current density approach definite forms that are oddly symmetric about the center of the layer.

   (c) the power density approaches a definite, evenly symmetric form.

   (d) the electromagnetic fields, current density, and power density increase indefinitely in magnitude.

5. For the electromagnetic fields and current density there are enveloped spatial waves within the layers, with a wavelength proportional to the skin depth, that propagate inward toward the center of the layer.

In Chapter 3 the results of the previous chapter are used to extend the analysis to transformers. We determined the power losses and ac resistances for various winding configurations and compared them The following conclusions were reached:

1. The current in the secondary winding is independent of the interleaving and layer thicknesses and depends only on the primary current, the numbers of layers, and the number of turns in each layer of both the primary and secondary windings. The electromagnetic fields, current density, and power losses, however, are dependent on interleaving

2. For non-interleaved windings, the primary winding is the same as an inductor without the secondary windings regarding the fields, current density, and power losses and so equations from Chapter 2 can be used to determine these. The secondary winding is also the same as an inductor except that things are reversed with respect to the spatial coordinate.

3. Interleaving the windings mitigates the losses due to the proximity effect and, in the purely interleaved case, they are completed eliminated and the total losses do not depend on the number of layers.

4. Comparing the losses in devices that have identical windings but where one is not interleaved and the other is purely interleaved, the losses ratio is a quadratic function of the number of layers and is dominated by the number of layers at higher frequencies.

In Chapter 4 we explored some other topics related to the losses in the windings, namely the effect of a non-ideal core and how the layer thicknesses can be optimized to reduce losses. Regarding the former of these we concluded the following:

1. The presence of the non-ideal deviates the electromagnetic fields and current density from the ideal core case in layers nearest to the core and especially in the first layer.

2. The power losses and ac resistance are lower for lower permeability cores but rather quickly approach the ideal core limits as the core permeability is increased.

3. The 1D analysis is insufficient for determining the effects of a non-ideal core in transformers and quickly leads to logical conflicts.

In determining the optimum layer thicknesses we came to the following conclusions in which we compare the losses/resistance to the case in which the layer thicknesses are much greater than the skin depth:

1. For an inductor or a transformer without interleaving,

   (a) the total losses and ac resistance are significantly reduced by choosing the optimal layer thickness for each layer, with the savings increasing within each layer as one moves outward from the core.

   (b) if the layer thicknesses are optimized such that all layers are of the same thickness, then the power losses and ac resistance are significantly reduced by a little less than the case in which each layer has a separate (optimized) thickness. This difference is not significant though, at least in the example we provided, though whether this holds generally is not

certain as the difference depends on numerous variables and optimized thicknesses had to be determined numerically.

2. For a transformer with interleaved windings, optimizing the layer thicknesses results in a power savings of about 8.28% regardless of the number of layers, which is not nearly as significant as the inductor/non-interleaved case, though again the losses and resistance are significantly reduced by interleaving itself. Also, in this case all the layers have the same optimum thickness by their nature.

5.3 Recommendations for Future Work

Though we have succeeded in determining a great deal about the nature of magnetic devices, we are left with a model that is far from complete even within the realm of 1-D analysis. In particular we concentrated primarily on the losses and increased ac resistance due to such losses. A complete model would also determine the inductance due to the entire winding space and core effects including losses and inductance due to the core. Though undoubtedly some work has been done in the literature on this, extending the analysis presented here to include these would be of much utility. Though of little practical utility presently due to the very high frequencies required, the radiation losses of magnetic device is another potential area of research. Perhaps this could be of interest not from the perspective of power loss but from an EMI perspective.

Another topic to explore within the scope of winding losses are the effects of an air gap on the losses and impedance. Some work has been done to this effect in [Roshen 2007], in which approximate expressions for the fringing field are derived, but how these results fit in with our analysis is unclear and, in that work, the skin effect is neglected. The fringing field effect may be difficult to incorporate into a 1-D analysis given that it cannot be described in such an analysis and care would have to be taken in this regard. One last potential area of research within the scope of 1-D analysis could be the capacitance of the windings due to their close proximity. The author is unaware of any work done on this topic but it would be necessary if a complete model of magnetic devices is to be constructed.

Throughout the course of this work we have also shed some light on the limitations of the 1-D analysis. There have been attempts to incorporate 2D effects into the 1D analysis (e.g. in [Dowell 1966] and [Kutkut 1998b]) but we have shown that, at least in Dowell's case, this can lead to violation of physical laws. Due to cylindrical symmetry the complete solution to this problem requires analysis in no more than two dimensions and, as mentioned in Section 1.2.7, there have been efforts which allow for computation of losses in a 2-D model numerically using various techniques [Albach et al. 2007; Spang and Albach 2008; Podoltsev et al. 2003]. It is this author's opinion however that a full

analytical 2-D analysis is possible, an assertion which rests on the following facts:

1. the expressions for the electromagnetic fields in and around both round and rectangular conductors are well known.

2. the principle of superposition holds.

If analytical solutions are to be found in this manner it is easy to see the rapidity with which the equations will become unwieldy. Such unwieldiness and the resulting tedium could be remedied with modern symbolic math software, though admittedly the intimate mathematical relation of the fields and current density may result in equations that presently have no analytical solution. Further difficulties are to be encountered as well in that the expressions for the electromagnetic fields of conductors assume a uniform current density, which we have shown is most definitely not the case in general. If such difficulties can be overcome, a 2-D treatment would improve the accuracy of the resulting expressions and would allow for the treatment of transformers with cores of arbitrary permeabilities.

A

Nomenclature

b	Breadth of the winding.
E	Electric field.
F	Complex HF-to-LF ratio.
$F_1(x)$	$(\sinh 2x + \sin 2x)/(\cosh 2x - \cos 2x)$
$F_2(x)$	$(\cosh x \sin x + \sinh x \cos x)/(\cosh 2x - \cos 2x)$
$F_3(x)$	$(\sinh x - \sin x)/(\cosh x + \cos x)$
h	Height of the layers.
H	Magnetic field intensity.
H_1	Magnetic field intensity between the first and second layers.
I	Magnitude of the current through the winding. It is also the phasor (which is real) because the current is the reference regarding phase.
J	Current density in the winding.
J_{LF}	Current density in the winding at low frequencies.
l_T	Mean turn length of the layers.
m	Total number of layers.
n	Layer number.
N_t	Number of turns per layer.
P	Complex power of the entire winding.
P_{av}	Average ac power dissipated in the winding.
P_{LF}	Power dissipated in the device at low frequencies.
P_n	Complex power of layer n.

P_{wn}	Complex power in a single turn of layer n.
R	Resistance of the winding at high frequencies.
R_{LF}	Resistance of the winding at low frequencies.
w	Width of a single turn.
x_{n_i}	Distance from the center of the core to the inner surface of layer n.
x_{n_o}	Distance from the center of the core to the outer surface of layer n.
Z	Impedance of the winding.
α	$\epsilon(x - x_{n_i})/h$
β	$\epsilon(x_{n_o} - x)/h$
γ	$\sqrt{j\omega\mu_0\eta/\rho_w} = \sqrt{\eta}(1+j)/\delta_w$.
δ_w	Skin depth, $\sqrt{2\rho_w/(\omega\mu_0)}$.
ϵ	$\sqrt{\eta}h/\delta_w$
ϵ_0	Permittivity of free space, 8.85×10^{-12} C^2/Nm^2.
ζ	$\alpha - \beta = \epsilon(2x - x_{n_i} - x_{n_o})/h$
η	Porosity factor, $N_t w/b$.
κ	$1 + j$.
λ	Wavelength of spatial waves.
μ_0	Permeability of free space, $4\pi \times 10^{-7}$ N/A^2.
ρ	Charge density in the conductor.
ρ_w	Resistivity of the winding conductor.
ω	Angular frequency of the current flowing through the winding.

B

Simplification of Power Density

As discussed in Section 2.6, the time-averaged power density within a layer is

$$P_d(x) = \frac{1}{2}\rho_w \tilde{J}\tilde{J}^* = \frac{1}{2}\rho_w |\tilde{J}|^2 \,.$$

Substituting (2.17) into this we get

$$P_d(x) = \frac{1}{2}\rho_w \left| J_{LF}\kappa\epsilon \frac{n\cosh\kappa\alpha - (n-1)\cosh\kappa\beta}{\sinh\kappa\epsilon} \right|^2$$
$$= \frac{1}{2}\rho_w J_{LF}^2\epsilon^2 \left| (1+j)\frac{n\cosh(\alpha+j\alpha) - (n-1)\cosh(\beta+j\beta)}{\sinh(\epsilon+j\epsilon)} \right|^2 .$$

Since, for arbitrary complex numbers z_1 and z_2, $|z_1 z_2| = |z_1||z_2|$ and, for arbitrary real or complex a and b,

$$\cosh(a+b) = \cosh a \cosh b + \sinh a \sinh b \,,$$

this becomes

$$P_d(x) = \rho_w J_{LF}^2\epsilon^2 \left| \frac{1}{\sinh\epsilon\cosh j\epsilon + \cosh\epsilon\sinh j\epsilon} \right|^2 \Big| n\cosh\alpha\cosh j\alpha$$
$$+ n\sinh\alpha\sinh j\alpha - (n-1)\cosh\beta\cosh j\beta - (n-1)\sinh\beta\sinh j\beta \Big|^2$$

$$= \rho_w J_{LF}^2\epsilon^2 \frac{1}{|\sinh\epsilon\cos\epsilon + j\cosh\epsilon\sin\epsilon|^2} \Big| n\cosh\alpha\cos\alpha$$
$$- (n-1)\cosh\beta\cos\beta + j\left(n\sinh\alpha\sin\alpha - (n-1)\sinh\beta\sin\beta\right) \Big|^2$$

$$= \rho_w J_{LF}^2 \epsilon^2 \frac{1}{(\sinh\epsilon\cos\epsilon)^2 + (\cosh\epsilon\sin\epsilon)^2} \Big[(n\cosh\alpha\cos\alpha - (n-1)\cosh\beta\cos\beta)^2 + (n\sinh\alpha\sin\alpha - (n-1)\sinh\beta\sin\beta)^2 \Big]$$

$$= \rho_w J_{LF}^2 \epsilon^2 \frac{1}{\sinh^2\epsilon\cos^2\epsilon + \cosh^2\epsilon\sin^2\epsilon} \Big[n^2\cosh^2\alpha\cos^2\alpha - 2n(n-1)\cosh\alpha\cosh\beta\cos\alpha\cos\beta + (n-1)^2\cosh^2\beta\cos^2\beta + n^2\sinh^2\alpha\sin^2\alpha - 2n(n-1)\sinh\alpha\sinh\beta\sin\alpha\sin\beta + (n-1)^2\sinh^2\beta\sin^2\beta \Big] . \tag{B.1}$$

In order to proceed we must digress for a moment and derive some general trigonometric and hyperbolic identities. We begin by utilizing the following identities:

$$\cosh^2 x = \frac{\cosh 2x + 1}{2} \qquad \sinh^2 x = \frac{\cosh 2x - 1}{2}$$
$$\cos^2 x = \frac{\cos 2x + 1}{2} \qquad \sin^2 x = \frac{1 - \cos 2x}{2} .$$

Consider then

$$\cosh^2 x\cos^2 x + \sinh^2 x\sin^2 x .$$

Substituting the identities into this we have

$$= \frac{1}{2}(\cosh 2x + 1)\frac{1}{2}(\cos 2x + 1) + \frac{1}{2}(\cosh 2x - 1)\frac{1}{2}(1 - \cos 2x)$$
$$= \frac{1}{4}(\cosh 2x + \cosh 2x\cos 2x + \cos 2x + 1 + \cosh 2x - \cosh 2x\cos 2x - 1 + \cos 2x)$$
$$\cosh^2 x\cos^2 x + \sinh^2 x\sin^2 x = \frac{\cosh 2x + \cos 2x}{2} . \tag{B.2}$$

By applying the same substitutions we come to another general identity:

$$\sinh^2 x\cos^2 x + \cosh^2 x\sin^2 x = \frac{\cosh 2x - \cos 2x}{2} . \tag{B.3}$$

In order to fully simplify (B.1) we must deduce one other general identity. We start by recalling the following for general a and b:

$$\cosh a\cosh b = \frac{\cosh(a+b) + \cosh(a-b)}{2}$$
$$\sinh a\sinh b = \frac{\cosh(a+b) - \cosh(a-b)}{2}$$
$$\cos a\cos b = \frac{\cos(a-b) + \cos(a+b)}{2}$$
$$\sin a\sin b = \frac{\cos(a-b) - \cos(a+b)}{2} .$$

For compactness we let $c = a + b$ and $d = a - b$ and, applying the identities to

$$\sinh a \sinh b \sin a \sin b + \cosh a \cosh b \cos a \cos b \,,$$

we find that

$$\begin{aligned} &= \frac{1}{2}(\cosh c - \cosh d)\frac{1}{2}(\cos d - \cos c) + \frac{1}{2}(\cosh c + \cosh d)\frac{1}{2}(\cos d + \cos c) \\ &= \frac{1}{4}(\cosh c \cos d - \cosh c \cos c - \cosh d \cos d + \cosh d \cos c + \cosh c \cos d \\ &\qquad + \cosh c \cos c + \cosh d \cos d + \cosh d \cos c) \\ &= \frac{1}{2}(\cosh c \cos d + \cosh d \cos c) \,. \end{aligned}$$

Thus

$$\begin{aligned} &\sinh a \sinh b \sin a \sin b + \cosh a \cosh b \cos a \cos b = \\ &\qquad \frac{\cosh(a+b)\cos(a-b) + \cosh(a-b)\cos(a+b)}{2} \,. \end{aligned} \tag{B.4}$$

Looking again at (B.1), we find that identities (B.2) and (B.3) simplify four of the six terms and the denominator, and identity (B.4) simplifies the remaining terms. We thus arrive at a simplified time-averaged power density:

$$\boxed{\begin{aligned} P_d(x) = \rho_w J_{LF}^2 \frac{\epsilon^2}{\cosh 2\epsilon - \cos 2\epsilon} \big[& n^2(\cosh 2\alpha + \cos 2\alpha) \\ & + (n-1)^2(\cos 2\beta + \cos 2\beta) \\ & - 2n(n-1)(\cosh\epsilon\cos\zeta + \cosh\zeta\cos\epsilon)\big] \,, \end{aligned}} \tag{B.5}$$

which is the same as equation (2.23).

C

Verification of Total Power Losses

It was mentioned in Section 2.7 that the total power losses could have been determined by integrating the power density. In this section we will verify that we get the same result doing this as we do from utilizing the Poynting theorem. The total, time-averaged power dissipated in the nth layer is reasoned to be

$$P_n = N_t w l_T \int_{x_{n_i}}^{x_{n_o}} P_d(x) dx \,.$$

Substituting the expression for power density (2.23) gives

$$\begin{aligned} P_n = N_t w l_T P_{d(LF)} \frac{2\epsilon^2}{\cosh 2\epsilon - \cos 2\epsilon} \int_{x_{n_i}}^{x_{n_o}} \big[& n^2(\cosh 2\alpha + \cos 2\alpha) \\ & + (n-1)^2(\cosh 2\beta + \cos 2\beta) \\ & - 2n(n-1)(\cosh\epsilon\cos\zeta + \cosh\zeta\cos\epsilon)\big]\, dx \,, \end{aligned} \tag{C.1}$$

where of course α, β, and ζ are functions of the position in the layer x. Noting that

$$\frac{d\alpha}{dx} = \frac{\epsilon}{h} \qquad \frac{d\beta}{dx} = -\frac{\epsilon}{h} \qquad \frac{d\zeta}{dx} = 2\frac{\epsilon}{h} \,,$$

equation (C.1) becomes

$$\begin{aligned} P_n = N_t w h l_T P_{d(LF)} \frac{2\epsilon}{\cosh 2\epsilon - \cos 2\epsilon} \Bigg[& \frac{n^2}{2}(\sinh 2\alpha + \sin 2\alpha) \\ & - \frac{(n-1)^2}{2}(\sinh 2\beta + \sin 2\beta) \\ & - n(n-1)(\cosh\epsilon\sin\zeta + \sinh\zeta\cos\epsilon)\Bigg]\Bigg|_{x_{n_i}}^{x_{n_o}} \,. \end{aligned} \tag{C.2}$$

At the surfaces we have

$$\begin{aligned} &\alpha(x_{n_i}) = 0 \qquad && \beta(x_{n_i}) = \epsilon \qquad && \zeta(x_{n_i}) = -\epsilon \\ &\alpha(x_{n_o}) = \epsilon \qquad && \beta(x_{n_o}) = 0 \qquad && \zeta(x_{n_o}) = \epsilon \,. \end{aligned}$$

Thus (C.2) evaluates to

$$\begin{aligned} P_n = N_t whl_T P_{d(LF)} \frac{2\epsilon}{\cosh 2\epsilon - \cos 2\epsilon} \Bigg[\frac{n^2}{2}(\sinh 2\epsilon + \sin 2\epsilon) \\ -n(n-1)(\cosh\epsilon \sin\epsilon + \sinh\epsilon\cos\epsilon) + \frac{(n-1)^2}{2}(\sinh 2\epsilon + \sin 2\epsilon) \\ - n(n-1)(\cosh\epsilon\sin\epsilon + \sinh\epsilon\cos\epsilon)\Bigg] \\ P_n = 2N_t whl_T P_{d(LF)}\epsilon \left[\frac{2n^2-2n+1}{2} \frac{\sinh 2\epsilon + \sin 2\epsilon}{\cosh 2\epsilon - \cos 2\epsilon} \right. \\ \left. - 2n(n-1)\frac{\cosh\epsilon\sin\epsilon + \sinh\epsilon\cos\epsilon}{\cosh 2\epsilon - \cos 2\epsilon}\right] . \end{aligned} \tag{C.3}$$

The total power is the sum of the powers in each layer:

$$\begin{aligned} P_{av} &= \sum_{n=1}^{m} P_n \\ &= \frac{\rho_w l N I^2 \epsilon}{2wh} \sum_{n=1}^{m} \left[(2n^2-2n+1)F_1(\epsilon) - 4n(n-1)F_2(\epsilon)\right] , \end{aligned} \tag{C.4}$$

where we have substituted in for $P_{d(LF)}$ and defined the functions

$$\begin{aligned} F_1(x) &\equiv \frac{\sinh 2x + \sin 2x}{\cosh 2x - \cos 2x} \\ F_2(x) &\equiv \frac{\cosh x \sin x + \sinh x \cos x}{\cosh 2x - \cos 2x} . \end{aligned}$$

Recalling again that

$$\sum_{n=1}^{m} n = \frac{m(m+1)}{2}$$

and

$$\sum_{n=1}^{m} n^2 = \frac{m(m+1)(2m+1)}{6} ,$$

equation (C.4) evaluates to

$$\begin{aligned} P_{av} = \frac{\rho_w l N I^2 \epsilon}{2wh} \Bigg[\left(\frac{2m(m+1)(2m+1)}{6} - \frac{2m(m+1)}{2} + m \right) F_1(\epsilon) \\ - \left(\frac{4m(m+1)(2m+1)}{6} - \frac{4m(m+1)}{2} \right) F_2(\epsilon) \Bigg] \\ = \frac{\rho_w l N I^2 \epsilon}{2wh} \left[\frac{2m^2+3m+1-3m-3+3}{3} F_1(\epsilon) - \frac{4m^2+6m+2-6m-6}{3} F_2(\epsilon) \right] \\ \boxed{P_{av} = \frac{1}{2} P_{LF} \epsilon \left[\frac{2m^2+1}{3} F_1(\epsilon) - \frac{4(m^2-1)}{3} F_2(\epsilon) \right] .} \end{aligned} \tag{C.5}$$

This equation is the expression for total power losses that appears in [Perry 1979] and [Vandelac and Ziogas 1988]. This is clearly different from the expression for total time-averaged power (2.33)

derived in Section 2.7 but they are found to be equal if we utilize the hyperbolic/trigonometric identity

$$F_2(x) = \frac{\cosh x \sin x + \sinh x \cos x}{\cosh 2x - \cos 2x} = \frac{1}{2}\left[\frac{\sinh 2x + \sin 2x}{\cosh 2x - \cos 2x} - \frac{\sinh x - \sin x}{\cosh x + \cos x}\right], \tag{C.6}$$

which is given in Appendix B of [Ferreira 1994]. We shall let the function $F_3(x)$ be

$$F_3(x) \equiv \frac{\sinh x - \sin x}{\cosh x + \cos x}$$

and (C.5) becomes

$$\begin{aligned} P_{av} &= \frac{1}{2} P_{LF} \epsilon \left[\frac{2m^2+1}{3} F_1(\epsilon) - \frac{4(m^2-1)}{6}(F_1(\epsilon) - F_3(\epsilon))\right] \\ &= \frac{1}{2} P_{LF} \epsilon \left[\frac{4m^2 + 2 - 4m^2 + 4}{6} F_1(\epsilon) + \frac{2(m^2-1)}{3} F_3(\epsilon)\right] \\ &\boxed{P_{av} = \frac{1}{2} P_{LF} \epsilon \left[F_1(\epsilon) + \frac{2(m^2-1)}{3} F_3(\epsilon)\right].} \end{aligned} \tag{C.7}$$

This is close but not equivalent to (2.33) derived using the Poytning theorem in Section 2.7. This important difference is discussed in Section 5.1. We have, however, demonstrated how the results of Perry and Vandelec/Ziogas are the same as Dowell's: the former report in the form of (C.5) while the latter reports (C.7).

D

Complex Power

In Section 2.7, the complex power was used to determine the impedance of a multilayer inductor. It is the purpose of this section to elucidate the meaning of complex power and, in doing so, to show why we are justified in using it to obtain the impedance. Let us begin by considering an ac current flowing through a circuit or component and the voltage across it, given by

$$i(t) = I\cos(\omega t + \phi_I) \qquad\qquad v(t) = V\cos(\omega t + \phi_V)\,,$$

respectively. The circuit or component has a general impedance Z (i.e. some combination of resistive and reactive components) that results in a phase difference of $\phi_Z = \phi_V - \phi_I$ between the voltage and the current. Consider then the following:

$$\begin{aligned} v(t) = V\cos(\omega t + \phi_V) &= \frac{1}{2}V[e^{j\omega t}e^{j\phi_V} + e^{-j\omega t}e^{-j\phi_V}] \\ &= \frac{1}{2}V[e^{j\omega t}e^{j\phi_V}e^{j\phi_I}e^{-j\phi_I} + e^{-j\omega t}e^{-j\phi_V}e^{-j\phi_I}e^{j\phi_I}] \\ &= \frac{1}{2}V[e^{j(\phi_V-\phi_I)}e^{j(\omega t+\phi_I)} + e^{-j(\phi_V-\phi_I)}e^{-j(\omega t+\phi_I)}]\,. \end{aligned}$$

Here we let

$$\tau = \omega t + \phi_I \qquad\qquad \phi_Z = \phi_V - \phi_I$$

so that the following can be written more compactly. We then have

$$\begin{aligned}
v(t) &= \frac{1}{2}V[e^{j\phi_Z}e^{j\tau} + e^{-j\phi_Z}e^{-j\tau}] \\
&= \frac{1}{2}V[(\cos\phi_Z + j\sin\phi_Z)(\cos\tau + j\sin\tau) + (\cos\phi_Z - j\sin\phi_Z)(\cos\tau - j\sin\tau)] \\
&= \frac{1}{2}V[\cos\phi_Z\cos\tau + j\cos\phi_Z\sin\tau + j\sin\phi_Z\cos\tau - \sin\phi_Z\sin\tau \\
&\quad + \cos\phi_Z\cos\tau - j\cos\phi_Z\sin\tau - j\sin\phi_Z\cos\tau - \sin\phi_Z\sin\tau] \\
&= \frac{1}{2}V[2\cos\phi_Z\cos\tau - 2\sin\phi_Z\sin\tau] \\
&= V[\cos\phi_Z\cos\tau - \sin\phi_Z\sin\tau]\,.
\end{aligned}$$

So we can express the voltage as

$$v(t) = v_R(t) + v_X(t)\,, \tag{D.1}$$

where

$$v_R(t) = V\cos(\phi_V - \phi_I)\cos(\omega t + \phi_I)$$

and

$$v_X(t) = -V\sin(\phi_V - \phi_I)\sin(\omega t + \phi_I)\,.$$

The voltage is therefore expressed as the sum of a component that is in phase with the current and a component that is ninety degrees out of phase with it. The former is responsible for the resistive component of the power while the latter is responsible for the reactive component. The instantaneous resistive power is therefore

$$\begin{aligned}
p_R(t) &= v_R(t)i(t) = V\cos(\phi_V - \phi_I)\cos(\omega t + \phi_I)I\cos(\omega t + \phi_I) \\
&= VI\cos(\phi_V - \phi_I)\cos^2(\omega t + \phi_I) \\
p_R(t) &= \frac{1}{2}VI\cos(\phi_V - \phi_I)[1 + \cos(2\omega t + 2\phi_I)]\,,
\end{aligned} \tag{D.2}$$

and the instantaneous reactive power is

$$\begin{aligned}
p_X(t) &= v_X(t)i(t) = -V\sin(\phi_V - \phi_I)\sin(\omega t + \phi_I)I\cos(\omega t + \phi_I) \\
p_X(t) &= -\frac{1}{2}VI\sin(\phi_V - \phi_I)\sin(2\omega t + 2\phi_I)\,.
\end{aligned} \tag{D.3}$$

The total instantaneous power is

$$\begin{aligned}
p(t) &= p_R(t) + p_X(t) = v(t)i(t) \\
&= V\cos(\omega t + \phi_V)I\cos(\omega t + \phi_I) \\
p(t) &= \frac{1}{2}VI[\cos(\phi_V - \phi_I) + \cos(2\omega t + \phi_V + \phi_I)]\,.
\end{aligned} \tag{D.4}$$

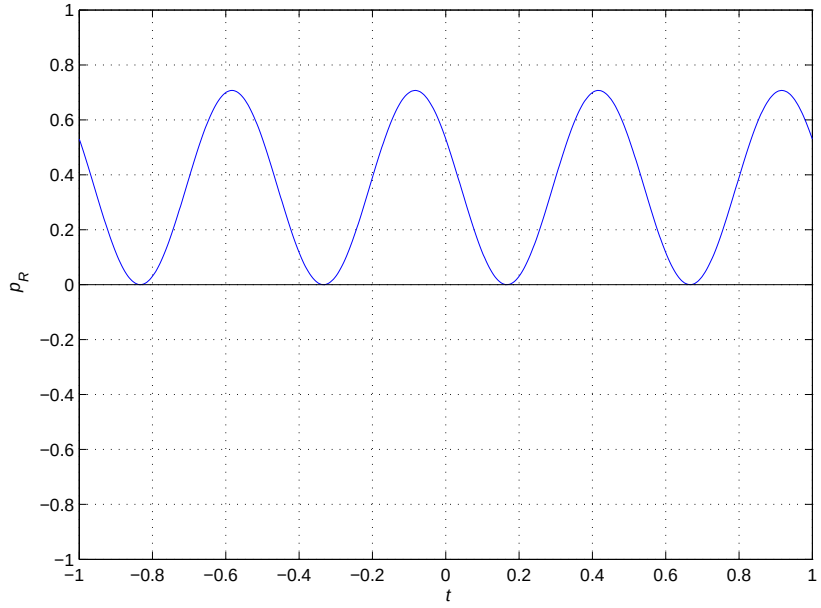

Figure D.1: The instantaneous pure resistive power for $\omega = 2\pi$, $I = 1$ A, $\phi_I = \frac{\pi}{6}$, $V = 1$ V, and $\phi_V = \frac{5\pi}{12}$.

That (D.4) is equal to $p_R(t)+p_X(t)$ is not shown explicitly here, but it follows necessarily from (D.1). Plots of (D.2), (D.3), and (D.4) are shown in Fig. D.1, Fig. D.2, and Fig. D.3, respectively, for an arbitrarily chosen frequency, peak voltage, peak current, and phases. Note that the instantaneous resistive power is always positive and the average reactive power is zero. This is consistent with the notion of resistive and reactive components.

The amount of energy stored in the fields changes periodically with time. The maximum amount of this energy, i.e. the energy stored at the moment when the system stops storing energy and starts extracting it, can be determined by integrating the reactive power over a half-cycle. To make things simpler, we can ignore the phase shift (and the negative sign, which is just an additional phase shift) and define

$$p'_X(t) = \frac{1}{2} VI \sin(\phi_V - \phi_I) \sin(2\omega t)\,.$$

The maximum energy stored in the fields is then

$$W = \int_0^{\frac{T}{2}} p'_X(t) dt\,,$$

where T is the period. In our case, the angular frequency ω' is 2ω, which makes the period

$$T = \frac{1}{f} = \frac{2\pi}{\omega'} = \frac{\pi}{\omega}\,.$$

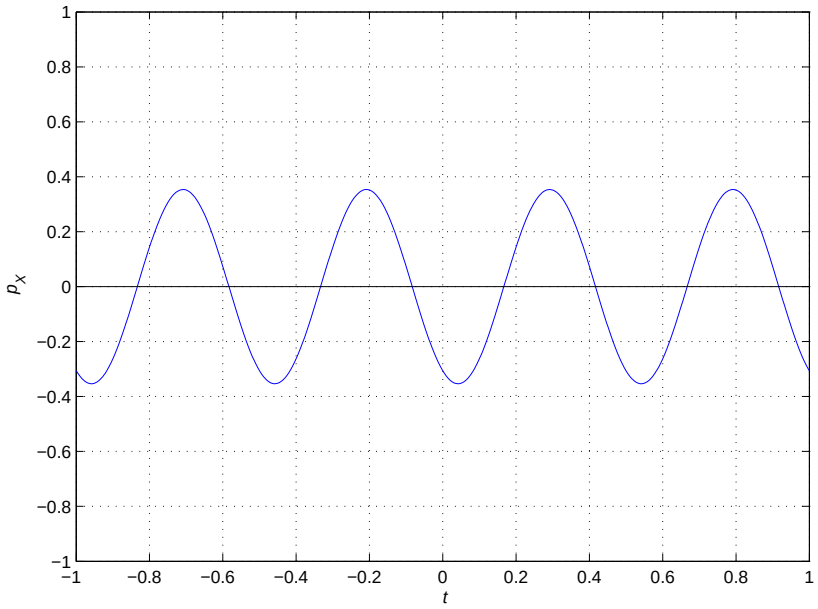

Figure D.2: The instantaneous pure reactive power for $\omega = 2\pi$, $I = 1$ A, $\phi_I = \frac{\pi}{6}$, $V = 1$ V, and $\phi_V = \frac{5\pi}{12}$.

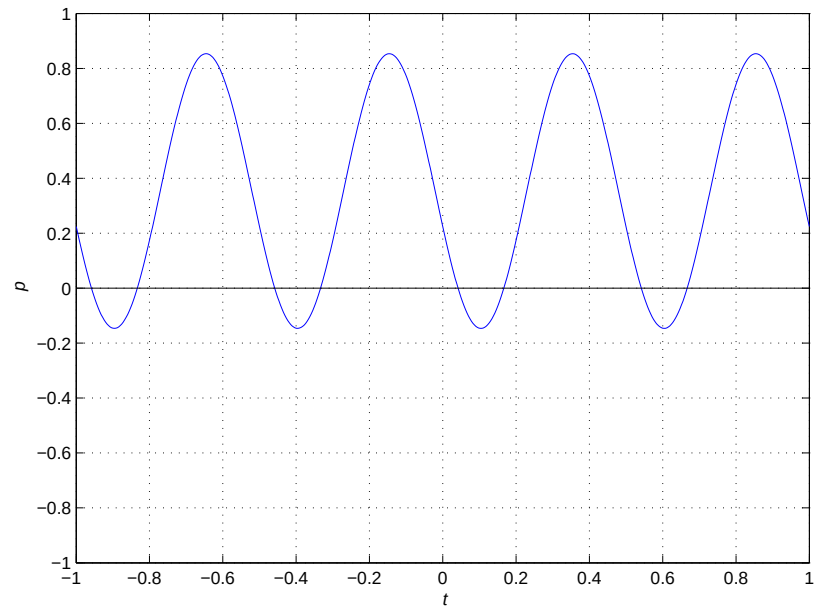

Figure D.3: The instantaneous total power for $\omega = 2\pi$, $I = 1$ A, $\phi_I = \frac{\pi}{6}$, $V = 1$ V, and $\phi_V = \frac{5\pi}{12}$.

The maximum energy stored in the fields thus becomes

$$\begin{aligned} W &= \int_0^{\frac{\pi}{2\omega}} \frac{1}{2} VI \sin(\phi_V - \phi_I) \sin(2\omega t) dt \\ &= \frac{1}{2} VI \sin(\phi_V - \phi_I) \int_0^{\frac{\pi}{2\omega}} \sin(2\omega t) dt \\ &= \frac{1}{2} VI \sin(\phi_V - \phi_I) \left(\frac{-\cos 2\omega t}{2\omega} \right) \Bigg|_0^{\frac{\pi}{2\omega}} \\ W &= \frac{VI \sin(\phi_V - \phi_I)}{2\omega} \,. \end{aligned}$$

This amount of energy is stored in the fields and then returned each cycle, or twice each cycle if referring to the frequency of the voltage and current.

We now focus our attention on the complex power that arises from the phasor representation of the voltage and current. If the voltage and current phasors are

$$\tilde{V} = V e^{j\phi_V} \qquad\qquad \tilde{I} = I e^{j\phi_I} \,,$$

then the complex power is

$$\begin{aligned} P &= \tilde{V}\tilde{I}^* = V e^{j\phi_V} I e^{-j\phi_I} \\ &= VI e^{j(\phi_V - \phi_I)} \\ &= VI[\cos(\phi_V - \phi_I) + j \sin(\phi_V - \phi_I)] \\ P &= VI \cos(\phi_V - \phi_I) + jVI \sin(\phi_V - \phi_I) \,. \end{aligned}$$

It is clear from (D.2) that the real part of the complex power is twice the average of the instantaneous resistive power. This is also twice the average of the total instantaneous power, as is obvious from (D.4). Similarly, the imaginary part of the complex power is twice the maximum, or peak, of the instantaneous reactive power, which can be seen from an examination of (D.3).

Fig. D.4 shows the voltage and current phasors as vectors on the complex plane. Another interpretation of the complex power is that the real part indicates the degree to which the vectors have the same (or opposite) direction (the resistive component). This is the dot product of the two vectors. The imaginary part of the complex power represents the degree to which the vectors are orthogonal (the reactive component) and is equal to the magnitude of the cross product of the two vectors.

An identical analysis can be done for the electric and magnetic fields and their phasors used in Poynting theorem. In this case, the Poynting vector, which is the product (instantaneous or phasor) of the electric and magnetic fields, does not represent the power but rather the power surface density, i.e. the rate of energy crossing a surface per unit area. The real and imaginary parts of the complex

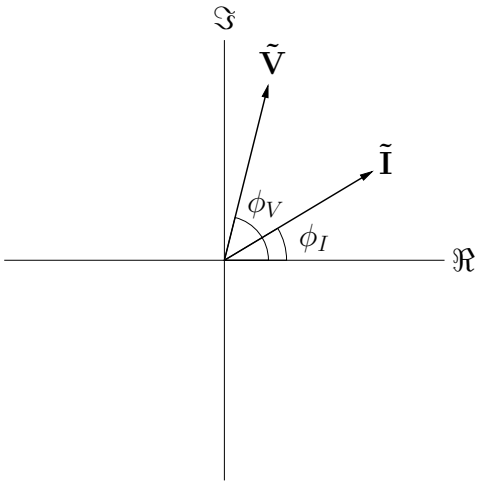

Figure D.4: Current and voltage phasors as vectors for $\phi_I = \frac{\pi}{6}$, $\phi_V = \frac{5\pi}{12}$, and $\phi_Z = \phi_V - \phi_I = \frac{\pi}{4}$.

power surface density correspond to the instantaneous power surface density in the same way that the complex power corresponds to the instantaneous power. When the complex power surface density is integrated over a surface, as is done in the Poynting theorem, the result is the complex power, and it is this fact which allows us to determine the impedance from it using phasors.

E

Verification of Magnetic Field Intensity Conjugate Equivalence at the Surfaces

In Section 2.7 we said that the magnetic field intensity at the inner and outer surfaces is equal to its conjugate there, i.e. $\tilde{H}^*(x_{n_i}) = \tilde{H}(x_{n_i})$ and $\tilde{H}^*(x_{n_o}) = \tilde{H}(x_{n_o})$. It is the purpose of this section to show this. From (2.16) we know that the magnetic field intensity within the nth layer is

$$\tilde{H}(x) = -H_1 \frac{n \sinh\left[\gamma(x - x_{n_i})\right] + (n-1)\sinh\left[\gamma(x_{n_o} - x)\right]}{\sinh \gamma h}\,.$$

What then is the conjugate of this $\tilde{H}(x)^*$? First we note that, for general complex numbers z_1 and z_2, the following are true:

$$\begin{aligned}
\overline{z_1 + z_2} &= \overline{z_1} + \overline{z_2} \\
\overline{z_1 z_2} &= \overline{z_1}\ \overline{z_2} \\
\overline{\left(\frac{z_1}{z_2}\right)} &= \frac{\overline{z_1}}{\overline{z_2}}\,,
\end{aligned}$$

where we shall now use the overline to indicate complex conjugate in order to make the following easier to read. Thus we can say that

$$\overline{\tilde{H}(x)} = -H_1 \frac{n\overline{\sinh\left[\gamma(x - x_{n_i})\right]} + (n-1)\overline{\sinh\left[\gamma(x_{n_o} - x)\right]}}{\overline{\sinh \gamma h}}\,. \tag{E.1}$$

Let us then investigate further the conjugate of the sinh function. Consider then, for general real a and b,

$$\begin{aligned}
\overline{\sinh(a+jb)} &= \overline{\sinh a\cosh jb + \cosh a\sinh jb} \\
&= \overline{\sinh a\cos b + j\cosh a\sin b} \\
&= \sinh a\cos b - j\cosh a\sin b \\
&= \sinh a\cos(-b) + j\cosh a\sin(-b) \\
&= \sinh a\cosh(-jb) + \sinh a\sinh(-jb) \\
&= \sinh(a-jb)\,.
\end{aligned}$$

Thus we can say that, for a general complex number z,

$$\overline{\sinh z} = \sinh\overline{z}\,.$$

Applying this fact and the previously mentioned complex conjugate properties to (E.1) yields

$$\tilde{H}^*(x) = -H_1\frac{n\sinh[\gamma^*(x-x_{n_i})] + (n-1)\sinh[\gamma^*(x_{n_o}-x)]}{\sinh\gamma^* h}\,.$$

Plugging in the value of x at the surfaces gives

$$\boxed{\begin{aligned}\tilde{H}^*(x_{n_i}) &= -(n-1)H_1 \\ \tilde{H}^*(x_{n_o}) &= -nH_1\,,\end{aligned}}$$

which are exactly the boundary conditions established in Section 2.3 from which the specific solution followed.

F

Real and Imaginary Parts of F

The complex HF-to-LF ratio factor is

$$F = \eta\gamma h \left[\coth\gamma h + \frac{2(m^2-1)}{3}\tanh\frac{\gamma h}{2}\right] . \tag{F.1}$$

It is complex because $\gamma = \sqrt{\eta}(1+j)/\delta_w$ is complex, and expressions for real and imaginary parts of (F.1) shall be determined in the following discussion. If z is a general complex number, let us denote its real and imaginary parts by z' and z'', respectively, in lieu of the more cumbersome $\Re\{z\}$ and $\Im\{z\}$. We let

$$M = \coth\gamma h \qquad\qquad D = \tanh\frac{\gamma h}{2}$$

and

$$\gamma h = \frac{\sqrt{\eta}h(1+j)}{\delta_w} = \epsilon + \epsilon j\,,$$

where

$$\epsilon = \sqrt{\eta}\frac{h}{\delta_w}\,.$$

(F.1) can then be expressed as

$$\begin{aligned} F &= \eta\epsilon(1+j)\left[M + \frac{2(m^2-1)}{3}D\right] \\ &= \eta\epsilon(1+j)\left[M' + jM'' + \frac{2(m^2-1)}{3}(D' + jD'')\right] \\ &= \eta\epsilon\left[M' + jM'' + jM' - M'' + \frac{2(m^2-1)}{3}(D' + jD'' + jD' - D'')\right] . \end{aligned}$$

From this we have

$$\Re\{F\} = F' = \eta\epsilon\left[M' - M'' + \frac{2(m^2-1)}{3}(D' - D'')\right] \tag{F.2}$$

$$\Im\{F\} = F'' = \eta\epsilon\left[M' + M'' + \frac{2(m^2-1)}{3}(D' + D'')\right] . \tag{F.3}$$

All that remains then is to determine M', M'', D', and D'', or, equivalently, the real and imaginary parts of the coth and tanh functions. To this end, let us begin by determining the components of the more general complex function $\coth z$, where

$$z = \alpha + \beta j$$

is a general complex number. Now,

$$\begin{aligned}
\coth z = \frac{\cosh z}{\sinh z} &= \frac{e^z + e^{-z}}{e^z - e^{-z}} = \frac{e^\alpha e^{j\beta} + e^{-\alpha} e^{-j\beta}}{e^\alpha e^{j\beta} - e^{-\alpha} e^{-j\beta}} \\
&= \frac{(e^\alpha e^{j\beta} + e^{-\alpha} e^{-j\beta})(e^\alpha e^{-j\beta} - e^{-\alpha} e^{j\beta})}{(e^\alpha e^{j\beta} - e^{-\alpha} e^{-j\beta})(e^\alpha e^{-j\beta} - e^{-\alpha} e^{j\beta})} \\
&= \frac{e^{2\alpha} - e^{j2\beta} + e^{-j2\beta} - e^{-2\alpha}}{e^{2\alpha} - e^{j2\beta} - e^{-j2\beta} + e^{-2\alpha}} \,. \qquad \text{(F.4)}
\end{aligned}$$

Recalling that

$$\cosh x = \frac{e^x + e^{-x}}{2} \qquad \sinh x = \frac{e^x - e^{-x}}{2}$$
$$\cos x = \frac{e^{jx} + e^{-jx}}{2} \qquad \sin x = \frac{e^{jx} - e^{-jx}}{j2} \,,$$

(F.4) becomes

$$\coth z = \frac{\sinh 2\alpha - j \sin 2\beta}{\cosh 2\alpha - \cos 2\beta} \,. \qquad \text{(F.5)}$$

Next we shall find the real and imaginary parts of $\tanh z$. We could derive this from the previous result by finding the real and imaginary parts of the reciprocal of (F.5). However, it is less tedious to derive it directly, using the same approach as before:

$$\begin{aligned}
\tanh z = \frac{\sinh z}{\cosh z} &= \frac{e^z - e^{-z}}{e^z + e^{-z}} = \frac{e^\alpha e^{j\beta} - e^{-\alpha} e^{-j\beta}}{e^\alpha e^{j\beta} + e^{-\alpha} e^{-j\beta}} \\
&= \frac{(e^\alpha e^{j\beta} - e^{-\alpha} e^{-j\beta})(e^\alpha e^{-j\beta} + e^{-\alpha} e^{j\beta})}{(e^\alpha e^{j\beta} + e^{-\alpha} e^{-j\beta})(e^\alpha e^{-j\beta} + e^{-\alpha} e^{j\beta})} \\
&= \frac{e^{2\alpha} + e^{j2\beta} - e^{-j2\beta} - e^{-2\alpha}}{e^{2\alpha} + e^{j2\beta} + e^{-j2\beta} + e^{-2\alpha}} \\
\tanh z &= \frac{\sinh 2\alpha + j \sin 2\beta}{\cosh 2\alpha + \cos 2\beta} \,. \qquad \text{(F.6)}
\end{aligned}$$

In our case, for the coth term,

$$\alpha = \beta = \epsilon \,,$$

so (F.5) becomes

$$\coth \gamma h = \frac{\sinh 2\epsilon - j \sin 2\epsilon}{\cosh 2\epsilon - \cos 2\epsilon} \,.$$

For the tanh term,

$$\alpha = \beta = \frac{\epsilon}{2}\,,$$

so (F.6) becomes

$$\tanh\frac{\gamma h}{2} = \frac{\sinh\epsilon + j\sin\epsilon}{\cosh\epsilon + \cos\epsilon}\,.$$

To put these results in our terms from before,

$$M' = \frac{\sinh 2\epsilon}{\cosh 2\epsilon - \cos 2\epsilon} \qquad M'' = \frac{-\sin 2\epsilon}{\cosh 2\epsilon - \cos 2\epsilon}$$
$$D' = \frac{\sinh\epsilon}{\cosh\epsilon + \cos\epsilon} \qquad D'' = \frac{\sin\epsilon}{\cosh\epsilon + \cos\epsilon}\,.$$

Applying these to (F.2) and (F.3), we have our desired result

$$\boxed{\begin{aligned}\Re\{F\} = F' &= \eta\epsilon\left[\frac{\sinh 2\epsilon + \sin 2\epsilon}{\cosh 2\epsilon - \cos 2\epsilon} + \frac{2(m^2-1)}{3}\frac{\sinh\epsilon - \sin\epsilon}{\cosh\epsilon + \cos\epsilon}\right]\\ \Im\{F\} = F'' &= \eta\epsilon\left[\frac{\sinh 2\epsilon - \sin 2\epsilon}{\cosh 2\epsilon - \cos 2\epsilon} + \frac{2(m^2-1)}{3}\frac{\sinh\epsilon + \sin\epsilon}{\cosh\epsilon + \cos\epsilon}\right]\,.\end{aligned}}$$

G

Method of Images

In Section 4.1 the method of images is used to determine the effect of a non-ideal core on the analysis. In this section we shall explore how this method comes about and in so doing why its use is justified. Consider the problem of determining the magnetic field around a dc infinite line current I flowing in the y direction and is placed at $(x, z) = (0, h)$, near the boundary of two semi-infinite regions of different permeability, the boundary being the infinite xy plane at $z = 0$. This is shown in Fig. G.1. The presence of the region of different permeability affects the magnetic field in a nontrivial way and prohibits the use of simple Amperian loops to determine the magnetic field, since the field can no longer be assumed to simply encircle the line current symmetrically.

The validity of the method of images rests on the uniqueness theorem, which states that, in some region of interest, any solution that satisfies the governing equation(s) as well as the boundary conditions is the unique and correct solution. In our case the governing equation is Laplace's equation for the magnetic scalar potential or, for the fields themselves, Gauss's law for magnetism and Ampere's law. The boundary conditions are:

1. The normal component of the magnetic flux density is continuous across the magnetic interface.
2. The tangential component of the magnetic field intensity is continuous across the magnetic interface.

Our approach to solving this problem follows that found in [Jackson 1962], though ours is a magnetostatic problem rather than an electrostatic one. We can determine the magnetic field intensity in the μ_1 region, $\mathbf{H_1}$, by placing an image source I' at the location of the reflection of the original source over the boundary and considering the entire space as a region of permeability μ_1, as shown in Fig. G.2. The solution to this problem, which is our desired solution, is only valid in the original μ_1 region, i.e. for $z \geq 0$, which we shall henceforth refer to as region one. Analogously, the magnetic field intensity in the μ_2 region, $\mathbf{H_2}$, is determined by replacing the original source with an

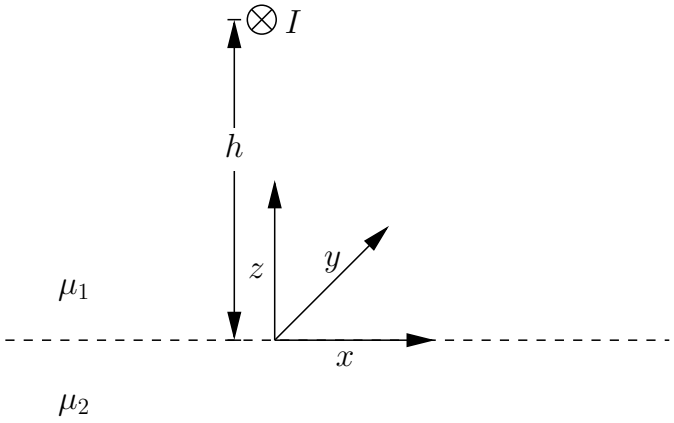

Figure G.1: The original problem, a line current near a magnetic boundary.

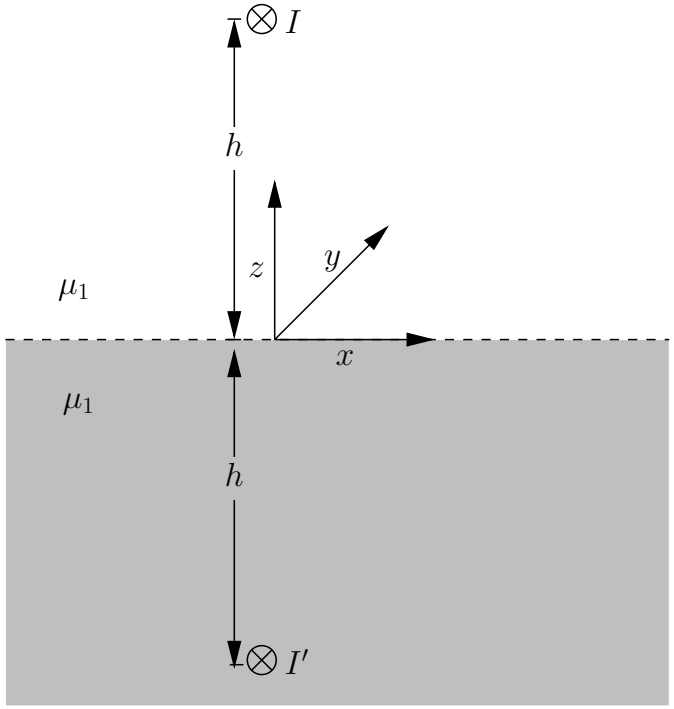

Figure G.2: Solution for the $z \geq 0$ region. The gray region indicates where the solution is not valid.

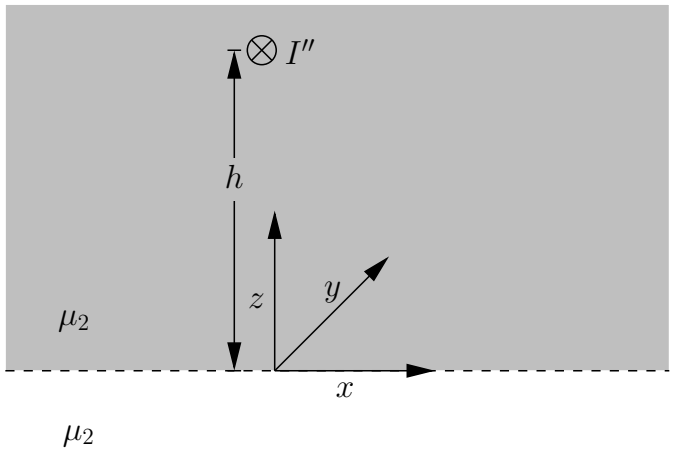

Figure G.3: Solution for the $z \leq 0$ region. The gray region indicates where the solution is not valid.

image source I'' at the same location, though it is not necessarily equal to the original source, and considering the entire space to have permeability μ_2. This is shown in Fig. G.3, and, again, this solution is valid only for $z \leq 0$, which we'll call region two.

That the solution comes from placing these image sources is not obvious. Rather than having been derived explicitly, this comes from someone's astute observation that placing the images sources at these locations happens to produce the correct boundary conditions that, by the uniqueness theorem, must constitute the correct solution. We are thus forced to take the placement of these image sources as a kind of leap of faith. What these sources should be beyond their placement, however, remains to be determined.

Now since in Fig. G.2 we have removed the boundary and replaced the entire space with permeability μ_1, the solution is the superposition of the fields from each source, which can be found simply using Ampere's law. The well known solution of the magnetic field intensity around an infinite line current at the origin and flowing in the y direction is

$$H_x = \frac{I}{2\pi}\frac{z}{x^2+z^2}$$
$$H_z = -\frac{I}{2\pi}\frac{x}{x^2+z^2}$$

Applying this to our two sources in Fig. G.2, we find that the components of the magnetic field intensity vector are

$$H_{1x} = \frac{1}{2\pi}\left[\frac{I(z-h)}{x^2+(z-h)^2} + \frac{I'(z+h)}{x^2+(z+h)^2}\right] \tag{G.1}$$

$$H_{1z} = -\frac{x}{2\pi}\left[\frac{I}{x^2+(z-h)^2} + \frac{I'}{x^2+(z+h)^2}\right], \tag{G.2}$$

which is really only valid in region one. Similarly the components of the magnetic field intensity in region two, due to the sole image current, are simply

$$H_{2x} = \frac{I''}{2\pi}\frac{z-h}{x^2+(z-h)^2} \tag{G.3}$$

$$H_{2z} = -\frac{I''}{2\pi}\frac{x}{x^2+(z-h)^2}\,. \tag{G.4}$$

The normal and tangential components at the $z = 0$ boundary are simply the z and x components, respectively. Thus to enforce the first boundary condition, we set

$$\begin{aligned} B_{1z}\Big|_{z=0} &= B_{2z}\Big|_{z=0} \\ \mu_1 H_{1z}\Big|_{z=0} &= \mu_2 H_{2z}\Big|_{z=0}\,. \end{aligned} \tag{G.5}$$

Plugging in $z = 0$ into (G.2) and (G.4), and plugging the resulting expressions into (G.5), results in

$$-\frac{\mu_1 x}{2\pi}\left[\frac{I}{x^2+h^2}+\frac{I'}{x^2+h^2}\right] = -\frac{\mu_2 x}{2\pi}\frac{I''}{x^2+h^2}\,,$$

from which we clearly obtain the relation

$$\mu_1(I+I') = \mu_2 I''\,. \tag{G.6}$$

Enforcing the second boundary condition means that

$$H_{x1}\Big|_{z=0} = H_{x2}\Big|_{z=0}\,. \tag{G.7}$$

Setting $z = 0$ in (G.1) and (G.3) and plugging these into (G.7) gives

$$\begin{aligned} \frac{h}{2\pi}\left[\frac{-I}{x^2+h^2}+\frac{I'}{x^2+h^2}\right] &= \frac{-h}{2\pi}\frac{I''}{x^2+h^2} \\ I'' &= I - I'\,. \end{aligned} \tag{G.8}$$

Substituting (G.8) into (G.6) yields

$$\begin{aligned} \mu_1(I+I') &= \mu_2(I-I') \\ \boxed{I' = \frac{\mu_2-\mu_1}{\mu_2+\mu_1}I} \end{aligned} \tag{G.9}$$

and substituting this back into (G.8) results in

$$\begin{aligned} I'' &= I - \frac{\mu_2-\mu_1}{\mu_2+\mu_1}I \\ \boxed{I'' = \frac{2\mu_1}{\mu_2+\mu_1}I\,.} \end{aligned} \tag{G.10}$$

We thus have a complete solution to the problem if we substitute (G.9) and (G.10) back into the four field component equations. These results have been verified in [Knoepfel 2000]. Note that if $\mu_2 \to \infty$, which is a perfect magnetic conductor, then $I' = I$ and $I'' = 0$, meaning there is no field inside the perfectly conducting region. This is analogous to a perfect electric conductor in which no electric fields are present. Likewise for $\mu_1 = \mu_2$ we have $I' = 0$ and $I'' = I$ just as we'd expect.

The method of images holds not only for electrostatic/magnetostatic fields but also for time harmonic fields, though about the more general, completely dynamic case the author is not as certain. Similarly, as should be clear from the superposition principle, its use can be extended beyond single sources to any configuration of sources, provided that they each have their images. The situation is analogous to geometric optics in which the most general case of regions having two different permeabilities is analogous to an interface at which some light is reflected and some transmitted, which may perhaps be from whence the insight of image placement came. The perfect electric or magnetic conductor case is analogous to a perfect mirror at which all of the light is reflected. The electric or magnetic fields are analogously "reflected" and/or "transmitted" at a dielectric and/or magnetic interface and the field lines are refracted. Actually this is more than mere analogy considering that light is of course nothing more than electromagnetic fields oscillating in space and time.

H
Derivatives of Hyperbolic/Trigonometric Functions

In Section 4.2 we require the derivatives of the hyperbolic/trigonometric functions $F_1(x)$ and $F_2(x)$, which shall be determined here. Beginning with $F_1(x)$ we have

$$\begin{aligned}\frac{dF_1}{dx} &= \frac{d}{dx}\frac{\sinh 2x + \sin 2x}{\cosh 2x - \cos 2x} \\ &= \frac{(2\cosh 2x + 2\cos 2x)(\cosh 2x - \cos 2x) - (\sinh 2x + \sin 2x)(2\sinh 2x + 2\sin 2x)}{(\cosh 2x - \cos 2x)^2} \\ &= 2\frac{\cosh^2 2x - \cos^2 2x - \sinh^2 2x - 2\sinh 2x \sin 2x - \sin^2 2x}{(\cosh 2x - \cos 2x)^2}\,.\end{aligned}$$

Recalling that

$$\cosh^2 x - \sinh^2 x = 1 \tag{H.1}$$

and

$$\cos^2 x + \sin^2 x = 1, \tag{H.2}$$

the above result reduces to

$$\frac{dF_1}{dx} = -4\frac{\sinh 2x \sin 2x}{(\cosh 2x - \cos 2x)^2}\,. \tag{H.3}$$

We now use the hyperbolic identity

$$\sinh 2x = 2\cosh x \sinh x \tag{H.4}$$

and the trigonometric identity

$$\sin 2x = 2\cos x \sin x \tag{H.5}$$

to reduce the above to its most useful form:

$$\boxed{\frac{dF_1}{dx} = -16\frac{\cosh x \sinh x \cos x \sin x}{(\cosh 2x - \cos 2x)^2}\,.} \tag{H.6}$$

Now, to determine the derivative of $F_2(x)$, we have

$$\begin{aligned}
\frac{dF_2}{dx} &= \frac{d}{dx}\frac{\cosh x \sin x + \sinh x \cos x}{\cosh 2x - \cos 2x} \\
&= \frac{1}{(\cosh 2x - \cos 2x)^2}\left[(\sinh x \sin x + \cosh x \cos x + \cosh x \cos x - \sinh x \sin x)\right. \\
&\quad \left.\times(\cosh 2x - \cos 2x) - (\cosh x \sin x + \sinh x \cos x)(2\sinh 2x + 2\sin 2x)\right] \\
&= \frac{2}{(\cosh 2x - \cos 2x)^2}\left[\cosh x \cosh 2x \cos x - \cosh x \cos x \cos 2x\right. \\
&\quad - \cosh x \sinh 2x \sin x - \cosh x \sin x \sin 2x - \sinh x \sinh 2x \cos x \\
&\quad \left. - \sinh x \cos x \sin 2x\right]\,.
\end{aligned}$$

It is here that we again use (H.4) and (H.5) in addition to the hyperbolic/trigonometric identities

$$\cosh 2x = \cosh^2 x + \sinh^2 x$$

and

$$\cos 2x = \cos^2 x - \sin^2 x\,.$$

After applying these, the above becomes

$$\begin{aligned}
\frac{dF_2}{dx} &= \frac{2}{(\cosh 2x - \cos 2x)^2}\left[\cosh x \cos x(\cosh^2 x + \sinh^2 x)\right. \\
&\quad - \cosh x \cos x(\cos^2 x - \sin^2 x) - \cosh x \sin x(2\cosh x \sinh x) \\
&\quad - \cosh x \sin x(2\cos x \sin x) - \sinh x \cos x(2\cosh x \sinh x) \\
&\quad \left. - \sinh x \cos x(2\cos x \sin x)\right] \\
&= \frac{2}{(\cosh 2x - \cos 2x)^2}\left[\cosh^3 x \cos x + \cosh x \sinh^2 x \cos x - \cosh x \cos^3 x\right. \\
&\quad + \cosh x \cos x \sin^2 x - 2\cosh^2 x \sinh x \sin x - 2\cosh x \cos x \sin^2 x \\
&\quad \left. -2\cosh x \sinh^2 x \cos x - 2\sinh x \cos^2 x \sin x\right] \\
&= \frac{2}{(\cosh 2x - \cos 2x)^2}\left[\cosh^3 x \cos x - \cosh x \cos^3 x - \cosh x \sinh^2 x \cos x\right. \\
&\quad \left. - \cosh x \cos x \sin^2 x - 2\cosh^2 x \sinh x \sin x - 2\sinh x \cos^2 x \sin x\right] \\
&= \frac{2}{(\cosh 2x - \cos 2x)^2}\left[\cosh x \cos x(\cosh^2 x - \sinh^2 x - \cos^2 x - \sin^2 x)\right. \\
&\quad \left. -2\sinh x \sin x(\cosh^2 x + \cos^2 x)\right]\,.
\end{aligned}$$

Since, by (H.1) and (H.2),

$$\cosh^2 x - \sinh^2 x - \cos^2 x - \sin^2 x = 0\,,$$

we are left with

$$\boxed{\frac{dF_2}{dx} = -4\frac{\sinh x \sin x(\cosh^2 x + \cos^2 x)}{(\cosh 2x - \cos 2x)^2}\,.} \tag{H.7}$$

Thus concludes the determination of the required derivatives.

I

Limits of Hyperbolic/Trigonometric Functions

In Section 4.2 we require the limits of the the hyperbolic/trigonometric functions $F_1(x)$ and $F_2(x)$, which shall be determined here. Beginning with $F_1(x)$ we have

$$\lim_{x\to\infty} F_1(x) = \lim_{x\to\infty} \frac{\sinh 2x + \sin 2x}{\cosh 2x - \cos 2x}\,.$$

We can note immediately that this limit in this form becomes the indeterminate ∞/∞, thereby making it a candidate for l'Hôpital's rule. Applying this however results in another indeterminate limit and repeated application will cycle between sinh / sin and cosh / cos functions, all of which are indeterminate. We shall therefore take a different by approach using the definition of the hyperbolic functions and multiplying the top and bottom by two:

$$\begin{aligned}\lim_{x\to\infty} F_1(x) &= \lim_{x\to\infty} \frac{e^{2x} - e^{-2x} + 2\sin 2x}{e^{2x} + e^{-2x} - 2\cos 2x} \\ &= \lim_{x\to\infty} \frac{1 - e^{-4x} + 2e^{-2x}\sin 2x}{1 + e^{-4x} - 2e^{-2x}\cos 2x} \\ &\boxed{\lim_{x\to\infty} F_1(x) = 1\,.}\end{aligned}$$

This last step warrants some explanation. The second terms in the numerator and denominator clearly go to zero while each trigonometric term is indeterminate in the limit but finite and therefore, because they are multiplied by terms that go to zero, go to zero, leaving unity.

For $F_2(x)$,

$$\lim_{x\to\infty} F_2(x) = \lim_{x\to\infty} \frac{\cosh x \sin x + \sinh x \cos x}{\cosh 2x - \cos 2x}\,,$$

we have a similar situation regarding the use of l'Hôpital's rule as so must again utilize the definition of the hyperbolic functions and multiply the top and bottom by two:

$$\begin{aligned}\lim_{x\to\infty} F_2(x) &= \lim_{x\to\infty} \frac{(e^x + e^{-x})\sin x + (e^x - e^{-x})\cos x}{e^{2x} + e^{-2x} - 2\cos 2x} \\ &= \lim_{x\to\infty} \frac{(1 + e^{-2x})\sin x + (1 - e^{-2x})\cos x}{e^x + e^{-3x} - 2e^{-x}\cos 2x} \\ &\boxed{\lim_{x\to\infty} F_2(x) = 0\,.}\end{aligned}$$

In the last step, the numerator as a whole is indeterminate but finite in the limit and the denominator goes to infinity, thus the entire limit is zero.

References

Albach, M., Stadler, A., and Spang, M. 2007. The influence of ferrite characteristics on the inductance of coils with rod cores. *43,* 6 (June), 2618–2620.

Bartoli, M., Noferi, N., Reatti, A., and Kazimierczuk, M. K. 1995. Modelling winding losses in high-frequency power inductors. *Journal of Circuits, Systems, and Computers 5,* 4, 607–626.

Bennet, E. and Larson, S. C. 1940. Effective resistance to alternating currents of multilayer windings. *Trans. Amer. Inst. Elect. Eng. 59*, 1010–1017.

Bladel, J. V. 1985. *Electromagnetic Fields.* Hemisphere.

Dowell, P. L. 1966. Effects of eddy currents in transformer windings. *IEE Proc. 113,* 8 (Aug.), 1387–1394.

Ferreira, J. A. 1994. Improved analytical modeling of conductive losses in magnetic components. *9,* 1 (Jan.), 127–131.

Hurley, W. G., Gath, E., and Breslin, J. G. 2000. Optimizing the ac resistance of multilayer transformer windings with arbitrary current waveforms. *15,* 2 (Mar.), 369–376.

Jackson, J. D. 1962. *Classical Electrodynamics.* John Wiley & Sons.

Knoepfel, H. E. 2000. *Magnetic Fields: A Comprehensive Theoretical Treatise for Practical Use.* John Wiley & Sons.

Kutkut, N. H. 1998a. Optimal air-gap design in high-frequency foil windings. *13,* 5 (Sept.), 942–949.

Kutkut, N. H. 1998b. A simple technique to evaluate winding losses including two-dimensional edge effects. *13,* 5 (Sept.), 950–958.

Perry, M. P. 1979. Multiple layer series connected winding design for minimum losses. *PAS-98,* 1 (Jan./Feb.), 116–123.

Podoltsev, A., Kucheryavaya, I. N., and Lebedev, B. B. 2003. Analysis of effective resistance and eddy-current losses in multiturn winding of high-frequency magnetic components. *39,* 1 (Jan.), 539–548.

Reatti, A. and Kazimierczuk, M. K. 2002. Comparison of various methods for calculating the ac resistance of inductors. *38,* 3 (May), 1512–1518.

Robert, F. 2002. A theoretical discussion about the layer copper factor used in winding losses calculation. *38,* 5 (Sept.), 3177–3179.

Robert, F. and Mathys, P. 1998. Ohmic losses calculation in SMPS transformers: Numerical study of Dowell's approach accuracy. *34,* 4 (July), 1255–1257.

Roshen, W. A. 2007. Fringing field formulas and winding loss due to an air gap. *43,* 8 (Aug.), 3387–3394.

Spang, M. and Albach, M. 2008. Optimized winding layout for minimized proximity losses in coils with rod cores. *44,* 7 (July), 1815–1821.

Vandelac, J. and Ziogas, P. D. 1988. A novel approach for minimizing high-frequency transformer copper losses. *3,* 3 (July), 266–277.

Venkatraman, P. S. 1984. Winding eddy current losses in switch mode power transformers due to rectangular wave currents. *Proceesings of Powercon 11*, 1–11.